Two-Body Photodisintegration of the Deuteron at Intermediate Energy

Thesis by

J. Eric Belz

In Partial Fulfillment of the Requirements

For the Degree of

Doctor of Philosophy

California Institute of Technology

Pasadena, California

1994

(Submitted January 5, 1994)

ACKNOWLEDGEMENTS

This work would not have been possible without the help of a great many people. I would like to thank my advisor, Bob Mckeown, for providing me with the opportunity to pursue this research. The experiment would not have been possible if not for the expertise of the scientist and staff at the SLAC laboratory, and the members of the NE 17 collaboration. Special thanks go to Rolf Ent, Brad Filippone, Naomi Makins and Tom O'Neill, who played major roles in the particularly painstaking process of understanding the spectrometer and the writing and debugging of vast amounts of software, without which this experiment would not have been possible. I would also like to thank Roy Holt, whose advise and knowledge were invaluable in the completion of this thesis.

Finally, I would like to thank my friends and family for supporting me over the years. I am particularly grateful to my Mom, who always encouraged and supported me through the highs and lows of my graduate work.

Abstract

We have measured the differential cross section for two-body deuteron photodisintegration at center-of-mass angles of 90°, 53° and 37° with photon energies from 1.6 GeV to 2.8 GeV. Additional data were taken at $\theta^* = 37°$ and E_γ =4.2 GeV. Invariant cross sections at $\theta^* = 90°$ and 53° appear to follow a simple scaling law predicted by constituent counting rules of perturbative QCD, while the cross section at $\theta^* = 37°$ shows a slower fall-off with photon energy. Angular distributions show increasing forward peaking at higher energies. Agreement with various theoretical predictions based on pQCD and meson-exchange models is discussed.

Contents

Introduction 1

I Exclusive Photodisintegration 3

A Physics Motivation 3

B QCD and Nuclear Physics 3

1 Quantum Chromodynamics 3

2 Medium Energy Nuclear Physics 5

C Theoretical Considerations 6

1 Dimensional-Scaling 7

2 Reduced Nuclear Amplitudes 13

3 Conventional Meson-Exchange Models 16

4 Asymptotic Amplitudes 19

D Summary 21

II Experiment 23

A Electron Beam 25

B Radiator 27

C Targets 27

D Spectrometer 29

1 Spectrometer Optics 30

2 Detector Package 30

E Trigger and Electronics 36

F Data Aquisition 36

G Run Plan 38

III Pass-1 Analysis 40

A Event Analysis 40

1 Tracking 40
2 Efficiencies 43
3 Dead-time 44
B Particle ID 49
1 The Time-of-Flight Detector 49
2 Measuring Particle Velocity 49

IV Spectrometer Calibration **54**

A 8 GeV/c Coordinates 55
1 Energy Loss 56
B The 8 GeV/c Model 57
C Measurement of the p(e,e′)p Cross Section 62
1 The Born Approximation 62
2 Yield from p(e,e′)p 64
3 Radiative Corrections 65
4 Solid Angle Calculation 67
5 Measured Cross Section 68
6 Momentum Scan 68
7 Extended Target Acceptance 69
D Accuracy of the Reconstruction Matrix Elements 70
1 De-radiation of W^2 72
2 Kinematic Calibration Results 76
3 Spectrometer Resolution 79
E 8 GeV/c Solid Angle 80
F Nuclear Interactions of Protons 82
1 Calculation of Nuclear Absorption 82
2 Measurement of Nuclear Absorption 83

G Summary 84

V Measurement of the Photodisintegration Cross Section 86

A The ^{2}H(γ,p)n Cross Section 86

B End-Point Fitting 90

C Pion Background 92

D Two-Step Background 93

1 Pion Photoproduction 93

2 Pion Absorption 93

3 Pion-Nucleon Scattering 94

4 Two-Step Background, Summary 94

E Determination of Cross Section 95

1 The Invariant Cross Section: $d\sigma/dt$ 98

F Subtraction of Al(γ,p)X Background 98

1 Multiple Scattering in the Radiator 98

2 Testing the Subtraction 101

G Accidental Background 103

1 Z_{target} cut 103

2 Accidental Background Rates 105

3 Accidental Background Correction 105

H Measurement of the Cross Section Without the Radiator 107

I Systematic Uncertainties 111

J Summary 116

VI Results and Discussion 118

A Results 118

B Comparison with Theoretical Models and Discussion 120

1 Constituent Counting 120

2 Reduced Nuclear Amplitudes 123
3 Meson-Exchange Calculations 125
4 Asymptotic Amplitudes 126
C Summary 126

VII Conclusions **129**

APPENDIXES **131**

A Bremsstrahlung Flux **131**

List of Tables

I Dimensional-Scaling 8

II Cryogenic Targets 28

III Other Targets and Materials 29

IV The Second Order Transport Model 59

V Matrix Elements used in Data Reconstruction 61

VI Summary of p(e,e′)p Runs 63

VII Born-level Cross Sections for p(e,e′)p 64

VIII Cross Section for Elastic Scan and Extended Target Test 71

IX Summary of Radiative Correction Parameters 73

X Mean W^2 in Momentum Scan 77

XI Mean W^2 Versus Angle 77

XII Calculated Solid Angles 81

XIII Estimated Absorption of Photoprotons in Various Elements of the Target and Detector 83

XIV Measured Absorption of Photoprotons 84

XV Al(γ,d)X Rates with the Radiator In 102

XVI Accidental Background Rates 105

XVIIRaw lab cross sections measured with and without the radiator 110

XVIIISummary of systematic uncertainties 112

XIX d(γ,p)n Cross Sections 115

XX $\gamma d \rightarrow pn$ at SLAC 120

XXI Fits to $\frac{d\sigma}{dt} \sim s^{-n}$ 123

XXIIEnergy Dependence of $\gamma \rightarrow e^- e^+$ Cross Section† 132

XXIIITotal Photon Yields used in Analysis 136

List of Figures

1 Electron-Hadron Scattering 10

2 Elastic Electron Deuteron Scattering 11

3 Electromagnetic Form Factors 12

4 The Reduced Deuteron Form Factor 14

5 Lee's Meson-Exchange Model 17

6 Meson-Exchange at Low Energy 18

7 Asymptotic Amplitudes 20

8 Experimental Set-Up 24

9 The A-line 25

10 The Cryogenic Targets 28

11 The 8 GeV/c Spectrometer 30

12 Time-of-Flight Scintillator Hodoscope 33

13 The 8 GeV/c Detector Stack 34

14 Time-of-Flight Hodoscope Electronics 35

15 High Level Trigger 37

16 Wire Chamber Efficiency 45

17 Hardware Dead-time 46

18 Total Dead-Times 48

19 Pulse Height Correction 51

20 Time-of-Flight Spectrum 52

21 p(e,e′)p Focal Plane Distributions 60

22 Raw W^2 Histogram 66

23 Results of the Elastic Scan 69

24 Extended Target Acceptance 70

25 Radiative Correction Parameterization 74

26 De-radiated W^2 Histogram 76

27 $E_\gamma - E_0$ Histograms 88

28 The Radiator-out Correction 91

29 $E_\gamma - E_0$ Histogram 96

30 Background Protons from Aluminium 100

31 Al(γ,d)X) Rates 102

32 Accidental Background Time-of-Flight 104

33 ^{2}H(γ,p)n Z_{target} Distribution 104

34 Accidental Background Z_{target} Distribution 106

35 Bremsstrahlung Fluxes 108

36 Toroid Calibration 113

37 Angular Distributions 119

38 Energy Dependence of $d\sigma/d\Omega^*$ 121

39 The Invariant Cross Section 122

40 The Reduced Nuclear Amplitude 124

41 Electron Radiative Straggling 134

42 *Thick-Target* and *Thin-Target* Bremsstrahlung 135

INTRODUCTION

The reaction ^{2}H(γ,p)n has been of interest for almost 60 years, since Chadwick and Goldhaber first studied the subject [1]. This is perhaps because the deuteron is the simplest nucleus, serving as a testing ground for new experimental and theoretical developments. The large body of data at low and moderate energies has been useful in probing the so-called realistic potentials that describe the binding of the deuteron and in developing a description of the reaction in terms of meson and baryon degrees of freedom. With the development of quantum chromodynamics (QCD) as the theory of strong interactions, however, interest has shifted towards probing quark and gluon degrees of freedom at the higher energy scales now experimentally accessible.

The scattering process at low energies is well described by traditional meson-exchange models, while at very high energies we expect the process to follow the simple scaling laws of perturbative QCD. It is believed that in the low-energy non-perturbative limit of QCD, the meson and baryon description of the reaction is recovered, although a complete non-perturbative QCD calculation in this regime is not yet feasible. There have been theoretical efforts both to push the asymptotic counting rules to lower energy and also to reliably extend meson theories to the few GeV region.

The results of the SLAC experiment NE 17 are presented here. The NE 17 experiment is designed to study the energy dependence of the ^{2}H(γ,p)n cross section in the few GeV region at several center-of-mass angles. In particular, the primary goal of the experiment is to search for the onset of scaling behavior suggested by the results of the SLAC experiment NE 8, which studied the reaction up to 1.8 GeV [2].

The motivation behind the experiment, along with theoretical expectations, are discussed in the first chapter. Chapters II and III cover details of the experimental apparatus and major steps in the data reduction. The calibration of the spectrometer

and determination of the effective solid angle is discussed in Chapter IV. Chapter V presents the final steps in the determination of the reaction cross section, followed by discussion of the accuracy of the experimental procedure. The results are presented along with the existing body of experimental data in Chapter VI, followed by comparisons with appropriate theoretical models and a discussion of the significance of the measurement. Concluding remarks are given in the final chapter.

I. EXCLUSIVE PHOTODISINTEGRATION

In this section the importance of two-body photodisintegration of the deuteron in the few GeV region is discussed. Several theoretical predictions based on both QCD and hadronic models are reviewed.

A. Physics Motivation

The role of quarks in nuclei is of central importance in nuclear physics. A guiding principle in the search for clear signatures of quarks in nuclei is to perform experiments with high energy electromagnetic probes. The deuteron is the simplest nucleus—being the only bound state of two nucleons—and is therefore particularly amenable to theoretical interpretation. Furthermore, the specification of the final state of the reaction also simplifies the interpretation of experiment. The primary advantage of choosing photodisintegration over elastic electron-deuteron scattering is that a higher value of momentum transfer to the outgoing nucleons $\hat{t}_N$ can be achieved before the rapid decline in cross section with increasing momentum transfer renders the measurement too difficult.

B. QCD and Nuclear Physics

1. Quantum Chromodynamics

Quantum chromodynamics is widely accepted as the fundamental theory of strong interactions [3]. The fundamental degrees of freedom of hadrons and their interactions are the spin 1/2 quarks and the vector gluons that obey an exact internal SU(3) "color" symmetry [4]. With the advent of QCD, many heretofore seemingly unrelated hadronic phenomena were explained: quark-based spectroscopy, current algebra, the point-like structure of partons in deep inelastic scattering, jet-phenomena,

the total $e^+e^- \rightarrow hadrons$ cross section and the large-momentum transfer behavior of hadronic form factors, for instance. Given the many successes of QCD in describing the structure and interactions of meson and baryons, one expects a description of nuclear interactions to be possible as well. In the past decade there has been much theoretical effort to describe nuclear phenomena within the framework of QCD.

An extremely attractive feature of QCD is that it is an elegant generalization of quantum electrodynamics (QED), and similarly has a renormalizable perturbation theory. In addition to the quark-gluon (qg) vertex, analogous to the electron-photon ($e\gamma$) vertex in QED, the non-Abelian structure of the underlying SU(3) symmetry necessitates three-gluon (ggg) and four-gluon ($gggg$) couplings too. The resulting gluon pairs in the one-loop vacuum polarization have an anti-screening effect, and the effective strength of the quark-gluon interaction is given by

$$\alpha_s(Q^2) = \frac{4\pi}{(11 - \frac{2}{3}n_f)\log(Q^2/\Lambda^2_{\rm QCD})}. \tag{1.1}$$

Here n_f is the number of flavors of quarks with $m_f^2 \ll Q^2$. For $n_f \leq 6$ the coupling vanishes at large momentum transfer, a property known as asymptotic freedom. The parameter $\Lambda_{\rm QCD}$ sets the basic mass scale for QCD and must be determined from experiment. Current estimates have $\Lambda_{\rm QCD} \approx 100 - 300\,{\rm MeV}$ [5].

Asymptotic freedom allows perturbative calculations in the limit of large momentum transfer, and there has been much success in describing the large-Q^2 behavior of hadronic amplitudes. In fact, the comparable size of $1/\Lambda_{\rm QCD} \approx 1\,{\rm fm}$ to the nucleon radius indicates perturbative QCD may become relevant at distance scales of 1 fm or less, and that QCD dynamics must be taken into account in considering nuclear processes in which nucleon structure is relevant. Unfortunately, explicit calculations face serious difficulties. Even to lowest order, the amplitudes for the simplest nuclear reactions involve millions of Feynman diagrams. Furthermore, the largeness of α_s at low energies renders perturbative techniques useless.

2. Medium Energy Nuclear Physics

The traditional description of low energy nuclear physics in terms of the interactions of mesons and baryons has met with great sucess. This is not inconsistent with the assumption that mesons and baryons are composed of quarks, however it can not yet be proved that the usual NN and Nm interactions are recovered in the low energy limit of QCD. In attempts to incorporate QCD dynamics in the medium energy regime, various schemes such as the MIT bag model and the cloudy bag model have been proposed [6]. The qualitative similarities between quark-interchange amplitudes and meson-exchange processes have been investigated by Blankenbecler *et al.* [7] and by Sivers *et al.* [8]. Even if the meson and baryon description of nuclear physics is rigorously the low energy limit of QCD, the possibility that the usual meson-baryon-isobar degrees of freedom are insufficient to describe nuclear properties at intermediate or high energy has been pointed out [9]. Empirically, the bound states of QCD are color-singlet quark-antiquark ($q\bar{q}$) and three quark (qqq) states corresponding to the colorless mesons and baryons of nuclear physics. In nuclei however, the existence of qqq color-octet states has not been ruled out. The successful description of nuclear properties with only colorless objects indicates that these hidden color components of the wave function are negligible at low energy. At high energy however, they may be significant, thereby precluding a successful description of nuclear processes in terms of mesons and baryons. There has also been speculation of the possibilities of six-quark states and dibaryon resonances [10].

Clearly nuclear reactions in the intermediate energy region (1–5 GeV) are of particular theoretical interest; there is evidently a transition in the behavior of form factors, structure functions and amplitudes of the processes from the predictions of meson theory to the asymptotic rules of QCD. The computational difficulties facing QCD and meson theories in the intermediate energy range only enhance the need for

experimental data. The ^{2}H(γ,p)n reaction is particularly useful for two reasons. The onset of perturbative QCD is governed by the amount of momentum transferred in a process, and the photon transfers all its energy and momentum to the nucleons, thereby making the pQCD region experimentally more accessible. The reaction is also attractive from a theoretical point of view: The deuteron is the simplest nucleus, and the answer to the difficult question of whether QCD is important—and non-nucleonic degrees of freedom are required to described the reaction—or whether the photon is absorbed by the usual colorless objects familar to low energy physics will perhaps be more clear.

C. Theoretical Considerations

Several theoretical models of the γd$\rightarrow$np reaction that are applicable to the energy range of the experiment are discussed in this section. Each model represents different assumptions about the role of quark and gluon degrees of freedom in the nucleus. In Brodsky and Farrar's dimensional-scaling model [11], expected to be valid in the asymptotic regime $s \gg M_{\rm d}^2$, the deuteron comprises six deconfined non-interacting quarks. In the reduced nuclear amplitude model of Brodsky and Hiller [12] the nucleons each retain their asymptotic quark properties, and their binding in the deuteron is described in terms of color-singlet two-quark exchange. Two other models examine the reaction without the use of QCD degrees of freedom. Lee's coupled channel model [13] is a traditional meson-exchange calculation that is constrained by low-energy data and extended to higher energy, while Nagornyĭ *et al.* [14] use a covariant, gauge-invariant formulation using only baryon degrees of freedom with allowance for the internal structure of the deuteron.

1. Dimensional-Scaling

The dimensional scaling laws, first recognized by Brodsky and Farrar [15] and independently by Matveev, Muradyan and Tavhelidze [16], for the asymptotic (large s) behavior of exclusive fixed-angle scattering are described by

$$\frac{d\sigma}{dt}(AB \to CD) \sim s^{-n+2} f(t/s), \tag{1.2}$$

where $n = n_A + n_B + n_C + n_D$ is (minimum) total number of lepton, photon and elementary quark fields carrying a finite fraction of the momentum (i.e., *constituents*) in the particles A, B, C and D. The usual invariant Mandelstam variables are defined in terms of the four-momenta of the initial and final particles by

$$s = (P_A + P_B)^2 \tag{1.3}$$

$$t = (P_A - P_C)^2$$

$$u = (P_A - P_D)^2. \tag{1.4}$$

Equation 1.2 follows in the limit of large s if the interaction is described by a scale-invariant renormalizable field theory and the wave functions are finite at the origin, and hence applies to both QED and QCD. Following Brodsky and Farrar, the scattering amplitude $M_{AB\to CD}$ of the hadrons is related to the amplitude for scattering of the constituents, integrated over all possible momenta of the constituents, with the constraint that they sum to the hadron momentum. With $n = n_A + n_B + n_C + n_D$ external lines, the scattering amplitude has dimensions $[length]^{n-4}$, and at large s and t with t/s fixed, the only length scale is $(\sqrt{s})^{-1}$. Integrating over the constituent's momenta cannot introduce an s dependence, so that $M_{AB\to CD} \sim s^{-\frac{n}{2}+2}$; Equation 1.2 then follows since [17]

$$\frac{d\sigma}{dt} = \frac{|M|^2}{64\pi s \mathbf{p_A^2}} \tag{1.5}$$

TABLE I. Dimensional-Scaling

Reaction	Energy	θ^*	Predicted	Measured
$pp \to pp$	$s > 15\,\mathrm{GeV}^2$	$38^\circ < \theta^* < 90^\circ$	10	9.7±0.5
$\gamma p \to \pi^+ n$	$E_\gamma = 4 - 7.5\,\mathrm{GeV}$	$\theta^* = 90^\circ$	7	7.3±0.4
$\gamma p \to \pi^0 p$	$E_\gamma = 4 - 7.5\,\mathrm{GeV}$	$\theta^* = 90^\circ$	7	7.6±0.7

and $p_A^2 \to s$ as $s \to \infty$, where $\mathbf{p_A}$ is the three momentum of the incident particle.

Although more careful reasoning is needed to establish Equation 1.2—to rule out the possibility that hadron masses or binding energies set the scale rather than s, for instance—the argument presented is essentially correct. Furthermore, dimensional arguments cannot specify possible powers of logarithms present in M, and indeed logarithmic scaling violations are expected from QCD [3].

The constituent-counting rules have been quite successful in describing the energy dependence of many scattering processes. Comparisons with hadronic processes such as pp→pp [18] and pion photoproduction $\gamma p \to \pi^+ n$ [19] and $\gamma p \to \pi^0 p$ [20] are summarized in Table I.

Given the sucess of the dimensional scaling laws outlined in Table I, it is reasonable to apply them the ^{2}H(γ,p)n reaction. In the quark model, of course, $n_p = n_n = 3$ and $n_d = 6$; then with $n_\gamma = 1$ and $\mathbf{p_A^*} = (s - M_\mathrm{d}^2)/(2\sqrt{s})$, Equation 1.2 becomes

$$\frac{d\sigma}{dt}(\gamma d \to np) \sim \frac{1}{(s - M_\mathrm{d}^2)^2}|M|^2 \tag{1.6}$$

$$\sim \frac{1}{(s - M_\mathrm{d}^2)^2} \cdot s^{-9} \cdot f(\theta^*)$$

$$\sim s^{-11} \cdot f(\theta^*), \text{ when s} \gg \mathrm{M_d^2}. \tag{1.7}$$

The Q^2 behavior of the electromagnetic form factors of hadrons is also explained by the dimensional scaling laws. In $eH \to eH$ scattering (Figure 1) the ingoing and outgoing electrons are counted as one elementary field each, and the initial and final

hadron each contain n_H elementary fields, where n_H is the number of quarks in the hadron. Thus the dimensional scaling law predicts

$$\frac{d\sigma}{dt}(eH \to eH) \sim s^{-(2+2n_H)+2} f(t/s) \tag{1.8}$$

$$\sim s^{-2n_H} f(t/s).$$

(1.9)

The usual definition of the spin averaged electromagnetic form factor is such that

$$\frac{d\sigma}{d\Omega}(eH \to eH) \sim \frac{1}{|t|}|F(t)|^2. \tag{1.10}$$

With t/s fixed, Equation 1.9 and Equation 1.10 can be combined to yield

$$|F(t)| \sim |t|^{1-n_H}. \tag{1.11}$$

The results can be understood in terms of quark-rescattering as follows. In Figure 2 the electron undergoes a hard-scattering from a quark in the hadron, with four-momentum transfer q^μ. The condition of elastic scattering requires that the final state be the same hadron with additional four-momentum q^μ, but in order for this to happen the four-momentum must be transferred to each of the remaining $n_H - 1$ quarks via hard gluon exchange. Each of the gluon propagators in the amplitude carries a factor $1/q^2 = 1/t$, and Equation 1.11 follows immediately.

Although there has been some controversy in the interpretation [21], the observed monopole behavior of the pion form factor ($F_\pi \sim |t|^{-1}$) and dipole behavior of the nucleon form factor ($F_N \sim |t|^{-2}$) are explained by the counting rules, as shown in Figure 3. The deuteron is a six quark system, so the scaling laws predict $F_d(t) \sim |t|^{-5}$, however it is clear that the scaling regime has not yet been reached even though the data extend up to $t \approx 4\,\mathrm{GeV}^2$. This is not surprising though, if we consider the average momentum transfer to the nucleons in the deuteron:

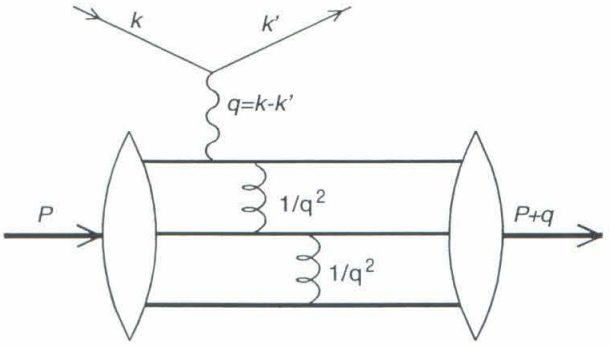

FIG. 1. Electron-Hadron Scattering

The figure shows the quark re-scattering diagram description of elastic electron-hadron scattering. The electron exchanges a virtual photon carrying four-momentum q^μ with a quark in the hadron. The four-momentum is distributed to the remaining $n_H - 1$ quarks via the exchange of $n_H - 1$ hard gluons. Each of the gluon propagators carries a factor $\alpha_s(Q^2)/Q^2$ in the amplitude.

$$\hat{t}_{\rm N}^{\rm ed} = (P'_{\rm d}/2 - P_{\rm d}/2)^2 \tag{1.12}$$

$$= (q/2)^2,$$

$$\approx -M_{\rm d}T_{\rm d}/2, \tag{1.13}$$

where $T_{\rm d}$ is the kinetic energy of the recoiling deuteron. At the highest momentum transfers attainable in elastic *ed* scattering, the momentum transferred to each nucleon is only $\hat{t}_N^{ed} \approx 1\,{\rm GeV}^2$, and the nucleon form factors do not clearly scale until $\hat{t}_N^{eN} = q^2 \gtrsim 2\,{\rm GeV}^2$.

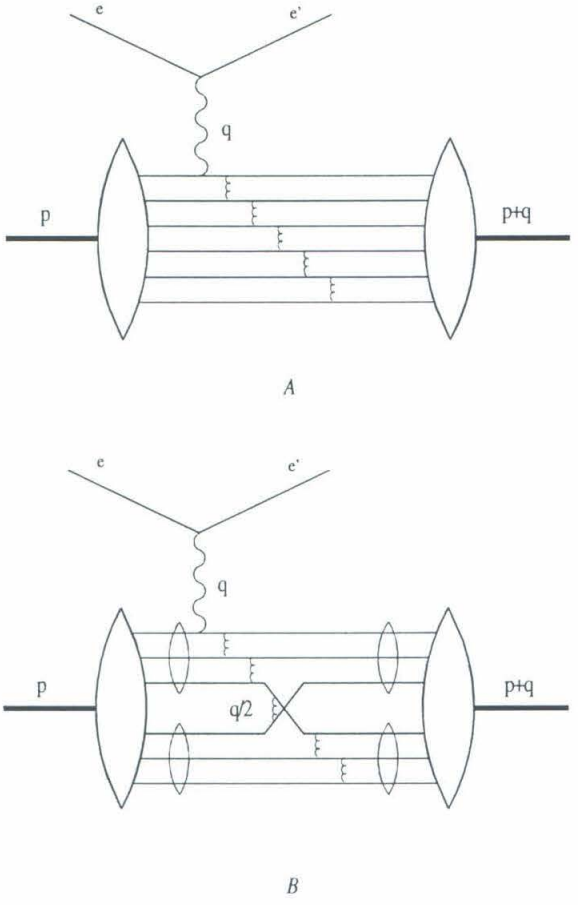

FIG. 2. Elastic Electron Deuteron Scattering

The figure, after [20], *shows two views of elastic electron deuteron scattering: (A) the re-scattering picture of pQCD scaling similar to Figure 1 with* $n_H = 6$, *and (B) the quark interchange diagram of the reduced nuclear form factor. In (B) the nucleons retain their identity as three-quark color singlet objects and interact by the interchange of color-singlet quark pairs.*

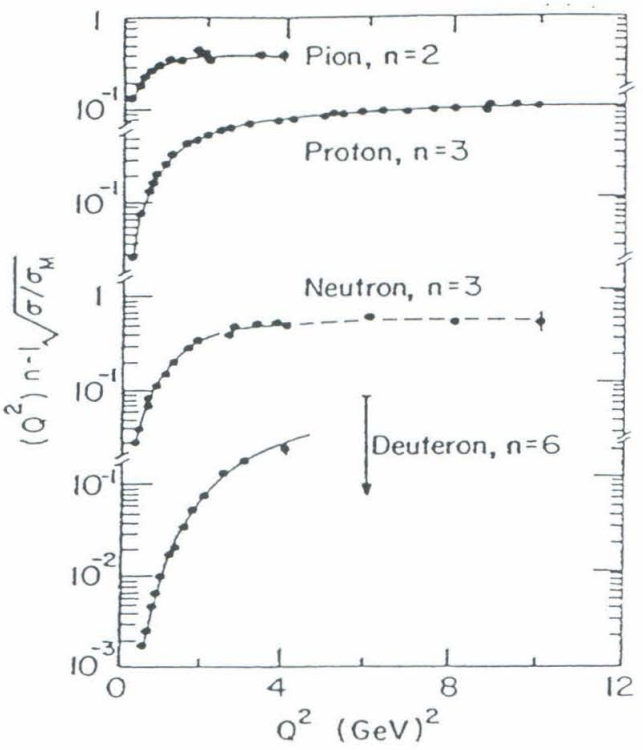

FIG. 3. Electromagnetic Form Factors

The figure, taken from [3], *shows the measured electromagnetic form factors of elastic electron-hadron scattering in terms of the constituent counting rules. Note that the pion and nucleon form factors exhibit scaling behavior, but the scaling region of the deuteron form factor has not yet been reached experimentally.*

2. Reduced Nuclear Amplitudes

The failure of dimensional scaling to describe elastic electron-deuteron scattering led Brodsky and Chertok [20] to the reduced nuclear amplitude approach, effectively producing scaling at lower momentum transfers.

Interpreting the deuteron form factor $F_d(Q^2 = -q^2)$ as the probability that the deuteron remains intact after absorbing four-momentum q^μ, they argue that, to the extent binding energy can be neglected, one can factor out the probability that the two nucleons remain intact after each absorbing, on average, four-momentum $q^\mu/2$. The reduced deuteron form factor is thus defined:

$$f_d(Q^2) = \frac{F_d(Q^2)}{F_n(Q^2/4)F_p(Q^2/4)}. \tag{1.14}$$

The nucleon internal degrees of freedom are accounted for by dividing out the nucleon form factors given by the dipole form [17]:

$$F_n(Q^2) \sim F_p(Q^2) \sim \frac{1}{1 + \frac{Q^2}{0.71\,(\mathrm{GeV/c})^2}} \tag{1.15}$$

$$\equiv F_N(Q^2). \tag{1.16}$$

The nuclear structure of the deuteron is now represented in $f_d(Q^2)$ in a manner consistent with QCD.

In contrast to $F_d(Q^2)$, which is interpreted as the probability amplitude of the six-quark system remaining intact, $f_d(Q^2)$ suggests that the probability amplitude contains two parts: the amplitude that the nucleons remain bound and the amplitude that they reform in the ground state deuteron. Treating the deuteron as comprising two constituents, the "reduced" proton and neutron, the QCD scaling laws predict the reduced form factor behavior:

$$f_d(Q^2) \sim \frac{1}{1 + \frac{Q^2}{m_0^2}} \to \frac{\mathrm{const}}{Q^2}, \tag{1.17}$$

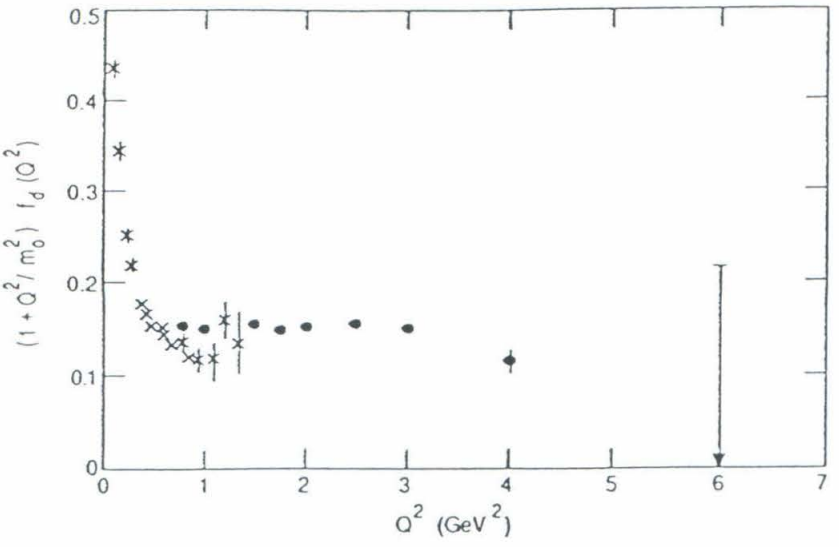

FIG. 4. The Reduced Deuteron Form Factor

The figure, taken from [20], *shows that with the reduced deuteron form factor, scaling in elastic electron-deuteron scattering can be achieved at low momentum transfers* ($Q^2 \approx 1\,(\mathrm{GeV/c})^2$). *The value* $m_0^2 = 0.28\,(\mathrm{GeV/c^2})^2$ *is from a parameterization of the pion form factor.*

where $m_0^2 = 0.28\,\mathrm{GeV}^2$ comes from a fit to the pion form factor, and is irrelevant at the energies considered here. The results show that the QCD scaling predictions can be extended down to $-t \sim 1\,(\mathrm{GeV/c})^2$, as shown in Figure 4.

In the reduced form factor interpretation, the nucleons retain their identity— in contrast to the six-quark bag picture of asymptotic scaling which in principle requires states with hidden color— and their binding is understood in terms of color-singlet quark interchange. The justification for the reduced form factor is that the mass scale for the quark-quark interaction inside the nucleon is not the same as that between the two interchanging quarks, and at momentum transfers of a few GeV^2, these mass scales are distinguishable. As t becomes very large, though, the QCD scaling laws are recovered.

The sucess of the reduced form factor approach to elastic *ed* scattering led Brod-

sky and Hiller to generalize it to other nuclear reactions [12]. Again the quark-quark interaction within the nucleon is assumed to have a different mass scale than the quark-quark interaction binding the nucleus together. Consider a process with amplitude $M(s,t)$ that involves A ingoing nucleons and A outgoing nucleons, and in the zero binding energy limit transfers four-momentum q_i to each nucleon $i = 1, \ldots, A$. The reduced amplitude is defined as

$$m(s,t) = M(s,t) \left[\prod_{i=1}^{A} F_{\mathrm{N}}(\hat{t}_i = |q_i^2|) \right]^{-1} . \tag{1.18}$$

Thus, the reduced amplitude for exclusive photodisintegration of the deuteron is

$$m_{\gamma \mathrm{d} \to \mathrm{np}} = \frac{M_{\gamma \mathrm{d} \to \mathrm{np}}}{F_{\mathrm{n}}(\hat{t}_{\mathrm{n}}) F_{\mathrm{p}}(\hat{t}_{\mathrm{p}})}. \tag{1.19}$$

Here the momentum transfer to the nucleons is defined analogously to Equation 1.13:

$$\hat{t}_{\mathrm{N}}^{\gamma \mathrm{d}} = (P_{\mathrm{N}} - \frac{1}{2} P_{\mathrm{d}})^2, \tag{1.20}$$

where P_{d} is the initial four-momentum of the deuteron and P_{N} is the four-momentum of the recoiling neutron or proton. Equation 1.20 reduces to

$$\hat{t}_{\mathrm{N}}^{\gamma \mathrm{d}} = m_{\mathrm{N}}^2 + (M_{\mathrm{d}}/2)^2 - M_{\mathrm{d}} E_{\mathrm{N}} \approx -2 m_{\mathrm{N}} T_{\mathrm{N}} \tag{1.21}$$

where E_{N} is the total energy of the recoiling nucleon; the approximation follows from $M_{\mathrm{d}} \approx 2 m_{\mathrm{N}}$. Treating $m_{\gamma \mathrm{d} \to \mathrm{np}}$ as an elementary amplitude, the fixed angle scaling behavior of the reduced amplitude is then expected to be

$$m \sim p_T^{4-n} f(t/s), \tag{1.22}$$

where p_T is the transverse momentum given by

$$p_T^2 = \frac{1}{4}(s - M_{\mathrm{d}}^2) \sin^2 \theta^* \to tu/s, \tag{1.23}$$

and n is the minimum number of elementary photon, lepton and *reduced* nucleon fields involved in the process. Here θ^* is the center-of-mass angle of the outgoing

proton. With $n = 5$ (two ingoing nucleons, two outgoing nucleons and one photon) the reduced amplitude should fall off as p_T^{-1}. Combining Equations 1.19 and 1.22, the predicted energy dependence of the cross section in the center-of-mass is

$$\frac{d\sigma}{d\Omega^*} \propto \frac{1}{\sqrt{s(s - M_d^2)}} F_p^2(\hat{t}_p) F_n^2(\hat{t}_n) \frac{1}{P_T^2} f^2(\theta^*). \tag{1.24}$$

According to Brodsky and Hiller, Equation 1.24 should be valid above $E_\gamma \sim 1\,\mathrm{GeV}$. Although it is difficult to specify the form $f(\theta^*)$, they argue that it should at least be constant, if not forward-backward peaked, in the scaling regime. Even if $f(\theta^*)$ is constant, Equation 1.24 predicts strong symmetric forward-backward peaking of the cross section that is entirely due to the nucleon form factors.

3. Conventional Meson-Exchange Models

Meson-exchange models have traditionally been used to successfully describe nuclear physics at low-energies, without invoking the fundamental quark substructure of hadrons. An example is the Paris potential description of the NN force [22]. The calculations are, in general, model dependent and have many adjustable parameters that must be constrained by experimental data. In this section the coupled-channel meson-exchange model of Lee [13] is reviewed.

Within the frame of meson and baryon degrees of freedom, the $\gamma + d \rightarrow n + p$ process can be considered to consist of two parts: (1) the incident photon is absorbed by one of the nucleons in the deuteron, and pions or heavier mesons are produced and subsequently absorbed by the other nucleon; (2) the two outgoing nucleons interact with each other through the exchange of mesons. The approach has been fairly successful in describing the low [24,25] and intermediate [26,27] energy regions. In extending the model to higher energies, steps (1) and (2) are constrained with available data and extrapolated to higher energy, as described below.

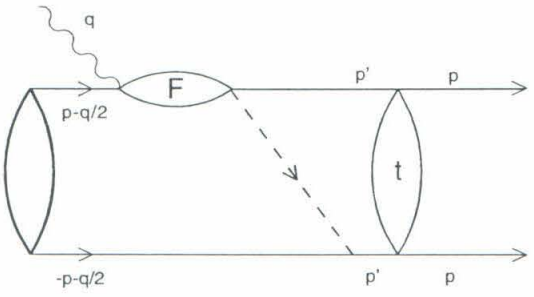

FIG. 5. Lee's Meson-Exchange Model

The figure shows the kinematics of Lee's meson-exchange model of the $^2H(\gamma,p)n$ reaction in the center-of-mass frame, where F is the off-shell amplitude of the $\gamma+N\rightarrow N+$mesons process and t is the half-off-shell matrix of the NN interaction.

Lee started with the coupled-channel meson-exchange model of NN scattering developed previously [23], in which he extended the Paris potential [22] to include the coupling to the Δ and N^* Roper resonance. The associated one-pion and two pion mechanisms were described by the standard isobar model with vertices $\Delta \leftrightarrow \pi N, N^*$ and $N^* \leftrightarrow \pi\Delta$. The model reproduced the known NN phase shifts and various NN total cross sections reasonably well up to 2 GeV. The model was used to generate the half-off-shell NN t-matrix shown in Figure 5. The photo-meson amplitude F is formulated using a Born term deduced from a field-theoretical Lagrangian and a resonant term describing Δ excitation. The Born term from [26] is extended with the isobar model [28] for $\gamma N \rightarrow \Delta \rightarrow \pi N$ to include the $\gamma N \rightarrow N^* \rightarrow \pi N$ and $\gamma N \rightarrow N^* \rightarrow \pi\pi N$ amplitudes. As a simplification, the $\pi\pi$ channel is approximated by a fictitious scalar-isoscalar particle. The resulting formulae can be found in [13].

The calculation is constrained by experimental measurements of the NN phase shifts and photo-meson production through the construction of F and t. The model is further constrained by low energy ^{2}H(γ,p)n data. As shown in Figure 6, the cal-

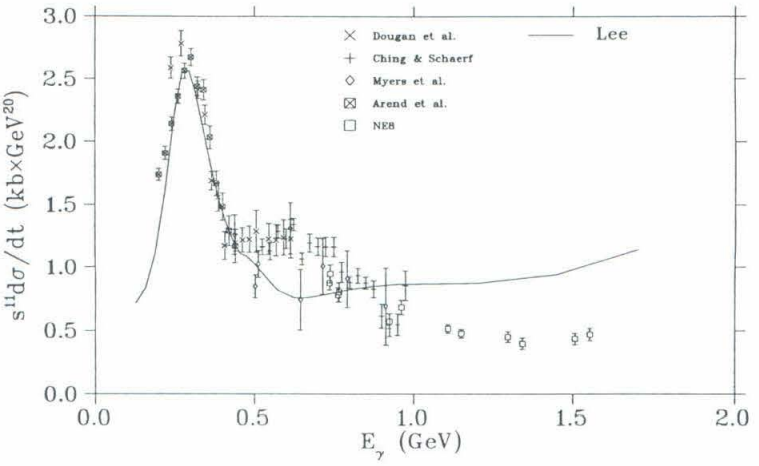

FIG. 6. Meson-Exchange at Low Energy

The figure shows a comparison of Lee's meson-exchange calculation at $\theta^* = 90^\circ$ *with the data* [59–62,2] *available before this experiment.*

culation is in good agreement with the data below $E_\gamma = 0.5\,\text{GeV}$, lower than the data between $E_\gamma = 0.5\,\text{GeV}$ and $E_\gamma = 1.0\,\text{GeV}$ and too large above $E_\gamma = 1.0\,\text{GeV}$. Lee subsequently examined the model dependence of his calculation on final state interactions (FSI) and also on choice of the deuteron wave function. In addition to the Paris potential, the Argonne V14, Reid soft-core [29] and Bonn-Q potentials were considered. Although the sensitivity to the deuteron wave function and FSI is significant, the observed energy dependence above 1 GeV cannot be obtained with the present coupled-channel formalism [23,30]. In spite of the short-comings of the present model, the meson-exchange description need not be abandoned yet. Relativistic effects need to be considered more carefully. Futhermore, the importance of higher resonances and heavier meson-exchange must be investigated quantitatively. In fact, Kang *et al.* [31] have reported good agreement with data up to $E_\gamma = 1.6\,\text{GeV}$ at center-of-mass angles of 90° by including the latter effects, however the calculation has not been extended to higher energy or other angles.

4. Asymptotic Amplitudes

Recently Nagornyĭ *et al.* have argued that the apparent failure of conventional meson theories to describe the ^{2}H(γ,p)n reaction for $E_\gamma > 1$ GeV is not surprising: At $E_\gamma > 1$ GeV deuteron configuration with characteristic sizes of $r_{eff} \sim (mq_o)^{-1/2} \simeq 0.2$ fm participate in the reaction, and wave functions derived from the realistic potentials do not accurately describe the nuclear core at such small distances [14]. Using a Lorentz-invariant, gauge-invariant field theory of bound systems developed earlier [32], they avoid the problems arising from our lack of knowledge of the wave function in the nuclear core by calculating the dNN vertex coupling in terms the asymptotic limit of a field theory using only mesons and baryon degrees of freedom. A brief outline of the theory, along with a summary of their conclusions is presented in this section.

In the asymptotic energy region, only tree diagrams are assumed to survive, and only the two lowest configurations in the Fock wave function of the deuteron are retained:

$$\Psi_{\rm d} = \cos\phi\,|{\rm NN}\rangle + \sin\phi\,|{\rm NN^*}\rangle, \tag{1.25}$$

where N* is the Roper resonance. In [32] it is shown that only the vector form factors $G_N\gamma_\nu$ and $G_{N^*}\gamma_\nu$ in the dNN and dNN^* vertices, respectively, contribute in the asymptotic limit, and the diagrams 1–5 in Figure 7 can be evaluated in terms of the masses, charges, magnetic moments and quadrupole moments of the particles involved. (The detailed formula and justification can be found in [14] and [32]). The contact diagram (6), which ensures gauge-invariance, is particularly important in hard processes because it is sensitive to the short distance behavior of the deuteron wave function. It differs from zero because of the deviation of the deuteron wave function from the Yukawa form ($G_N = const.$) at short distances. The diagram is not evaluated in terms of wave functions corresponding to realistic potentials but, rather

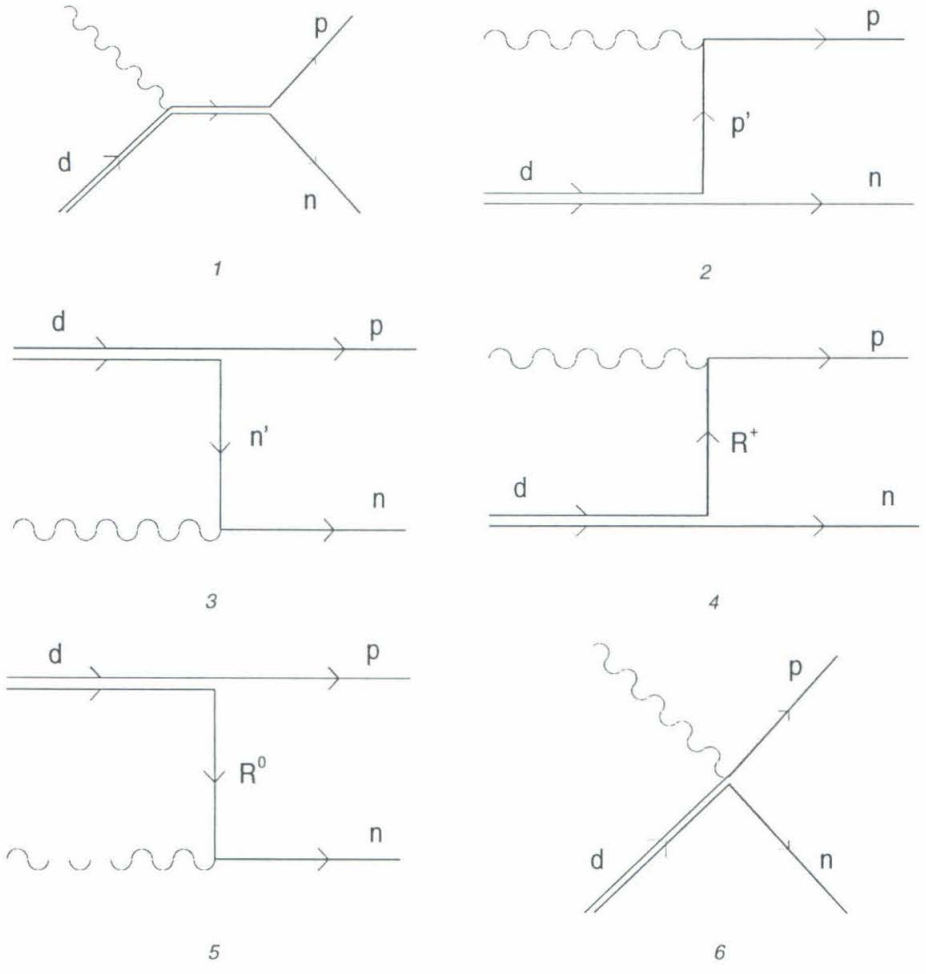

FIG. 7. Asymptotic Amplitudes

The figure, taken from [14], *shows the gauge-invariant covariant diagrams for photodisintegration of the deuteron at asymptotic energies, in the model of asymptotic amplitudes. Graphs 1, 2, 3 and 6 correspond to the NN configuration of the deuteron, while graphs 4 and 5 correspond to the NN* configuration. Graph 6 is particularly important in the asymptotic region.*

in analogy with [33], the form factor for the dNN (dNN^*) vertex with one virtual nucleon is assumed to have the three-pole form in the asymptotic limit:

$$G_{N(N^*)}(-k^2) \simeq C_{N(N'*)}[\frac{1}{2}m_\pi^2 - k^2]^{-\epsilon}, \tag{1.26}$$

$$\epsilon = 3 \ .$$

Here k^μ is the difference between the four-momenta of the outgoing proton and neutron. The parameter ϵ determines the majority of the scaling behavior of the cross section. The relative strength of the two Fock components in Equation 1.25 determines the ratio of the two constants appearing in Equation 1.26, $\alpha = C_N/C_{N^*}$. The free parameter α then has a small effect on the scaling behavior of the cross section, and the overall normalization of the C_N's must be determined from experiment.

Finally, the cross section for large but finite s can be written:

$$\frac{d\sigma}{d\Omega^*} \propto \frac{1}{s(s - M_{\rm d}^2)^{2\epsilon-1}} f(\theta^*, s); \ f(\theta^* = 90^\circ, s) \equiv 1 \ . \tag{1.27}$$

For $\theta^* = 90^\circ$ in the energy range $s = 8$–$16\,\mathrm{GeV}^2$, Equation 1.27 resembles the scaling predicted by the dimensional counting rules. The evaluation of $f(\theta^*, s)$ for $\theta \neq 90^\circ$ is strongly model dependent, however several general conclusions can be drawn: for $50^\circ < \theta^* < 130^\circ$ and $s \gg M_{\rm d}^2$, $f(\theta^*, s) \simeq f(\theta^*)$—so that the theory predicts an energy dependence similar to that expected from the constituent counting rules, while for $\theta^* < 50^\circ$ and $\theta^* > 130^\circ$, $f(\theta^*, s)$ is a rising function of s.

D. Summary

In this chapter the significance of the ^{2}H(γ,p)n in the search for the onset of scaling in exclusive nuclear reactions has been discussed. It widely believed that the relevance of the quark degrees of freedom in exclusive nuclear reactions is determined by the momentum transferred to the nucleons; thus the ^{2}H(γ,p)n reaction is particularly

attractive because the photon imparts *all* its energy and momentum to outgoing proton and neutron. The reaction has also been discussed in few GeV region without regard for the quark substructure of the deuteron, using only the usual meson and baryon degrees of freedom familiar to low energy nuclear physics.

II. EXPERIMENT

Experiment NE 17 was conducted during the summer of 1991 at the Stanford Linear Accelerator Center (SLAC) as part of the laboratory's nuclear physics program (NPAS). An electron beam ranging in energy from 1.6 GeV to 4.2 GeV impinged on a 0.77 g/cm^2 copper foil, producing bremsstrahlung photons which then irradiated a 15 cm long liquid deuterium (LD_2) target. Photoprotons from the ^{2}H(γ,p)n reaction were detected and analyzed in the 8 GeV/c spectrometer. Spectra were taken both with and without the radiator to account for virtual photons from the electron beam and bremsstrahlung production in the target materials. To ensure an exclusive reaction, only the highest energy photoprotons are accepted, thus eliminating yield from all but the two-body final state. This does not eliminate protons from the aluminium end-caps of the target, so data were taken with a nearly identical liquid hydrogen target and subtracted. The 8 GeV/c spectrometer was configured to detect and identify protons with a new time-of-flight package and Freon Čerenkov counter. Figure 8 shows a schematic diagram of the experimental arrangement.

Although the NE 17 proposal was initially deferred, the experiment became feasible with the allocation of beam-time for a combined E140x and NE 18 run [34,35]. E140x studied deep inelastic scattering from nuclear targets, and required the 15 cm ^{1}H and ^{2}H targets necessary for NE 17. The NE 18 experiment studied (e,e'p) from nuclear targets, with the coincident proton detected in the 8 GeV/c spectrometer. With the addition of the radiator-slide built for NE 8 [36], all the equipment necessary for the measurement of ^{2}H(γ,p)n in the few GeV energy range was readily available.

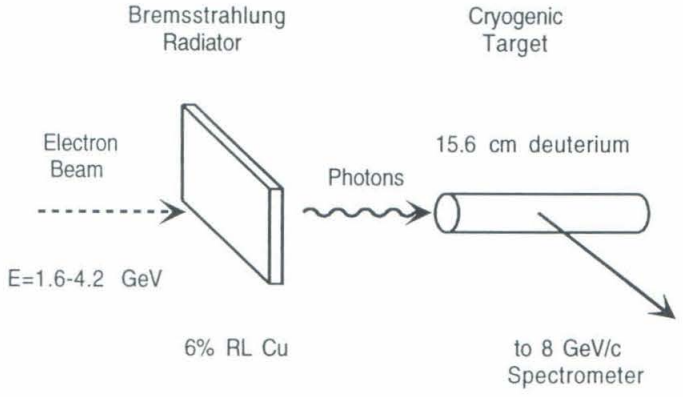

FIG. 8. Experimental Set-Up

The figure shows a schematic diagram of the experimental set-up. The electron beam impinges on a Cu radiator, producing bremsstrahlung photons that illuminate a cryogenic deuterium target. Photoprotons from $^2H(\gamma,p)n$ are detected in the 8 GeV/c spectrometer.

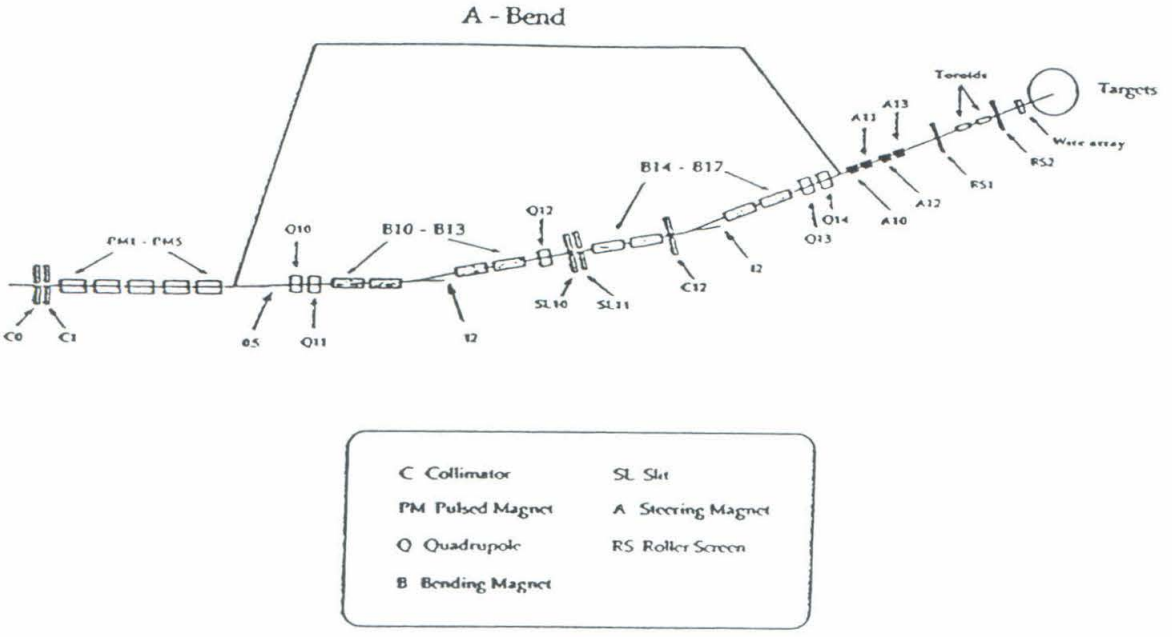

FIG. 9. The A-line

A. Electron Beam

The SLAC accelerator is an RF linac operated in a pulsed mode. The full accelerator has 30 sectors that each provide over 1 GeV of energy gain at high power. Low energy beams, however, suffer losses from low RF levels and cannot be delivered through the full accelerator at even modest currents. Experiment NE 17 used the Nuclear Physics Injector (NPI), which is located six sectors from the linac exit and provides high current (60 mA peak) pulsed beams (1.6 μs, 120 pps) up to 6 GeV. Data were generally taken at lower peak currents (15 mA) because of radiation in the detector stack.

The beam was delivered to the end-station A (ESA) via the A-beamline. (Shown in Figure 9). The A-bend comprises eight identical dipole magnets (B10-B17) that define the beam energy. A ninth dipole connected in series serves as monitor: although not part of the beam transport, a rotating wire (flip coil) mounted in the nominal beam position continuously measures the magnetic field that defines the beam energy.

The energy spread of the beam is limited by the slits SL10 and SL11, and was typically 0.2–0.4% FW. Quadrupoles Q10-Q14 are standard optical elements that shape the beam spot at the target.

The final beam steering was under experimenters control. Two Zn-S coated roller screen are remotely inserted into the beam line and viewed by a TV camera to provide a visual image of the beam spot, which can then be steered with magnets A10-A13. In addition, two crossed arrays of parallel aluminium wire (0.005 inch diameter, 0.0156 inch spacing) permanently mounted in the beam's path provide a pulse-by-pulse monitor of the beam shape. Secondary emission electrons caused by the passage of the electron beam through the wires produce currents that are then read by external circuits and monitored by a μVax computer that controls two steering magnets and keeps the beam centered on target.

Beam quality was monitored with two spill monitors, each made of a plastic scintillator optically coupled to a phototube shielded from room light. The anode signal of the phototubes were viewed on an oscilloscope and recorded by an ADC and written to tape. The bad-spill monitor was mounted in the alcove near RS1, and had an output correlated with the beam halo. The good-spill monitor was 10 m from the target at 70°, and provided a qualitative picture of the 1.6 μs beam spill on target.

The beam current was integrated on a pulse-by-pulse basis using two independent toroidal transformers. The electron beam served as the primary winding, while the secondary winding forms the toroid around the beam and is connected to a resistor and capacitor to form a resonant circuit. A beam pulse excites a damped oscillation in this circuit. The toroid is repeatedly calibrated by passing a known current through a third winding, thus there are two independent measures of the beam current. Agreement, after calibration corrections, is typically $\leq 1\%$, as shown in Figure 36.

B. Radiator

The radiator slide is the same as that used in the NE 8 experiment. Three radiators of approximately 2%, 4% and 6% of a radiation length were mounted on a slide 1.5 m upstream from the LD_2 target. Primary data were taken with only the 6% radiator. The radiator was mounted as close to the target as possible, without being in the spectrometer acceptance, to minimize the size of the bremsstrahlung beam, which was dominated by multiple scattering of the electron beam in the radiator. The radiator thickness was measured during NE 8, and is 0.864 ± 0.004 mm [36].

C. Targets

The target assembly is shown in Figure 10. There are two target ladders, one holding the solid targets, and the other the cryogenic targets and dummy used in this experiment. The liquid target ladder has both a long and a short (15 cm and 4 cm, approximately) LD_2 and LH_2 target. Only the 15 cm targets were used for production data, however, both the 15 cm and 4 cm LH_2 targets and the dummy targets were used during checkout. Computer control allowed fast and reproducible remote positioning of targets. The cryogenic liquids circulated through a loop at 2 atm (absolute pressure) and were maintained near 21 K by passing the return flow through a heat exchanger immersed in a reservoir of liquid hydrogen at atmospheric pressure. The 1 atm over-pressure raised the target liquid's boiling point by roughly 2 K over the reservoir's, thus abating boiling of the liquid in the path of the electron beam. Pressure transducers monitored the cell pressure and platinum resistors monitored the temperature. This information was used to estimate the target density in the presence of the electron beam. Properties of the cryogenic targets, measured after the experimental run, appear in Table II. The target lengths were measured at room temperature, and the length at $T \approx 21$ K is calculated to be 0.996 times the length

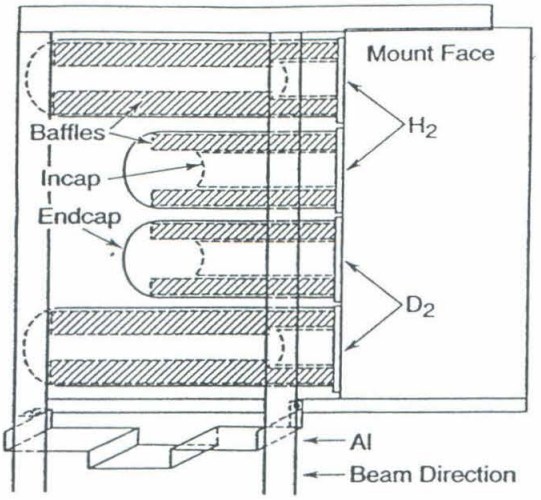

FIG. 10. The Cryogenic Targets

TABLE II. Cryogenic Targets

Target Name	Material	Length (cm @ 300 K)	Density (g/cm^2)	Purity (%)
4CM_LH2	LH_2	4.029	0.0705	99.94
15CM_LH2	LH_2	15.818	0.0705	99.94
4CM_LD2	LD_2	4.029	0.1701	99.68
15CM_LD2	LD_2	15.745	0.1701	99.68

at 300 K.

The dummy targets each comprise two pieces of aluminium alloy placed at the respective end-cap positions. The total thickness of aluminium in the beam path is 9.5 times that of the cryogenic targets. Their properties and those of other materials lying in the path of the beam or detected particle are shown in Table III.

The two target ladders are mounted on a rotating carriage that can be be positioned such that one of the target ladders is in the beam line. With the liquid-target ladder in the beam line, the solid-target ladder sat at beam-right, and ob-

TABLE III. Other Targets and Materials

Object	Material	Thickness(g/cm^2)
4 cm dummy	Al 3004 and Al 5052	0.509
15 cm dummy	Al 3004 and Al 5052	0.509
Upstream End-cap	Al 5052	0.0204
Downstream End-cap	Al 3004	0.0332
Wire Array	Al	0.0108
Hymen	Al	0.0069
Cell Wall	Al 3004	0.0345
Insulation	Mylar	0.0088
Chamber Window	Al 5052	0.0817
Air Gap	Air	0.019
8 Quad Membrane	Al 5052	0.0681

structed scattering angles greater than 53° from the 15 cm targets. Thus the data at $E_{\text{beam}} = 1.6$ GeV were taken at a center-of-mass angle of 85°, rather than 90°.

D. Spectrometer

Photoprotons produced in the target were detected in the 8 GeV/c spectrometer, shown in Figure 11. It is a vertical bend spectrometer, with magnets arranged in a QQDDQ pattern. We ran the spectrometer in the large-acceptance-mode; that is, with current in the first two quadrupole reversed with respect to the normal tune, thereby increasing the accepted solid angle from 0.75 msr to 3.2 msr at the central momentum. The detector package, shown in Figure 13, sits in a lead-lined concrete shielding hut. Three planes of scintillators serve as a fast-trigger and time-of-flight detector; ten planes of wire chambers and a hodoscope provide tracking, and an

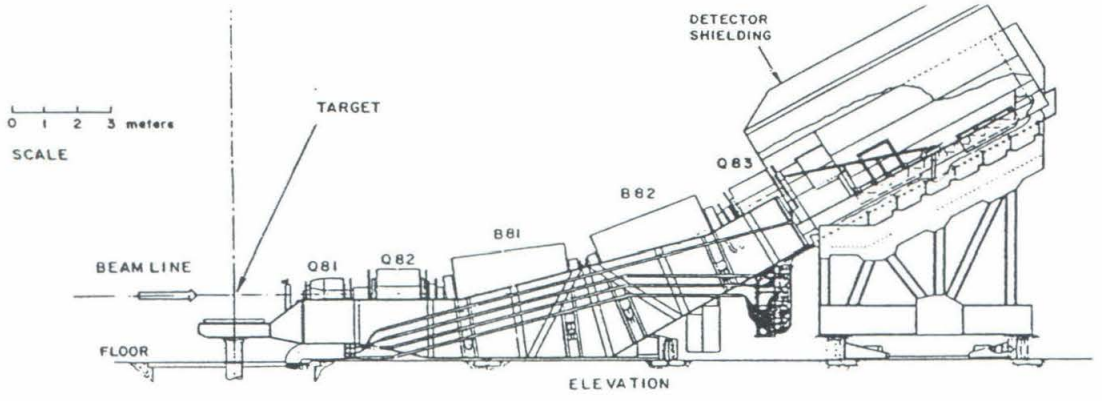

FIG. 11. The 8 GeV/c Spectrometer

atmospheric Freon Čerenkov detector provides pion rejection.

1. Spectrometer Optics

Two 15° bending magnets (B81 and B82) produce the momentum dispersion of the spectrometer, with three quadrupoles (Q81, Q82 and Q83) providing focusing. The true momentum focal plane is tilted roughly 5.8° away from the central ray. The scattering angle focal plane is normal to the central ray and separated from the center of the momentum focal plane by $\approx 0.5\,\mathrm{cm}$. A detailed description of the optics-calibration procedure is given in Chapter IV.

2. Detector Package

The first component of the detector package is the Čerenkov counter at the front end. It is a large, air-tight, light-tight iron tank mounted directly onto the magnet

absolute pressure and provided 3.1 m of radiator path. An aluminium coated 0.25 inch slumped lucite mirror focuses the Čerenkov photons onto a 5 inch Quanticon RCA 8854 phototube that had been coated with a layer of organic wavelength shifter (pTP) to enhance sensitivity in the ultraviolet [37]. Since the detector needed to separate pions from protons at momentums from 3.0–4.5 GeV/c, where the pions are still relatively slow, a high index of refraction was required. Freon-114 ($C_2Cl_2F_4$) was used; it has an index of refraction of 1.0014 at atmospheric pressure, so the corresponding threshold momentum for pions is 2.7 GeV/c.

In this experiment, pions are not the dominant non-proton background. Deuterons produced in the target end-caps by Al(γ,d)X reactions are far more copious. (Typically d/p ratios were 1/3 while π/p ratios were not more than 1/500). Indeed, even tritons produced in the end-caps were seen. Because of the modest momentum of the spectrometer, deuterons and tritons cannot be separated from protons by an atmospheric-pressure gas-Čerenkov counter, however their low velocities are ideal for time-of-flight and separation.

A time-of-flight (ToF) system comprising 3 planes of segmented scintillators was constructed for this experiment. New Bicron BC-420 fast scintillator with a 1.5 ns decay time was purchased and tested for all elements of the ToF package. The front layer provided the long arm of the ToF system, and was equipped with fast Amperex XP2020 phototubes from the decomissioned MARK-III detector at SLAC. The phototubes are rated with 1.5 ns rise time, 2.4 ns pulse duration and 0.25 ns single electron transit-time spread, and were extensively tested before the experiment. Since the front end of the spectrometer receives the most background radiation, the front scintillators were the thinnest (0.95 cm) and also had the most segments (8, vertical). The two rear planes were both 3 horizontally segmented 1.27 cm thick scintillators 3.57 m and 3.86 m from the front plane respectively. Each scintillator was viewed by phototubes at both ends. The front plane also included two large scintillators

equipped with a single phototube each. A schematic diagram of the ToF scintillators appears in Figure 12.

Ten planes of multi-wire proportional chambers spaced every 20 cm provide charged-particle track identification. They have been described in detail elsewhere [38]. In summary, each chamber has a 35 cm high by 93 cm wide active area with anode wires oriented either horizontally or at $\pm 30^{\circ}$ to the vertical (P- or T-type, respectively). In the proportional mode a gas mixture, 65.75% argon, 30.0% isobutane, 0.25% Freon 13B1 and 3.0% methylal, flows through the chambers. The chambers were labelled 1–10, starting at the front end of the detector package (Figure 13). The even chambers are P-type, with 176 wires spaced every 2 mm. The remaining chambers are T-type with alternating orientation with respect to vertical. Each has 480 wire spaced every 2 mm, however adjacent wires were connected, effectively increasing the spacing to 4 mm.

The passage of a charged particle produces ions in the gas-mixture, inducing a pulse on the nearest wire pair. A digital system built by Nanometrics Inc. is used to record up to 64 wire hits per trigger and convert the information to a bit pattern that is stored in Camac latches; all wire information within roughly 30 ns of the trigger is stored. The ten chambers provide efficient, accurate particle tracking. An algorithm uses the wire chamber information along with scintillator and hodoscope data to select tracks. The overall tracking efficiency was always greater than >99.9%, and correction was calculated and applied on a run-by-run basis.

Immediately following the wire chamber package is the NBS-hodoscope. It is essentially two crossed planes of overlapping, segmented scintillators coupled to phototubes. There are 22 vertical and 20 horizontal segments. The scintillator strips are 2 inches wide, and thus the resolution is much poorer than that of the wire chambers. The data from these detectors were used to aid track selection.

Raw analog signals from the detectors' photo tubes were carried roughly 100 m to

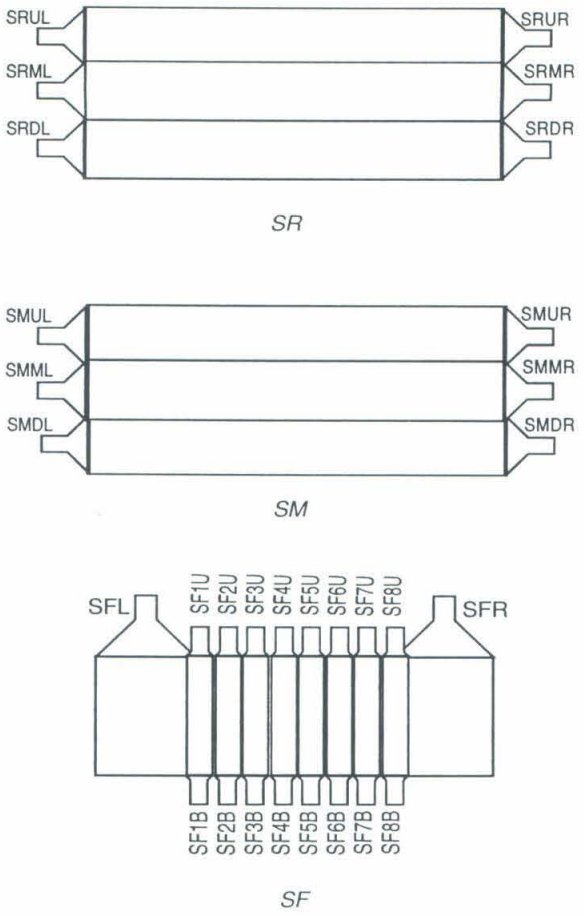

FIG. 12. Time-of-Flight Scintillator Hodoscope

The figure shows a schematic diagram of the three scintillator planes in the 8 GeV/c time-of-flight detector, approximately to scale. The horizontal-by-vertical dimensions of the SF, SM and SR planes are 89.1 cm × 45.0 cm, 101.0 cm × 41.6 cm *and* 101.0 cm × 42.4 cm, *respectively. Note that the coordinate system shown is* left *handed.*

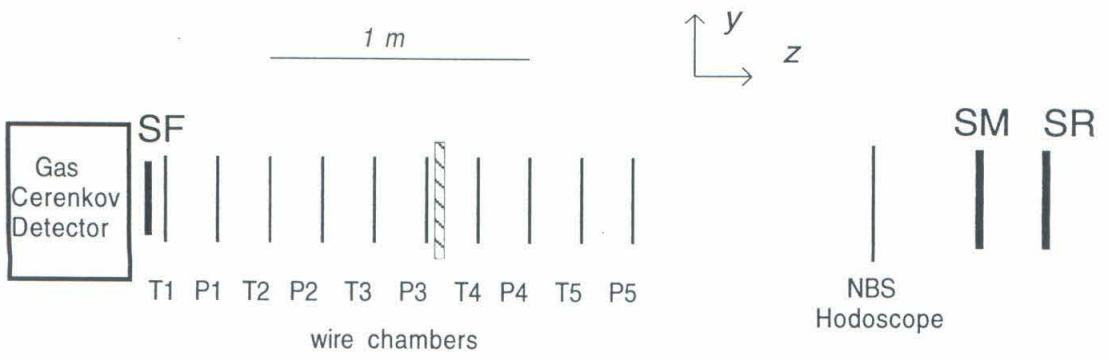

FIG. 13. The 8 GeV/c Detector Stack

The figure shows the detector stack in the 8 GeV/c spectrometer, configured to detect protons. The primary elements are the time-of-flight scintillator package (SF,SM and SR) that serves as a fast-trigger and also in particle ID, and the 10 planes of MWPC for track identification. The figure is approximately to scale.

the counting house via fast-coaxial cable, where they were fed into the fast electronics composed mainly of commercially available CAMAC and NIM modules. Figure 14 shows the primary elements of the scintillator electronics. Each detector signal passed through a fan, with one output going to an analog-to-digital converter (ADC) to record pulse height information, and the other to a discriminator. The logic-output of the discriminator was then used for trigger logic, timing information, scalers, latches, and so on. The discriminator levels and the high voltages across the phototubes had to be carefully chosen to reduce the effect of slewing [39] on the timing information without compromising good rejection of the many small spurious pulses common in an electron beam environment. The high voltages were also adjusted so that all the detectors had a similar response.

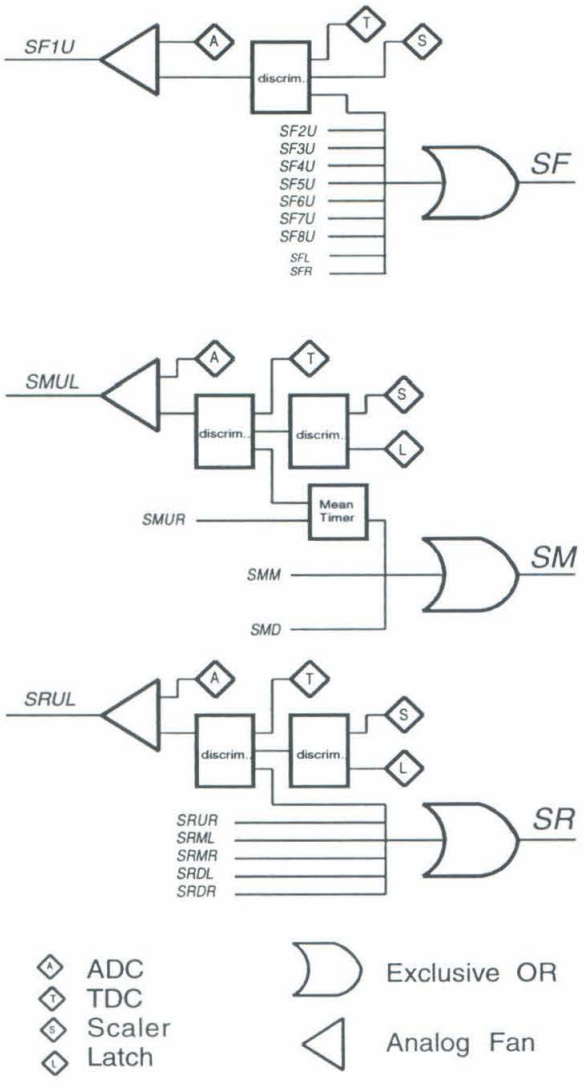

FIG. 14. Time-of-Flight Hodoscope Electronics

The figure shows the time-of-flight electronic instrumentation. For each scintillator plane, the electronics for one of the detector segments is shown. The SM and SR scintillator signals are formed by and exclusive-OR combination of the all the detectors in the respective plane, while the SF signal is an exclusive-OR of only the upper phototubes.

E. Trigger and Electronics

The trigger for the detector was a 3-fold coincidence between any element of each of the three scintillator planes, as defined by the overlap of their 20 ns logic pulses. The detectors in any given plane were timed to $\approx$10 ns. Proton transit times for the various spectrometer momentum settings run during the experiment range from 15–21 ns, so that no timing correction was needed for the different settings. Particles with $\beta \lesssim 0.4$ were too slow to fire trigger. The main electronic elements of the trigger are shown in Figure 15.

Although the trigger provides high efficiency detection of charged particles, there is no inherent particle identification, so that all charged particles (pions, deuterons, tritons, for example) passing through the detector are recorded. In addition to the 3/3 trigger, there was a prescaled 2/3-coincidence trigger and a randomly generated trigger. The 2/3 trigger is less stringent and provides the means to estimate the 3/3 trigger efficiency, while the random trigger provides a monitor of the quiescent state of the electronics (pedestal subtraction and drifts).

The fast-trigger logic generated integration gates for the ADC's, start pulses for the time-to-digital converters (TDC), gates for the wire chamber information and also reset the latches, and initiated the event logging procedure. The computer and electronics can only record one event per 1.5 μs beam burst, thus a delayed veto from the pretrigger module prevented more than 1 trigger per beam burst. The correction for the resulting dead-time, and also that from the finite duration of the logic pulses, are discussed in Section III A 3.

F. Data Aquisition

The ADC, TDC, and latch information characterizing an event were read and stored by a PDP-11. The PDP-11 could handle events at 180 Hz and the buffer could

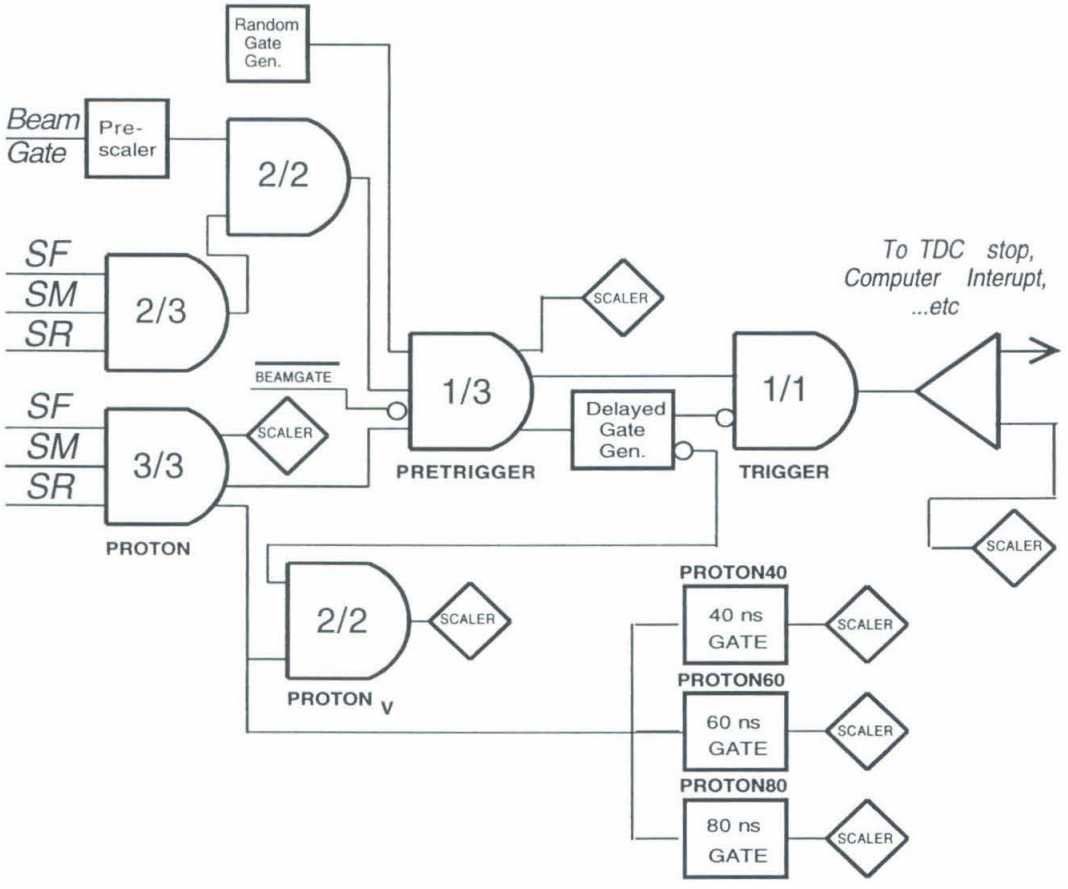

FIG. 15. High Level Trigger

The figure shows the fast-trigger for the experiment. Scalers relevant to the discussion of dead-times in Section III A 3 are also shown. The formation of the SF, SM and SR signals can be found in previous figure.

store many events blocks. Data were then recorded by a VAX 11-780 computer. The detector hardware data were recorded event-by-event on magnetic tape. Non-event information characterizing the run such as spectrometer magnet currents, target positions, high voltages, and scalers, were recorded periodically via CAMAC interfaces. A separate μVAX computer recorded beam information, which was also written to tape periodically. After the conclusion of data taking, the tape data were transferred to disk in a compressed form, using modified software from NIHKEF. Events were selected from tape based on the latch information. (For instance, only those events with an 8 GeV/c trigger were selected). ADC data were pedestal subtracted, with TDC and ADC information written to disk only for those channels with non-zero ADC values. The non-event data were stored on a run-by-run basis in an end-of-run block. The procedure allows easy access and replay of data. All the data occupied roughly 500 megabytes of disk space and required less than 2 hours of VAX-4000 CPU-time for a complete replay.

G. Run Plan

Much of the run procedure was determined on-line. Estimates of the rate for two-body photodisintegration were made beforehand by extrapolating the NE 8 data according to the s^{11} scaling law, however background rates from the target end-caps and radiation intensities in the detectors had to be determined at run time. Under most running conditions, the peak current of the accelerator had to be limited so that there were not more than 0.1 triggers per pulse (to limit dead-time to $< 10\%$). We also required that the rate in the front scintillators be less than 25/spill so that the time-of-flight system remained effective. Hence the maximum beam current and required beam-time had to be calculated during data aquisition. Because NE 17 was allotted a limited time, we were not able to complete the original scope of the experiment.

The goal of 10% statistical error was reduced to 17%, and the measurement of an angular distribution at 3.0 GeV was reduced to two 2.8 GeV measurements at $\theta^* = 90^\circ$ and 37°. (Because of the rapid decline in cross section with energy, most of the running time was spent at the highest energy). Furthermore, angular distributions were measured at 0.4 GeV intervals, instead of 0.2 GeV as originally proposed. The program to measure pion photoproduction, d(γ,d)π^0/ was dropped, except for some checkout data taken with the 1.6 GeV/c spectrometer. Nevertheless, we were able to measure a forward point at 4.2 GeV. In addition, there is important checkout data available from the NE 18 experiment that is vital to the interpretation of the NE 17 results— including p(e,e′p) data that are beyond the scope of this experiment [35].

III. PASS-1 ANALYSIS

The extraction of the photodisintegration cross section from the event-data has several phases. First the event-by-event data are read sequentially from disk; the latches and wire-chamber information are used to determine whether or not a real particle caused the trigger. If so, the scattering kinematics $(\Delta P/P_0, \Delta\theta, \phi)$ are reconstructed from the wire chamber information. The data are histogrammed on a run-by-run basis. Then, using the non-event information, such as beam charge, dead-time corrections, target-density etc., a photoproton rate is calculated. Finally, the various background runs are subtracted and the cross section is extracted using a Monte-Carlo model of the spectrometer acceptance and a theoretical calculation of the bremsstrahlung spectrum. Details of the first two phases of the analysis are presented in this chapter.

A. Event Analysis

1. Tracking

The ten wire chambers positions are surveyed to ≈ 1 mm, and the positions of the wires within each chamber is known as accurately. All wire information within roughly 30 ns of the fast-trigger is converted into a digital form, which is then compressed before readout. Although the compression stores a maximum of 64 wire hit per event, rates were low enough that this limitation was not a problem. Pre-existing SLAC software, with some modification, was used to identify possible tracks in the chambers. (A track is a straight line that intersects hit wires within the resolution of the device). The algorithm first identifies tracks consistent with the P-chamber data. Any spurious tracks far outside the spectrometer acceptance are purged. Thus, with the vertical coordinate constrained a similar process is followed with the T-

chambers. To reduce the number of spurious tracks, a minimum of five chambers with at least two of each type had to be on the track. At this point the track is defined simply by its overlap with struck wires; it is then required to satisfy several criteria (purges), described below, that efficiently identify significant events and reject spurious signals. With the vertical and horizontal paths of the tracks defined, the position and direction (X_{fp}, dX/dZ_{fp}, Y_{fp}, dY/dZ_{fp}) at the focal plane are used to reconstruct the three-momentum of the proton at the target. The procedure used to determine the reconstruction coefficients is described in a later section.

The criteria that all tracks must satisfy are as follows:

- Good χ^2: The goodness of fit of a track is defined by $\chi^2 = 3\chi_x^2 + 3\chi_y^2$ where the x and y subscripts refer to the T- and P- chambers, respectively, and are normalized by the wire spacings.

- Good Fiducial: The track had to be contained within a fiducial region of the spectrometer that contained all the detector elements. This cut defines the spectrometer acceptance, and is included in the Monte Carlo simulation of the 8 GeV/c discussed in Section IV B.

- Good reconstruction: The values of $(\Delta P/P_0, \Delta\theta, \phi)$ reconstructed from the track must lie within the acceptance of the spectrometer.

- Good X-θ: The spectrometer optics are such that particles from the target have a linear X_{fp}-dX_{fp} correlation. This purge requires that the track's X_{fp} and dX_{fp} satisfy the correlation, within a tolerance.

- Good *scint*: It must be true that, for at least two of the three trigger-scintillator planes, the track intersects a counter that has fired.

- Good NBS: If a signal is detected in both the vertically-segmented and the

horizontally-segmented hodoscope scintillators, the track must point at one hodoscope segment that fired.

- Good Combo: A loose logical-*AND* of NBS and *scint.*

The good fiducial, good X-θ and good reconstruction purges are the most significant for the majority of the events, as they should be satisfied by 100% of the photoprotons and serve mainly to eliminate background events early in the analysis. The other purges can have non-zero inefficiencies so are applied loosely. Their purpose is to eliminate bad tracks in events with multiple tracks.

Although the trigger was a very efficient particle detector, it provided little background rejection, and the proximity of the SM and SR planes along with the high rates in the front plane resulted in a large accidental 3-fold coincidence rate. The fraction of events with no initial tracks ranged anywhere from 3% up to 95% depending on the spectrometer setting and the radiator status (in or out). Typically 50% of the triggers were accidental. The number of events with multiple tracks before purging was small, typically one percent of the number of events with tracks. (The maximum was 5%). Multiple tracks are caused either by the passage of two or more charged particles through the detector within $\approx$30 ns of the trigger, or by spurious tracks found to be geometrically consistent with the wire chamber data. The series of purges was used to select the physically significant track. If no single track could be selected, the event was assumed to be two real particles and the event was rejected. A multiple-track-correction factor is applied on a run-by-run basis to account for only one of the lost events—the other event will be counted in the dead-time correction. Typically less than 1/3 % of events fall into this category. (The maximum was 1.2%).

2. *Efficiencies*

The detection of protons by the 8 GeV/c spectrometer is not 100% efficient. Inefficiencies in single particle counting arise from the fluctuations in both the particle energy loss and the electronic amplification of the resulting signal. These effects apply to the scintillation counters, wire chambers and Čerenkov counter, although the latter was not used in the analysis. The detection of protons is also impaired by hadronic interactions (absorption and hard scattering) in, and before, the detector elements; this effect is discussed in Section IV F. In addition, the counting of particles at finite rates gives rise to dead-times caused by the overlapping of pulses in time and the inability to log more than one event per beam burst. The voltages on the scintillator-phototubes and the discriminator levels were adjusted before the experiment to yield near unit efficiency for the detection of minimum ionizing particles, while maintaining good rejection of spurious pulses. This is critical since the only trigger for the experiment is the 3-fold coincidence of the three scintillator planes, so that the trigger efficiency, ϵ_{TRIG}, is the product of the three efficiencies of the scintillator planes ($\epsilon_{\rm sf} \cdot \epsilon_{\rm sm} \cdot \epsilon_{\rm sr}$). The prescaled 2/3-coincidence trigger was designed to measure these efficiencies. A small fraction of the events are recorded requiring only a 2/3-trigger, then all the scintillators along the particle track are checked for pulses. The efficiency of a given scintillator can then be calculated as the ratio of the number of times it was hit by a particle to the number of times it fired. In principle one would like to do this on a run-by-run basis, so that the distribution of events used to calculate the efficiency reflects the distribution of the data. The statistics required for such a procedure precludes it from the analysis of this experiment. The high accidental rate for 2/3-scintillator coincidences, coupled with large prescaling, resulted in only 200 events with a track and a 2/3-trigger. The measured efficiency is 100% for all scintillator planes in all runs, but the statistics are poor.

The wire chamber efficiency can be calculated in a similar manner, except that all events with tracks can be used because the wire chamber information is not part of the trigger. The efficiency of each plane is calculated as the ratio of the number of times a wire chamber had a wire on a clean track to the number of clean tracks passing through the chamber. The results are shown in Figure 16. The tracking algorithm requires at least five chambers with at least two of each type firing; the total wire chamber efficiency is then calculated by summing all the possible configurations that satisfy this criterion, weighted with the probability of the configuration calculated with the 10 measured chamber efficiencies. The calculation can be done as a function of the total number of chambers required on the track, and extrapolated to five. Figure 16 also shows the result of the calculation along with an estimate from the data. The efficiency is consistently above 99.97%, and is calculable on a run-by-run basis.

3. Dead-time

Because events are defined by a digital level going *TRUE* for some length of time ($\tau = 20\,\text{ns}$), following an event the detector is unable to record another event for 20 ns. By counting events simultaneously with scalers that are incremented by logic levels of length τ, 2τ, 3τ and 4τ, one can estimate the true event rate from the scaler rate [40]:

$$\omega_{scaler}(\tau') = \omega \cdot e^{-\omega\tau'} \approx \omega \cdot (1 - \omega\tau'), \tag{3.1}$$

where τ' is the duration of the *TRUE* logic level, and ω is the true event rate. For the small hardware dead-times observed in this experiment, the linear approximation is entirely adequate. Thus, on a plot of scaler rate versus gate width, a linear extrapolation to $\tau = 0$ yields the actual event rate. A plot of the PROTON20–PROTON80 8 GeV/c scalers, summed over all the runs, versus the width of the input logic signal

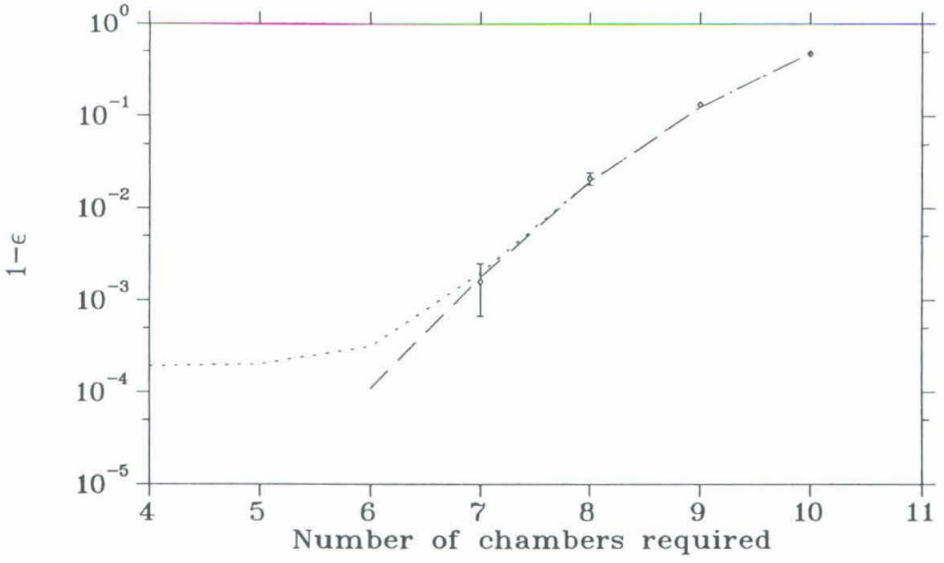

FIG. 16. Wire Chamber Efficiency

The data points in the figure show the measured total wire chamber efficiency ϵ versus the number of chambers required on the track. The dashed line is the expected results of the measurement, based on the measured efficiency of each chamber. The dotted line is a calculation of the true efficiency of the wire chambers; it differs from the dashed line because the sample of events used in the analysis was required to have at least 5 chambers on the track a priori.

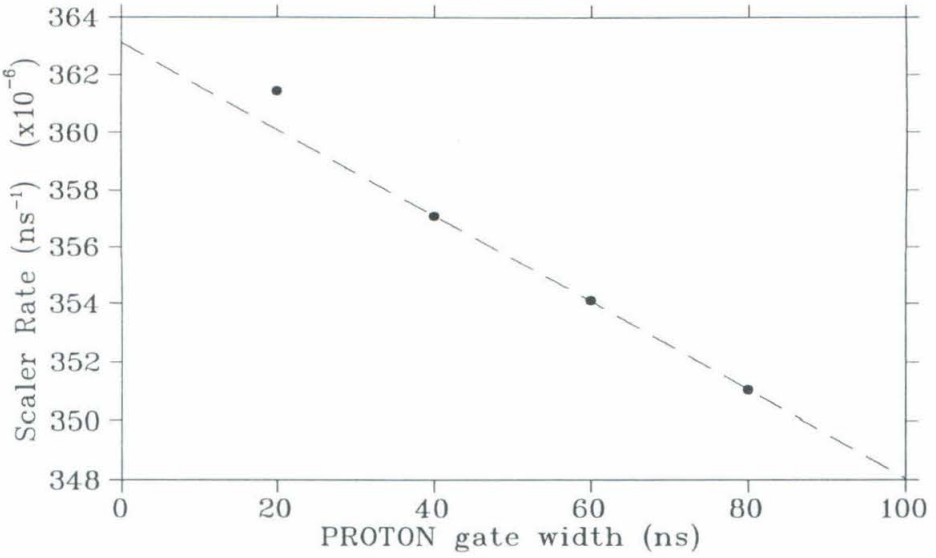

FIG. 17. Hardware Dead-time

The figure shows the measured PROTON scaler rates per ns versus the length of input logical signal. The dashed line is a linear fit of 40, 60, and 80 ns scalers, which is extrapolated back to zero to determine the actual number of pre-triggers caused by 3/3 scintillator coincidences. The 20 ns scaler is not used in the fit because of double pulsing of the discriminated signal.

(Figure 17) shows the linear relationship holds for all but the 20 ns scalers—probably because of double pulsing. Thus, in determining the actual number of events, only the 40 ns, 60 ns and 80 ns scalers are fit and extrapolated back to 0 ns.

Computer dead-time arises from the limited speed at which the PDP-11 can read data from the CAMAC interfaces. In a pulsed beam experiment such as NE 17, the computer is at most able to record only one event per beam spill, so that if there is more than one event during a beam spill, only the first is analyzed, and the subsequent events must be accounted for with a computer dead-time correction.

Data logging is started by the output of the trigger going to a logical *TRUE* state (see Figure 15). The trigger is fired by an input from the pre-trigger module—the

pre-trigger being the logical *OR* of all relevant events in the spectrometer—and then blocked for the remainder of the beam spill. The prescription that the computer dead-time is given by the ratio of the pre-trigger scaler to the trigger scaler, is not valid in this case because it rest on the assumption that all events going into the pre-trigger occur randomly and have no temporal correlation. The prescaled 2/3-trigger is the source of the problem. The prescaling is accomplished by taking the logical *AND* of the 2/3-coincidence with the prescaled beam gate. Thus, when the beam gate is blocked, the prescaled 2/3-coincidence does nothing, however when it is not blocked, all 2/3-coincidences increment the pre-trigger scaler—at a rate of 5/spill in some runs. So although the prescale factor is low, typically 2^{-8}–2^{-10}, and only a small fraction real events are missed, and PRETRIG/TRIG greatly overestimates the computer dead-time. Instead the ratio of PROTON scaler to the PROTON_{V} scaler is used. The proton scaler is incremented every time a 3/3-coincidence between the three scintillator planes, while the PROTON_{V} scaler was incremented for every 3/3-coincidence occurring when no trigger was already present. The product of this ratio with the hardware dead-time correction from Equation 3.1 gives the ratio of 3/3-coincidences occurring to the total number written to tape. Figure 18 shows the total dead-time correction versus run number. In principle this correction has no statistical error, since it is the ratio of two exact measured numbers, however since the fraction of triggers caused by real protons can be significantly less than one, there can be fluctuations in the actual number of protons missed. The largest uncertainty from this is 0.08% . The correction can also be estimated from statistical arguments: given an average of μ pre-triggers per spill, the expected dead-time correction factor is simply

$$f_{\text{dead-time correction}} = \mu/(1 - e^{-\mu}). \tag{3.2}$$

The comparison is shown in Figure 18; the two methods agree for all runs.

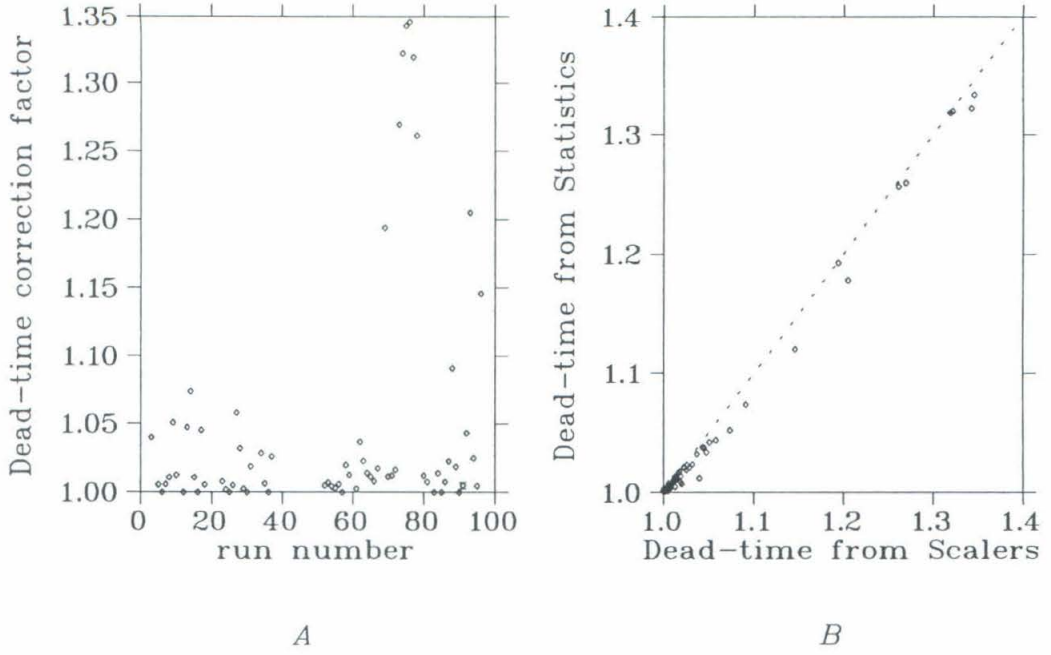

FIG. 18. Total Dead-Times

Figure (A) shows the total dead-time correction factors (hardware dead-time × computer dead-times) for all the runs taken in the experiment. The runs with large ($\approx 30\%$) corrections were taken with the 4.2 GeV beam. Figure (B) shows a run-by-run comparison of the exact dead-time with the statistical estimate from Equation 3.2. The exact dead-time is slightly higher than the estimate because the beam-spill in not uniform.

B. Particle ID

1. The Time-of-Flight Detector

The 3 planes of scintillators forming the fast trigger for the experiment were also used as a time-of-flight detector for particle ID—by combining the momentum measurement from tracking and the velocity measurement from time-of-flight, the mass of the particle can be reconstructed. The detector was designed for π^+-p separation, which is difficult at momenta much larger than M_p, however the significant background at low photoproton-momentum kinematics is from deuterons, making separation relatively easy. At high momenta (forward angles) the deuteron rates are low, and the most significant background is from accidentals—particles that have penetrated detector shielding and show no ToF peak (see Section V G).

2. Measuring Particle Velocity

The measurement of the particle velocity β is achieved by fitting the linear relationship between the time at which the particle crosses the scintillator plane versus the Z_{hut} coordinate of the plane. With Z_{hut} defined as the direction perpendicular to the planes, the relationship is

$$t^i = mZ^i_{hut} + b \tag{3.3}$$
$$m = \sqrt{1 + (dX/dZ)^2 + (dY/dZ)^2}(\frac{1}{c\beta}).$$

The constants m and b are fit with a simple un-weighted linear regression. Here dX/dZ and dY/dZ are the measured slopes of the track in the two direction orthogonal to Z_{hut} (Y_{hut} is vertical, X_{hut} is horizontal), and c is the speed of light. The times t^i, where i labels the scintillators that fired along the track, are measured with respect

to the 8 GeV/c trigger time using 50 ps/channel TDCs. (Each TDC module was calibrated before the experiment). The trigger starts the TDC, which is subsequently stopped by the discriminated PMT signal, so that the time is given by

$$t^i = C^i + \Delta Y/v_{scint} + PHC. \tag{3.4}$$

The constant offsets C^i account for differences in the cable lengths and intrinsic response times of the various phototubes. The correction $\Delta Y/v_{scint}$ accounts for the propagation of scintillation light through the detector. The speed of light in the scintillator is typically $\approx$ 12 cm/ns; ΔY can be as large as 100 cm, so that this correction is large. The pulse height correction PHC, typically a few ns, corrects for the slewing of the discriminated phototube signal, and is adequately described by the functional form (see Figure 19):

$$PHC = P\sqrt{\max(A_{PMT}, A_0)}. \tag{3.5}$$

The fits to the parameters in Equation 3.5, *i.e.*, the various C^i's, v_{scint}'s, P's, A_{PMT}'s and A_0's, used in this analysis were done using the large body of proton events available from NE 18. The fitting procedure, described in detail in [35], is subtle; parameters for each PMT were fit independently with an iterative procedure, using initial values of the various parameters measured before the experiment. The resulting timing resolution is $\sigma_{\rm ToF} \approx 150$ ps, with a corresponding velocity resolution given by

$$\sigma_\beta \approx \beta^2 \sigma_{\rm ToF}(c/\Delta Z), \tag{3.6}$$

where ΔZ=3.86 m is the length of the ToF package.

Several steps were taken to achieve good β resolution: The SR scintillators was moved to the back of the detector hut to increase ΔZ; the SM plane was also pushed back to increase the sensitivity of the fit (Equation 3.3) to β. The size of σ_{ToF} is largely determined by the intrinsic phototube timing resolution, scintillator quality—because

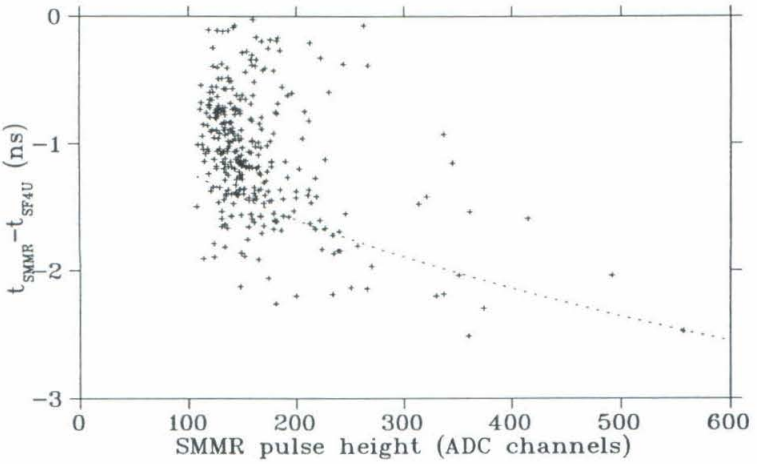

FIG. 19. Pulse Height Correction

The figure shows the effect of slewing. The difference between the time at focal plane measured with the SF4U scintillator and that measured with the SMMR without the pulse height correction is plotted versus the SMMR pulse height.

of light attenuation, and the number of time measurements t_i. A large (≈ 100) sample of phototubes were tested before the experiment, and only the best were selected for use; BC-420 fast-scintillator material was also purchased and tested. The scintillator was chosen because it has both a fast decay time and a long attenuation length. The three detector planes typically provided 6 timing measurements, however the number can be as high as 12 because of the physical overlap of the elements in each plane. A good time-of-flight can be fit with only 4 measurements, provided 2 are from the SF. If the SF measurements were lost, usually because of spurious hits prior to the trigger-event, no ToF could be fit. Timing measurements are accepted in the analysis provided the following criteria are satisfied:

- The detector must have good ADC and TDC measurements. The ADC pulse must be 30 channels or more, and the associated TDC measurement must lie between channels 2 and 1500.

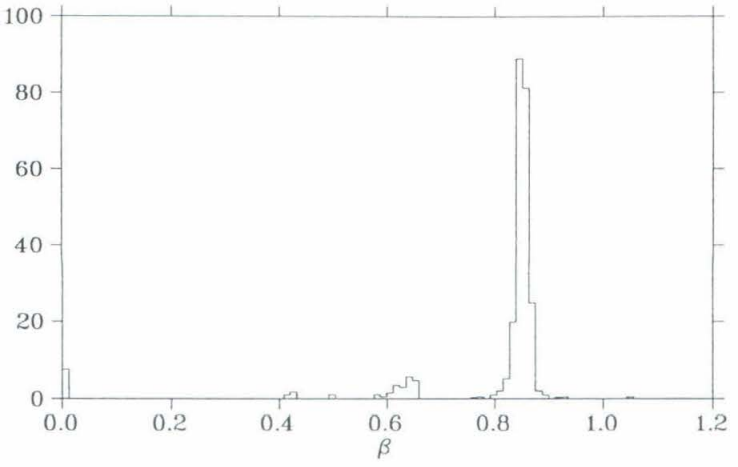

FIG. 20. Time-of-Flight Spectrum

The figure shows a β spectrum of photoproton from $\gamma d \rightarrow np$ along with background protons, deuterons and tritons from the Al target windows. The central momentum of the spectrometer is 1.505 GeV/c.

- The X_{hut} and Y_{hut} position of the track at the scintillator plane must lie within the extent of the detector segment under consideration. If no such segment in the plane satisfied this condition, then the track must lie within 1 cm of the segment.

- The timing measurements from both phototubes on the detector segment under consideration must agree within a tolerance.

Figure 20 shows a β spectrum measured with the deuterium target and the radiator present. The proton and deuteron peaks are clearly separated, and particle ID cuts are placed on the β-spectrum, instead of the reconstructed mass, without loss of signal-to-noise. The p-d peak separation at low momentum is large enough that the dispersion in β over the momentum acceptance of the spectrometer is not significant. At high momentum, the dispersion is less, and the largest component of the background is accidentals, which have no peak in β. The events in the $\beta = 0$ bin

are events in which no time-of-flight could be measured and are the main source of inefficiency in the particle ID. Time of flight efficiencies ranged from 90%-100%. The data were analyzed both without the no-ToF events and an efficiency correction, and with the no-ToF events accepted. Furthermore, the analysis was done with varying particle-ID cuts; the rates varied within 4%, indicating accuracy of the particle ID.

IV. SPECTROMETER CALIBRATION

Systematic studies of the 8 GeV/c spectrometer are discussed in this chapter. The spectrometer was run for the first time in a non-standard tune, the large-acceptance-tune; that is, with the current in the first two quadrupoles reversed with respect to the normal tune. The change increases the solid angle from ≈ 0.75 msr to ≈ 3.2 msr, and thus allows the accumulation of the required statistics for the experiment in a much shorter time. Unfortunately, the sensitivity of the optical properties to the absolute field strength and shape in the quadrupoles is significantly increased. In fact, the uncertainties were such that a self-consistent model of the spectrometer could not be obtained at the few percent level. To minimize systematic errors in the final cross section the following procedure was adapted. A Monte Carlo model of the spectrometer is used to calculate the effective solid angle. The model is chosen to best reproduce the focal plane distributions observed in p(e,e'p) and p(e,e')p data. The best-fit reverse matrix elements of the model, however, are not used to reconstruct the data. The data are reconstructed with reverse matrix elements that have been adjusted to fit kinematic constraints in p(e,e'p) measurements [35]. The procedure is justified by its success in describing the well known p(e,e')p reaction.

After a summary of the coordinate systems used in the analysis, the Monte Carlo model of the spectrometer is discussed. The procedure used to measure the ^{2}H(γ,p)n cross section, outlined above, is tested with the p(e,e')p reaction. The measurement of the elastic cross section is explained, followed by a comparison with the World data. Then, using a differential radiative correction procedure (de-radiation), the p(e,e')p reaction is used to calculate the size of the uncertainties in the spectrometer optics. Finally, the ^{2}H(γ,p)n is discussed. The solid angles calculated using the Monte Carlo are given for each kinematics, and the correction for the nuclear-absorption of protons is discussed.

A. 8 GeV/c Coordinates

Before discussing the 8 GeV/c model it is important to clarify the coordinates used at various stages in the analysis. The coordinates necessary to describe the scattering of the detected particle are the scattering position at the target $(X_{targ}, Y_{targ}, Z_{targ})$ and the momentum $\mathbf{p_f}$. The origin is at the target center, with Z_{targ} along the beam direction. The angular coordinates of the momentum vector (θ_f, ϕ_f) are the usual polar angles defined relative to the initial beam direction: $\cos\theta_f = p_{f,z}/|\mathbf{p_f}|$ is the production angle, and ϕ_f is the azimuthal angle. The standard spectrometer-target coordinates $\theta_t = \theta_0 + \Delta\theta$ and $\phi_t = \phi$, where θ_0 is the central angle setting of the spectrometer, are not the same. They are related by:

$$\begin{aligned} \cos\theta_f &= \cos\theta_t \cos\phi_t \\ -\tan\phi_f &= \tan\phi_t / \sin\theta_t. \end{aligned} \tag{4.1}$$

The magnitude of the momentum is defined in terms of the momentum setting of the spectrometer:

$$\Delta P/P_0 = \frac{(|\mathbf{p_f}| - P_0)}{P_0}. \tag{4.2}$$

There is also a transport coordinate system, $(X_{trans}, Y_{trans}, Z_{trans})$, that is defined relative to the optic axis of the spectrometer. The origin is at the central target position, with Z_{trans} parallel to the optic axis of the spectrometer; X_{trans} points down in the bend plane and Y_{trans} is perpendicular to the bend plane with a right-handed sense.

In the detector hut the coordinate system $(X_{hut}, Y_{hut}, Z_{hut})$ is left-handed and orthogonal; Z_{hut} is collinear with the central ray, Y_{hut} is up and X_{hut} points to the south (beam right). The origin is the intersection of the central ray and the true momentum focal plane. A trajectory through the detector is described by the four quantities:

$$
\begin{aligned}
X_{fp} &= X_{hut}(Z_{hut} = 0) \\
dX_{fp} &= \frac{dX_{hut}}{dZ_{hut}}(Z_{hut} = 0) \\
Y_{fp} &= Y_{hut}(Z_{hut} = 0) \\
dY_{fp} &= \frac{dY_{hut}}{dZ_{hut}}(Z_{hut} = 0).
\end{aligned} \tag{4.3}
$$

The six unknowns of a scattering event, the interaction point $(X_{targ}, Y_{targ}, Z_{targ})$—or equivalently $(X_{trans}, Y_{trans}, Z_{trans})$—and the momentum given by $(\Delta P/P_0, \Delta\theta, \phi)$, are reduced to four measured quantities in the detector hut: $X_{fp}, dX_{fp}, Y_{fp}, dY_{fp}$. For the purpose of reconstruction, X_{trans} and Z_{trans} are set to zero and the four remaining unknowns are calculated as second and third order polynomials in the focal plane quantities. The coefficients of these polynomials are the reconstruction matrix elements. The assumption $X_{trans} = 0$ is good, and the beam's vertical extent is ≈ 1 mm. $Z_{trans} = 0$ is not strictly true unless the spectrometer sits at $\theta_0 = 90°$, however the approximation is good. Because $\delta\theta_t \ll 1$ and $\phi_t \ll 1$, the scattering position along the target is well approximated by:

$$
Z_{targ} = Y_{trans}/\sin\theta_0. \tag{4.4}
$$

1. Energy Loss

The reconstruction matrix elements relate the measured focal plane quantities to spectrometer-target quantities. Using Equation 4.2 one can then obtain the momentum vector of the scattered particle, p_f. The particle, however, passes through target material and vacuum windows, thus losing energy in atomic collisions, before entering the 8 GeV/c magnetic optics, and a correction to the measured energy must be made. For protons moving speed $\beta = v/c$ the mean energy loss from collisions with atomic electrons is given by [41]:

$$\Delta E = 4\pi N_A r_e^2 m_e c^2 \frac{Z}{A}\frac{\rho}{\beta^2}\log\frac{2m_e\beta^2\gamma^2}{I}. \tag{4.5}$$

Here A and Z are the atomic weight and number of the material; ρ its density. The ionization constant, I, is given to 10 % by $I = 16Z^{0.9}$ eV, $Z > 1$. For liquid hydrogen and deuterium we use the value 21.8 eV [5]. The amount of material traversed by the proton is calculated assuming it originated at the center of the target. Typical energy losses for kinematics of this experiment were from 2–4 MeV.

B. The 8 GeV/c Model

A Monte Carlo computer program was written to compare measured data with the 8 GeV/c model. Events are generated at the target position in a six dimensional phase space. The three dimensions representing the initial position of the events are chosen independently, with the position along the target (Z_{targ}) chosen uniformly and the horizontal and vertical coordinates (X_{targ} and Y_{targ}) given by separate Gaussian distributions truncated at $\pm 3\sigma$ (σ =0.2 mm). The other three coordinates, $(\Delta P/P_0, \Delta\theta, \phi)$, representing the trial event's momentum, could be chosen independently and uniformly, or with a distribution representing a physical process (e.g., elastic p(e,e')p scattering discussed in Section IV C). After transforming from the standard physical coordinates to spectrometer-target coordinates, the event is propagated forward through magnetic elements using Transport [42]. (Details of the Transport model are given in Table IV). The trajectory is checked against apertures at various points in the magnetic system: 69.13 cm into Q81, the circular end face of Q82, and the end flange of Q83. Events that pass through the magnet system are propagated into the detector hut. Trajectories are checked against the known wire chamber and scintillator positions. Events passing through enough wire chambers (five) and scintillators (three) are accepted as good events, and are then characterized by their trajectory parameters at the effective focal plane: $X_{fp}, dX_{fp}, Y_{fp}, dY_{fp}$.

Normally distributed Gaussian random numbers with widths 0.23 cm, 2.8 cm, 0.10 cm and 1.25 cm, respectively, are added to the focal plane quantities to simulate the resolution of the wire chambers. Events that then fail the fiducial cuts, which are based on the projection of the track through the detector elements, are rejected (c.f. Section III A 1). Multiple scattering from vacuum windows and detector materials is treated in the Gaussian approximation [5]—Gaussian random numbers are added to the trajectory's two angular coordinates. Energy loss from ionization is simulated by subtracting the most probable energy loss given by Equation 4.5 and Equation 4.9 for protons and electrons, respectively.

Ideally, a successful Transport model will accurately reproduce measured focal plane distributions *and* yield reverse matrix elements that reconstruct data in a physically consistent manner. With p(e,e′)p reaction, for instance, the momentum and angle of the detected electron are correlated such that

$$\frac{1}{E_f} - \frac{1}{E_i} = \frac{(1 - \cos\theta_f)}{M_p}, \tag{4.6}$$

where the E's are the energies of the initial and final electrons, and θ_f is the angle between them. Various Transport models were tested with the constraints that they adequately reproduce the focal plane distributions measured in p(e,e′)p data, and also that the data, as reconstructed with the best-fit reverse matrix elements of the model, satisfy Equation 4.6. Both second and third order models with various quad strengths were extensively tested. The absolute strengths ($\int \mathbf{B} \cdot d\mathbf{l}$) of Q82 and Q83 relative to the bending magnets is determined to 0.5% in off-line measurements after the experiment, and that of Q81 is known to 0.3% [43]. Run-to-run averages were measured with a transducer, stored in registers and written to tape. Fluctuations in the field strengths were less than 0.1 % on average. In the Transport model, the strengths of Q82 and Q83 were varied by $\pm 0.5\%$ and Q81 by $\pm 0.3\%$. The final model has the nominal quad strengths and is second order, and was chosen because it best

TABLE IV. The Second Order Transport Model

Object	Length (m)	Field[I] (kG)	1/2 Apperture (cm)	Rotation Angles[III] magnet,pole face	Fringe Field correction coeff.
GAP			$X \times Y = 64.13 \times 17.50$		0.518
DRIFT	2.3178				
Q81 (quad)	1.03693	-8.412	13.97		
DRIFT	0.9274				
Q82 (quad)	1.3385	5.3292	19.37		
DRIFT	0.9692				
B81 (bend)	3.6183	7.24040[II]		−90°, 7.5°	
DRIFT	1.01540				
B82 (bend)	3.6183	7.24040[II]		−90°, 7.5°	
DRIFT	0.7194				
Q83 (quad)	1.3385	-3.0986	19.37		

[I] Field strengths are for $P_0 = 3.000\,\mathrm{GeV/c}$.

[II] The field gradient n-value is 0.

[III] Magnet rotations are followed by and equal rotation of oppostie sign; pole tip rotations are the same sign at the entrance and exit of the magnet.

fit p(e,e′)p focal plane distribution, as shown in Figure 21. The model adequately reproduces the widths and normalization of the data, reflecting an accurate modeling of both the spectrometer's apertures and magnification. Agreement with Equation 4.6, however, is not entirely satisfactory, and the Transport matrix elements were not used to reconstruct the data.

Using p(e,e′p) and d(e,e′p)n coincidence data taken during the NE 18 experiment, complete sets of matrix elements, for both the 8 GeV/c and 1.6 GeV/c spectrometers were determined independently from the Transport model. The details are described elsewhere [35]. The matrix elements, shown in Table V, provide a physically consistent reconstruction of the data, which is particularly important for this experiment because the measurement of the ^{2}H(γ,p)n cross section requires an accurate reconstruction of the photon energy from the measured photoproton momentum.

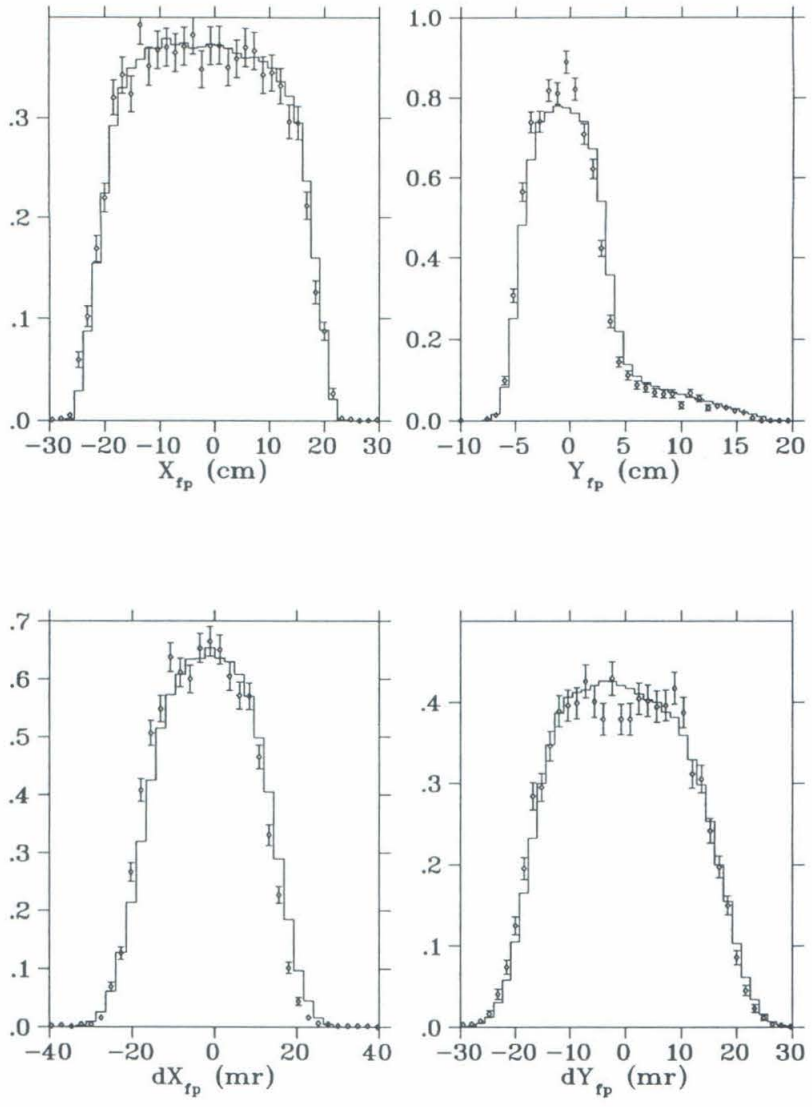

FIG. 21. p(e,e′)p Focal Plane Distributions

A comparison of the focal plane distributions (X_{fp}, Y_{fp}, dX_{fp}, dY_{fp}) measured in p(e,e′)p with the Monte Carlo model of the spectrometer is given in the figures. The data, for the 4 cm target, include the dummy subtraction. The model p(e,e′)p distribution used in the Monte Carlo, developed in [35], *has fixed normalization determined from Equation 4.7 and includes radiative processes.*

TABLE V. Matrix Elements used in Data Reconstruction

	$\Delta P/P_0$	$\delta\theta$	ϕ
	%	mr	mr
1[†]	0.15–0.17	1.2–0.7	4.0–1.2
X_{fp} (cm)	$+1.00 \times 10^{-3}$	$+8.90 \times 10^{-1}$	
dX_{fp} (mr)	-6.50×10^{-3}	-1.50×10^{-2}	
Y_{fp} (cm)	-3.95×10^{-1}		-1.036×10^{0}
dy_{fp} (mr)	$+4.00 \times 10^{-3}$	-3.30×10^{-2}	-2.75×10^{0}
X_{fp}^2	-1.70×10^{-3}	$+1.00 \times 10^{-3}$	
$X_{fp}dX_{fp}$	$+4.30 \times 10^{-3}$		
$X_{fp}Y_{fp}$	-1.00×10^{-3}	1.70×10^{-2}	
dX_{fp}^2	-2.50×10^{-3}		
Y_{fp}^2	$+4.00 \times 10^{-3}$		-2.80×10^{-2}
$Y_{fp}dY_{fp}$	$+4.00 \times 10^{-3}$		$+6.60 \times 10^{-2}$
dY_{fp}^2	-1.50×10^{-4}	$+6.00 \times 10^{-3}$	$+5.00 \times 10^{-5}$
$X_{fp}^2Y_{fp}$	-7×10^{-5}	$+4 \times 10^{-4}$	
$X_{fp}Y_{fp}^2$		1×10^{-3}	

[†] The constant offsets were fit to the p(e,e'p) data, and account for misalignment of the detector hut and errors in the absolute calibration of the spectrometer. They have a small momentum dependence.

C. Measurement of the p(e,e′)p Cross Section

The p(e,e′)p reaction has been extensively investigated experimentally and is well understood theoretically up to momentum transfers of $\approx 9(\mathrm{GeV/c})^2$ [44,45]. It is an ideal reaction for studying the 8 GeV/c spectrometer optics and acceptance. Data were taken at squared-four-momentum transfers of $\approx 1\,\mathrm{GeV}^2/\mathrm{c}^2$ during both the E140x and NE 18 checkout phases [34,35]. The E140x checkout comprises a momentum scan, in which the elastic peak in $\Delta P/P_0$ is swept across the momentum focal plane by stepping the dipole current. The NE 18 data are two consecutive runs at identical kinematics with the 4 cm and 15 cm targets, providing a test of the acceptance for extended targets, vital to the understanding of the ^{2}H(γ,p)n cross-sections. A summary of the p(e,e′)p data is given in Table VI.

1. The Born Approximation

In the Born-level approximation, the inclusive cross section for the elastic scattering of electrons from protons is given by the Rosenbluth formula [17]:

$$\left(\frac{d\sigma}{d\Omega}\right)^{1-\gamma} = \left(\frac{d\sigma}{d\Omega}\right)_{Mott} \left[\frac{G_E^2(q^2) + (q^2/4M_\mathrm{p}^2)G_M^2(q^2)}{1 + q^2/4M_\mathrm{p}^2} + q^2/4M_\mathrm{p}^2 \cdot 2G_M^2(q^2)\tan^2\frac{1}{2}\theta\right], \tag{4.7}$$

$$\left(\frac{d\sigma}{d\Omega}\right)_{Mott} = \frac{Z^2\alpha^2\cos^2\frac{1}{2}\theta}{4p_i^2\sin^4\frac{1}{2}\left[1 + (2p_i/M_\mathrm{p})\sin\frac{1}{2}\theta\right]}. \tag{4.8}$$

Here $G_E(q^2)$ and $G_M(q^2)$ are the electric and magnetic form-factors of the proton, respectively, and q_μ is the four-momentum of the virtual photon. Various parameterization of the proton form-factors can be found in the literature [44]. Based on the results of NE 11 [46], the World data are best described at $-q^2 \approx 1\,\mathrm{GeV}^2/\mathrm{c}^2$ with the standard dipole form for $G_E(q^2)$ [17] and the Gari-Krumpelmann parameterization

TABLE VI. Summary of p(e,e′)p Runs

Run	E (GeV)	θ_0	P_8 (GeV/c)	Target
NE-18, 4	2.015	40.723°	1.320	4CM_LH2
NE-18, 5	2.015	40.723°	1.320	4CM_DUM
NE-18, 6	2.015	40.723°	1.320	15CM_LH2
NE-18, 7	2.015	40.723°	1.320	15CM_DUM
E140x, 271	1.9958	37.023°	1.3582	4CM_LH2
E140x, 272	1.9958	37.023°	1.3795	4CM_LH2
E140x, 273	1.9962	37.023°	1.3797	4CM_LH2
E140x, 278	1.9958	37.023°	1.4005	4CM_LH2
E140x, 282	1.9962	37.023°	1.4418	4CM_LH2
E140x, 274	1.9962	37.023°	1.3795	4CM_DUM
E140x, 275	1.9962	37.023°	1.3797	4CM_DUM
E140x, 280	1.9966	37.023°	1.4001	4CM_DUM
E140x, 281	1.9962	37.023°	1.4001	4CM_DUM

TABLE VII. Born-level Cross Sections for p(e,e′)p

E_{beam} (GeV)	θ_0	Q^2 (GeV/c^2)	$d\sigma/d\Omega$ (nb/sr)
2.015	40.723°	1.294	3.064
1.9958	37.023°	1.124	6.116

of $G_M(q^2)$ [47]. The parameterizations of the cross section at the kinematics of the check out data, shown in Table VII, are good to 2%.

2. Yield from p(e,e′)p

Yield from the p(e,e′)p reaction is measured by subtracting the dummy target scattering yield from the hydrogen target scattering yield. Rates are normalized by the total integrated-luminosity (total charge × nucleons/nb) with all the various corrections applied (i.e., dead-time, target shrinkage, isotopic purity, efficiencies, multiple tracks, etc.). A factor of 9.5 is included in the dummy target luminosity because of the relative thickness of the aluminium seen by the spectrometer (see Table II). The yield from Al(e,e′)X was typically 2-3% that of p(e,e′)p for the 4 cm target, and proportionally smaller for the 15 cm target.

The same target quantity cuts used in the ^{2}H(γ,p)n analysis are used: $|\delta\theta| < 15\,\text{mr}$, $|\phi| < 50\,\text{mr}$ and $|\Delta P/P_0| < 5\%$. Events are then corrected for energy losses from ionization: An electron passing through a thickness τ of material with density ρ undergoes collisional energy loss with a most probable value given by [41]:

$$\Delta E = 4\pi N_A r_e^2 m_e c^2 \frac{Z}{A}\tau\,(19.28 + \log\tau/\rho)\,, \tag{4.9}$$

where Z and A are the atomic number and weight of the material. The scattering is assumed to take place on average at the center of the target, and the calculated energy losses are added to the measured energy of the scattered electron and subtracted from

the initial beam energy. The data are then histogrammed in the squared-missing-mass, which measures the mass of the undetected hadronic state:

$$W^2 = (P_\mu + q_\mu)^2 = M_{\rm p}^2 + 2M_{\rm p}\nu - Q^2,$$

$$\nu = E - E' \tag{4.10}$$

$$Q^2 = -q_\mu^2 \approx 4EE' \sin^2 \frac{\theta}{2}.$$

Here E and E' are the energies of the initial and final electrons, and θ is the angle between their three-momenta in the lab-frame. For elastic scattering in the Born approximation, the constraint $Q^2 = 2M_{\rm p}\nu$ holds so that the proton mass is recovered. A typical W^2 histogram is shown in Figure 22. The normalization is given by

$$\left(\frac{d\sigma}{dW^2}\right)^{\rm raw} ({\rm nb/GeV^2}) = \frac{e}{Q_{eff}} \frac{1}{n_{nucl}} \frac{N_{W^2}}{\delta W^2_{\rm bin}} \frac{1}{\epsilon}, \tag{4.11}$$

where e is the electron charge, Q_{eff} is the dead-time corrected integrated beam current, n_{nucl} is the target density (protons/nb), N_{W^2} is the raw histogram and $\delta W^2_{\rm bin}$ is the histogram bin width in GeV^2. The factor ϵ^{-1} is a 1% efficiency correction. (The yield in the super-elastic region, $W^2 < M_{\rm p}^2$, which is populated only by events from the target end-caps, is consistent with zero.) The measured yield is then given by

$$Y = \int_{W^2_{\rm SE}}^{W^2_{\rm cut}} dW'^2 \left(\frac{d\sigma}{dW'^2}\right)^{\rm raw}, \tag{4.12}$$

where $W^2_{\rm SE}$ is the super-elastic cut chosen below the elastic peak, and $W^2_{\rm cut}$ is an upper cutoff that must be chosen below the pion-production threshold at $W^2 = (M_{\rm p} + m_{\pi^0})^2 = 1.152\,{\rm GeV^2}$. The dependence of Y on $W^2_{\rm cut}$ is discussed below.

3. Radiative Corrections

The tail at $W^2 > M_{\rm p}^2$ in Figure 22 is caused by diagrams involving real photon emission from the incoming and outgoing electron lines: both E and E' are reduced,

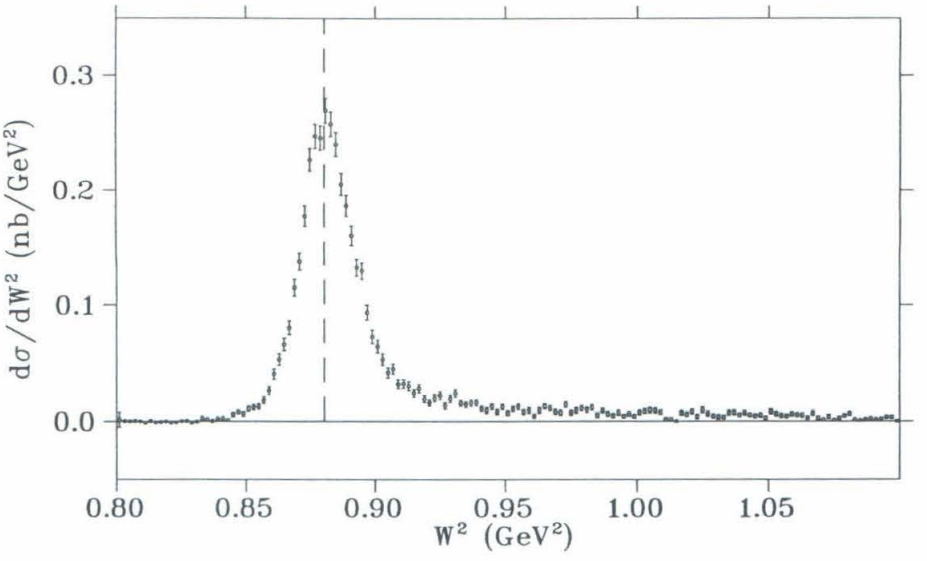

FIG. 22. Raw W^2 Histogram

The figure shows a raw missing mass-squared histogram measured in elastic electron-proton scattering.

thereby increasing the measured value of W^2. The radiative tail extends up to the maximum value given by $W^2 \approx 2M_{\rm p}E$, but is cut off by spectrometer acceptance. Thus the measured yield differs from that predicted by the Rosenbluth formula.

The correction for the radiative tail has been extensively investigated by several authors [48,49]. The general prescription is to define a cutoff-dependent function RCOR$[W^2_{\rm cut} - M^2_{\rm p}]$ that represents a fractional correction for yield lost above the cut. That is, the one-photon-exchange (Born-level) cross-section is given in terms of the measured cross-section by:

$$\left(\frac{d\sigma}{d\Omega}\right)^{1-\gamma} = (\mathrm{RCOR}[W^2_{\rm cut} - M^2_{\rm p}])^{-1} \times \left(\frac{d\sigma}{d\Omega}\right)^{\rm raw}, \tag{4.13}$$

where

$$\left(\frac{d\sigma}{d\Omega}\right)^{\rm raw} = \frac{Y}{\Delta\Omega_{p(e,e')p}}. \tag{4.14}$$

Here $\Delta\Omega_{p(e,e')p}$ is the effective solid angle of the spectrometer, discussed in Section IV C 4.

We use the integral radiative correction of Mo and Tsai [49]. They express their result in terms of E, E' and θ. The conversion to W^2 is done by solving Equations 4.10 for E' with E fixed at the beam energy and θ fixed at the central spectrometer angle. The error introduced by neglecting the variation in the radiative correction over angular acceptance of the spectrometer was investigated and is negligible. Mo and Tsai evaluate diagrams with one external photon and 1-loop diagrams, giving the fractional radiative correction as $(1 + \delta_{int})$. (Note that $\delta_{int} < 0$). Higher order diagrams are approximated by exponentiating the first-order correction. Straggling from bremsstrahlung in the target materials is included with an additional correction δ_{ext}, so that the radiative correction is given by:

$$\mathrm{RCOR}[W^2 - M_\mathrm{p}^2] \equiv \exp\left(\delta_{int}(E') + \delta_{ext}(E')\right), \tag{4.15}$$

with

$$E' = \frac{M_\mathrm{p}^2 + 2M_\mathrm{p}E - W^2}{2M_\mathrm{p} + 4E\sin^2\theta/2}. \tag{4.16}$$

4. Solid Angle Calculation

The solid angle is calculated from the Monte Carlo program described in Section IV B. Events are generated according to the expected p(e,e')p distribution and propagated through the Monte Carlo and reconstructed with the second-order matrix elements fit to the Transport model. The method used to model the p(e,e'p) reaction, including radiation, is developed in [35]. Agreement with data is shown in Figure 21. The same cuts that are applied to the data are applied to the Monte Carlo events. The average solid angle is then determined by:

$$\Delta\Omega_{p(e,e')p} = (\Delta\theta\Delta\phi) \times N_{final}/N_{initial}, \tag{4.17}$$

where $\Delta\theta\Delta\phi = 3\,\mathrm{msr}$ are given by angular cuts ($30\,\mathrm{mr} \times 100\,\mathrm{mr}$). $N_{initial}$ is the number of trial events generated within the applied cuts, and N_{final} is the number of events *reconstructed* within the cuts after propagation through the Monte Carlo. The Monte Carlo was run—with negligible systematic error—for each of the spectrometer and target configurations listed in Table VI.

5. Measured Cross Section

The super-elastic cut was chosen at $W^2_{\mathrm{SE}} = 0.84\,\mathrm{GeV}^2$, and the cutoff at $W^2_{\mathrm{cut}} = 0.96\,\mathrm{GeV}^2$. Because of the high central momentum of run 282, the cut was put at $W^2_{\mathrm{cut}} = 0.94\,\mathrm{GeV}^2$ so that the cutoff is not determined by the spectrometer acceptance. The measured cross-sections appear in Table VIII.

6. Momentum Scan

Because of the kinematic correlation between θ_f and $|\mathbf{p_f}|$ given by Equation 4.6, the p(e,e')p reaction illuminates a limited portion of the detector stack, referred to as the elastic stripe. To first-order $\delta\theta$ (X_{fp}) and $\Delta P/P_0$ (Y_{fp}) are linearly correlated, with all values of $\delta\theta$ (X_{fp}) populated and a limited region of $\Delta P/P_0$ (Y_{fp}) populated at each setting. As the magnet current is increased, the stripe moves across the detector stack from positive (negative) values of $\Delta P/P_0$ (Y_{fp}) to negative (positive) values. Measurement of the cross-section versus the position of the elastic stripe test the spectrometer acceptance versus $\Delta P/P_0$. The measured yields, calculated solid angles, and radiatively corrected cross-sections appear in Table VIII. (Also see Figure 23). The data are consistent with the parameterization of te World data, except at the highest value of $\Delta P/P_0 \approx 3\%$. Photoprotons from ^{2}H(γ,p)n illuminate

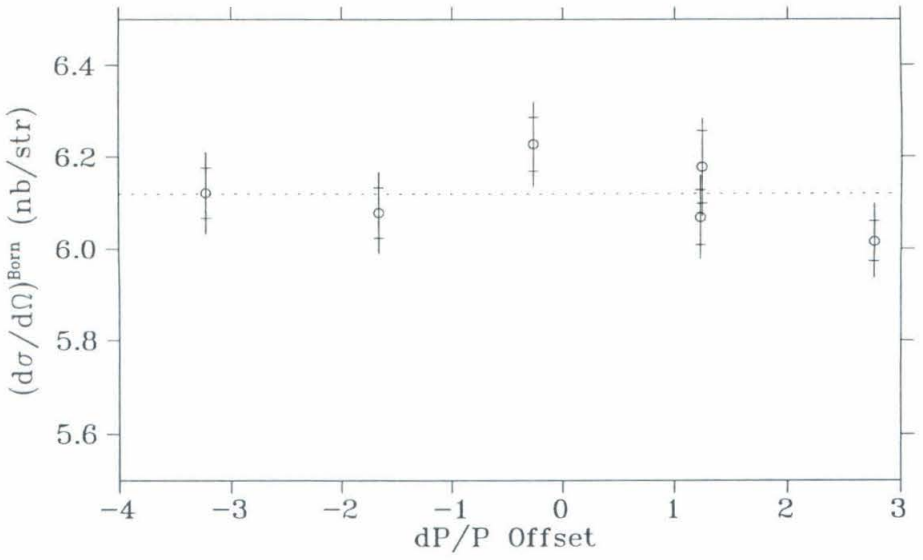

FIG. 23. Results of the Elastic Scan

The figure shows the measured p(e,e')p cross sections in the elastic scan. The inner error bars are statistical, with a 1% systematic error (for the radiative correction and 1% efficiency correction) added in quadrature to give the total error bar. The dashed line is the theoretical value.

a limited $\Delta P/P_0$ region of the spectrometer, and at none of the kinematics does this region extend beyond -3.8%< $\Delta P/P_0$ <2%, so that the no momentum dependent acceptance correction is required.

7. Extended Target Acceptance

The acceptance of the spectrometer depends on the target position, and is expected to be constant only within the region defined by $|Y_{trans}| < 3\,\text{cm}$. (See Figure 24). Data for NE 17, however, were taken with $|Y_{trans}|$ as large as 6.26 cm, so that an understanding of the acceptance for large Y_{trans} is required. Elastic *ep* data were taken at $\theta = 40.723^{\circ}$ with both the 4 cm target and 15 cm target under

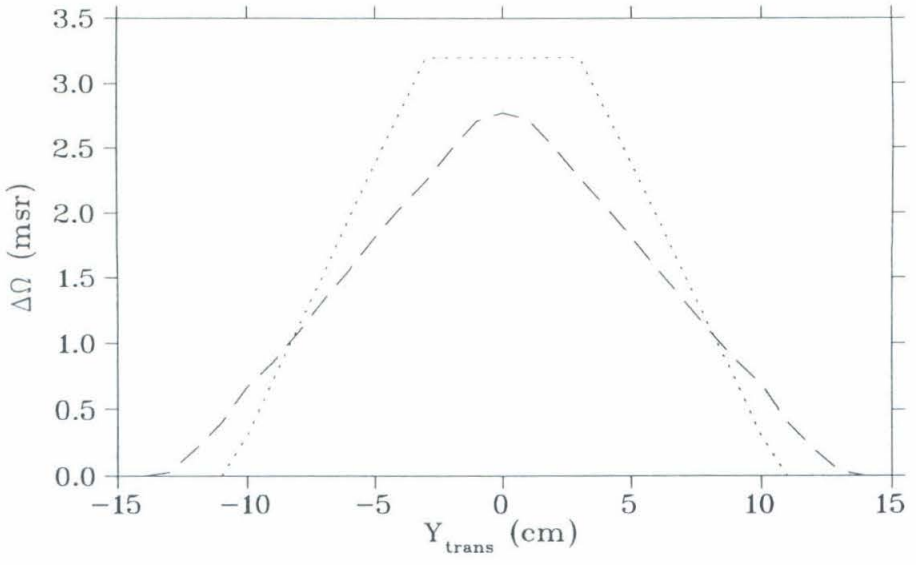

FIG. 24. Extended Target Acceptance

The figure shows the spectrometer solid angle versus Y_{trans}. The dotted line is for $\Delta P/P_0 = 0\%$, while the dashed line averages over $|\Delta P/P_0| \leq 3\%$.

identical circumstances, thereby reducing systematic uncertainties in their comparison. The extent of the 15 cm target in the optical coordinates of the spectrometer is $\Delta Y_{trans} = \Delta Z_{targ} \sin\theta_0 = \pm 5.16$ cm. The results appear in Table VIII. The radiatively corrected measured yields are 7.966 ± 0.0098 pb and 6.981 ± 0.0082 pb for the 4 cm and 15 cm targets, respectively, while the solid angles calculated from the 8 GeV/c model are 2.600 msr and 2.266 msr. Thus the two measurements of the cross section, 3.06 ± 0.04 nb/sr and 3.08 ± 0.04 nb/sr, are both in agreement with the fit to the World data of 3.06 nb/sr.

D. Accuracy of the Reconstruction Matrix Elements

The agreement of the p(e,e′)p cross section with the World data from both the elastic scan and the extended target test indicates the validity of the solid angle

TABLE VIII. Cross Section for Elastic Scan and Extended Target Test

Momentum Offset (%)	Measured Yield† (pb)	$\Delta\Omega_{p(e,e')p}$ (msr)	RCOR	$d\sigma/d\Omega$ † nb/sr
2.763	10.72(08)	2.3491	0.76639	5.95(4)
1.238	12.02(15)	2.5664	0.76639	6.11(7)
1.224	11.80(12)	2.5625	0.76639	6.01(6)
-0.2649	12.33(12)	2.6105	0.76639	6.16(6)
$\approx$ 1.42	12.04(11)	2.6125	0.76639	6.01(5)
-3.2216	11.56(10)	2.5593	0.74622	6.05(5)
Target Length (cm)				
4.029	6.082(75)	2.5998	0.76347	3.06(4)
15.818	5.012(59)	2.2663	0.71791	3.08(4)

†Uncertaintes in parenthesis are statistical only.

calculation and data reconstruction procedure, averaged over the acceptance of the spectrometer. However, the agreement does not preclude errors in the data reconstruction that could, in principle, cancel, or nearly cancel, in the average over the spectrometer acceptance. An accurate measurement of the cross section for various bins in the acceptance is desirable, but is not possible because of the limited statistics of the p(e,e')p data. Nevertheless, the missing mass defined by Equation 4.10 is constrained in elastic scattering to reproduce the proton mass $W^2 = M_p^2 = 0.88035\,\mathrm{GeV}^2$, and can be measured precisely with a modest statistical sample of events, thereby providing a precise test of the reconstruction matrix elements. Furthermore, the data from the elastic scan can be used to isolate specific regions of the 8 GeV/c acceptance. The high precision is obtained by fitting the W^2 peak with a Gaussian, however, as is clear from Figure 22, the radiative tail must be taken into account. We follow a de-radiative procedure based on that of P.N Kirk *et al.* [50]. A differential radiative correction, with which the radiative tail is moved back into the peak on a bin-by-bin basis, is applied, so that the corrected data form a Gaussian peak centered on $W^2 = M_p^2$. The de-radiative procedure is explained, in detail, in Section IV D 1, and is then applied to the p(e,e')p data in Section IV D 2. Maximum uncertainties in the reconstructed three-momentum over the acceptance of the spectrometer are then estimated from systematic variations in the peak position across the acceptance of the spectrometer.

1. De-radiation of W^2

Equations 4.12– 4.14 can be combined to express the Born level cross section in terms of the measured W^2 histogram with an integral radiative correction:

$$\left(\frac{d\sigma}{d\Omega}\right)^{1-\gamma} = (\mathrm{RCOR}[W^2_{\mathrm{cut}} - M_p^2])^{-1} \int_{W^2_{\mathrm{SE}}}^{W^2_{\mathrm{cut}}} dW'^2 \left(\frac{d\sigma}{d\Omega dW'^2}\right)_{\mathrm{measured}} . \qquad (4.18)$$

TABLE IX. Summary of Radiative Correction Parameters

E (GeV)	θ_0	Target	P_1	P_2
2.015	40.723°	4CM_LH2	0.966963	0.09338953
2.015	40.723°	15CM_LH2	0.947039	0.1094746
1.9958	37.023°	4CM_LH2	0.967938	0.09227504

In the de-radiation procedure, the integral radiative correction is averaged over the first bin above the super-elastic cut, thereby correcting that bin for radiative losses. The yield added to the first bin is then removed from higher bins by averaging the difference of the radiative correction between the respective bins. With the first bin corrected, the procedure is repeated with the remaining bins. In order to simplify the integration involved in the averaging of the radiative correction, the Mo and Tsai calculation is fit with the following form:

$$\mathrm{RCOR}[\Delta(E, E'_{\mathrm{cut}}, \theta)] = P_1 \Delta^{P_2}, \tag{4.19}$$

$$\begin{aligned}\Delta(E, E'_{cut}, \theta) &\equiv W^2_{\mathrm{cut}}(E, E'_{cut}, \theta) - M^2_{\mathrm{p}}, \\ &= 2M_{\mathrm{p}}(E - E'_{\mathrm{cut}}) - 4EE_{\mathrm{cut}} \sin^2 \frac{\theta}{2}.\end{aligned}$$

The fit is not only convenient, but essentially exact (as shown in Figure 25) because the formulae of Mo and Tsai neglect the Q^2 dependence of the elastic cross section. Values of the fit parameters for various kinematics and targets are given in Table IX.

The de-radiation proceeds on a bin-by-bin basis as follows. The first bin is chosen just above the super-elastic cut. One starts here because this bin received no contribution from events that have radiated out of lower W^2 bins. In calculating the radiative correction to the first bin, one ignores the actual measured value of W^2 because of resolution. (The radiative correction is not defined for cutoffs below the M^2_{p}). One considers only the *difference* in initial and final values of W^2, with the

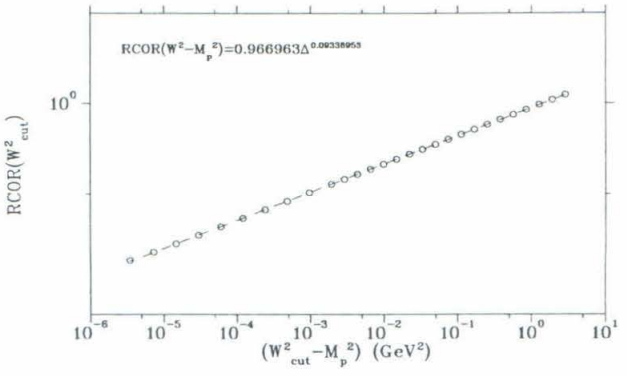

FIG. 25. Radiative Correction Parameterization

The figure shows the radiative correction calculated using the procedure of Section IV D 1 (open circles) and the two-parameter fit of Equation 4.19 (dashed line), justifying the use of the fit. The radiative correction was calculated for the kinematics of the measured data: $E = 2.015\,\mathrm{GeV}$, $\theta = 40.723^{\circ}$.

upper edge of the bin defining the cutoff. Thus the average radiative correction over the bin is defined:

$$R_1 = \frac{1}{\delta W^2_{\rm bin}} \int_0^{\delta W^2_{\rm bin}} d\omega' \mathrm{RCOR}[\omega'] \tag{4.20}$$

$$= \frac{P_1}{1+P_2} (\delta W^2_{\rm bin})^{P_2}. \tag{4.21}$$

Then the 1-photon yield of this first bin is given by:

$$\sigma_1^{1-\gamma} = \sigma_1^{\rm raw} / R_1. \tag{4.22}$$

Here $\sigma_1^{\rm raw}$ is the raw yield in the first bin, and $\delta W^2_{\rm bin}$ is the bin width. It must be emphasized that the radiative correction is not calculated with absolute values of W^2. One considers only the *difference*, Δ, between the radiated and unradiated values of W^2.

The yield that has been added to the first bin,

$$\delta\sigma_1 = \sigma_1^{\text{raw}} \cdot \left(\frac{1}{R_1} - 1\right), \tag{4.23}$$

must then be subtracted from the rest of the yield in higher bins. In calculating the yield that radiated from the 1st bin to the i^{th} bin, again we average over the difference in radiative correction: the correction to the i^{th} bin is given by:

$$\sigma_i' = \sigma_i - \delta\sigma_1 / R_i, \tag{4.24}$$

where the average difference in the radiative correction across the bin is

$$R_i = \frac{1}{\delta W_{\text{bin}}^2} \int_0^{\delta W_{\text{bin}}^2} d\omega' \left(\text{RCOR}[(i+1)\delta W_{\text{bin}}^2 + \omega'] - \text{RCOR}[(i-1)\delta W_{\text{bin}}^2 + \omega']\right) \tag{4.25}$$

$$= \frac{P_1}{1+P_2} \cdot \left((i+2)^{1+P_2} - (i+1)^{1+P_2} - (i)^{1+P_2} + (i-1)^{1+P_2}\right) (\Delta W_{\text{bin}}^2)^{P_2}. \tag{4.26}$$

After going through all bins ($i = 2, ..., i_{\max}$) the 1st bin is radiatively corrected, and each higher bin has the contribution from only the 1st bin removed. The procedure is repeated with the 2nd, then 3rd bin, up to the n^{th} bin. The procedure can be summarized with the matrix equation

$$\begin{pmatrix} \sigma_1^{1-\gamma} \\ \sigma_2^{1-\gamma} \\ \sigma_3^{1-\gamma} \\ \vdots \\ \sigma_n^{1-\gamma} \end{pmatrix} = \begin{pmatrix} a_1 & 0 & 0 & \dots & 0 \\ a_2 & a_1 & 0 & \dots & 0 \\ a_3 & a_2 & a_1 & \dots & 0 \\ \vdots & \vdots & \vdots & \ddots & \vdots \\ a_n & a_{n-1} & a_{n-2} & \dots & a_1 \end{pmatrix} \begin{pmatrix} \sigma_1^{\text{raw}} \\ \sigma_2^{\text{raw}} \\ \sigma_3^{\text{raw}} \\ \vdots \\ \sigma_n^{\text{raw}} \end{pmatrix}, \tag{4.27}$$

where:

$$a_1 = \frac{1}{R_1}$$

$$a_n = -a_1 \sum_{i=2}^{n} R_i a_{n-i+1}. \tag{4.28}$$

Equations 4.27 provides a simple method to calculate a de-radiated spectrum. In addition, the uncertainty squared $(\delta\sigma_i^{1-\gamma})^2$ in each bin can be computed in terms of the

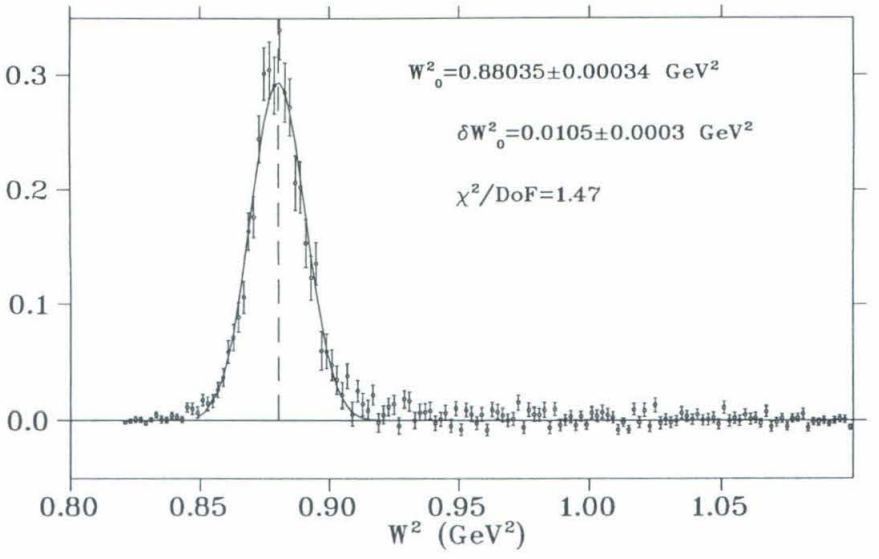

FIG. 26. De-radiated W^2 Histogram

The figure shows the p(e,e')p data from Figure 22 after the de-radiative procedure is applied. The solid line is the Gaussian fit.

squared uncertainties in the raw yields $(\delta\sigma_j^{\rm raw})^2$ weighted by corresponding squares of the de-radiating matrix $(a_{i-j+1})^2$. A typical de-radiated spectrum is shown in Figure 26.

2. Kinematic Calibration Results

The de-radiation procedure described previously was applied to p(e,e')p data composing the elastic scan as a precise test of the reconstruction matrix elements used in the data analysis. The de-radiated missing mass spectra were fit with a 3 parameter Gaussian shape, yielding a normalization A_0, peak position W_0^2 and peak width $\sigma_{W_0^2}$, along with their uncertainties. The runs in the elastic scan illuminate different regions of the 8 GeV/c acceptance, and the observed variation in W_0^2 allows a precise test of the reconstruction of $|\mathbf{p_f}|$ across the acceptance of the detector. The elastic

TABLE X. Mean W^2 in Momentum Scan

P_0 (GeV)	Momentum Offset (%)	W_0^2 (GeV^2)
1.3582	2.763	0.8712(3)
1.3795	1.238	0.8750(4)
1.3797	1.224	0.8747(3)
1.4005	-0.2649	0.8760(2)
1.4418	-3.2216	0.8740(2)

TABLE XI. Mean W^2 Versus Angle

θ_f	$\delta\theta$ cut	W_0^2 (GeV^2)
$< 40.08^\circ$	$\delta\theta \leq -10\,\mathrm{mr}$	0.8749(2)
40.65°	$\|\delta\theta\| < 10\,\mathrm{mr}$	0.8737(2)
$> 41.23^\circ$	$\delta\theta \geq +10\,\mathrm{mr}$	0.8740(3)

peak is also fit in three regions of the angular acceptance: $\delta\theta < 10\,\mathrm{mr}$, $|\delta\theta \leq 10\,\mathrm{mr}$ and $\delta\theta > 10\,\mathrm{mr}$.

The results are show in Table X. The data do not cluster around $W_0^2 = M_\mathrm{p}^2$ because no offsets were used in the analysis. (The data were taken during the running of E140x and the offsets fit with NE 18 data [35] are not applicable because the detector hut was removed between experiments). Run 279 is not included because of problems with the recorded bending-magnet NMR render it useless for such a precise test.

Variations in W_0^2 can be related to errors in the measured target quantities $\Delta P/P_0$ and $\Delta\theta$ by use of the relations:

$$dW^2 = \frac{\partial W^2}{\partial E}dE + \frac{\partial W^2}{\partial E'}dE' + \frac{\partial W^2}{\partial \theta}d\theta,$$

$$\begin{aligned}
\frac{\partial W^2}{\partial E} &= 2M_{\rm p} - 4E'\sin^2\theta/2 \;=\; 1.31\,{\rm GeV} \\
\frac{\partial W^2}{\partial E'} &= -2M_{\rm p} - 4E\sin^2\theta/2 \;=\; 2.68\,{\rm GeV} \\
\frac{\partial W^2}{\partial \theta} &= -4EE'\sin\theta/2\cos\theta/2 \;=\; -3.36\,{\rm GeV}^2/{\rm rad}.
\end{aligned} \tag{4.29}$$

For the elastic scan, the largest deviation of W_0^2 occurs at the most positive momentum offset (2.7%). (That is, at $\delta\theta = 0$ the elastic peak is expected be at $\Delta P/P_0 = 2.7\%$). For all NE 17 kinematics and spectrometer settings, this region of the acceptance is not illuminated by the ^{2}H(γ,p)n reaction, and this deviation can be ignored. For the other runs in the scan, the variation of the measured peak position $\Delta W_0^2 \approx 0.0020(4)\,{\rm GeV}^2$. Using Equation 4.30 with $dE = 0$ and $d\theta = 0$ gives:

$$\delta E' = \Delta W_0^2 \left(\partial W_0^2/\partial E'\right)^{-1} \;=\; 0.75\,{\rm MeV}, \tag{4.30}$$

so that the error in $\Delta P/P_0$ is:

$$\delta\frac{\Delta P}{P_0} = \delta E'/P_0 = 0.06\%. \tag{4.31}$$

Thus the uncertainty in the momentum over the useful region of the acceptance is 0.06% of the central momentum.

Similarly, the missing mass peak position is measured in three $\delta\theta$ regions covering roughly 10 mr each. The variation in peak positions is $1.2\times10^{-3}\,{\rm GeV}^2$. Using Equation 4.30 with $dE = 0$ and $dE' = 0$ we obtain a maximum systematic uncertainty in the measured angle:

$$\delta\left(\theta_f\right) = \Delta W_0^2 \left(\partial W_0^2/\partial\theta\right)^{-1} \;=\; 0.36\,{\rm mr}. \tag{4.32}$$

The uncertainties derived above are correlated because of the kinematics correlation Equation 4.6, so that the $\Delta P/P_0 = 0.06\%$ and $\delta\theta = 0.36$ mr uncertainties near the edge of the acceptance are upper limits. The actual error is most likely some combination of a distortion in $\delta P/P_0$ and $\delta\theta$, with magnitudes each less than the

upper limit. Note also that the small variations of W_0^2 with respect to $\Delta P/P_0$ and $\delta\theta$ are quadratic, indicating that the magnification and dispersion are modeled correctly to first-order.

3. Spectrometer Resolution

The width of the elastic peak $\sigma_{W^2} = (1.08 \pm 0.03) \times 10^{-2}\,\mathrm{GeV}^2$ extracted from the de-radiated spectrum has contributions from the measured momentum σ_P and angle $\sigma_{\delta\theta}$, and also the beam energy σ_E. Using Equation 4.30 with the kinematics of the 15 cm target run:

$$\sigma_{W^2}^2 = \frac{\partial W^2}{\partial E}^2 \sigma_E^2 + \frac{\partial W^2}{\partial E'}^2 \sigma_P^2 + \frac{\partial W^2}{\partial \theta}^2 \sigma_{\delta\theta}^2 \tag{4.33}$$

$$= (1.45\,\mathrm{GeV})^2 \sigma_E^2 + (2.84\,\mathrm{GeV})^2 \sigma_P^2 + (3.47\,\mathrm{GeV}^2/\mathrm{r})^2 \sigma_{\delta\theta}^2. \tag{4.34}$$

The data were taken with the energy slits at 0.2% FW ($\Delta E = 0.004\,\mathrm{GeV}$, $\sigma_E = \Delta E/2\sqrt{2\log 2} = 0.0017\,\mathrm{GeV}$), so that the width due to the beam energy is $0.0021\,\mathrm{GeV}^2$. The spectrometer's momentum and angle resolutions, which are dominated by multiple scattering and the wire chamber resolution, were calculated with the Monte Carlo at $\sigma_P \approx 0.20\% \times P_0$ and $\sigma_{\delta\theta} \approx 2.0\,\mathrm{mr}$, respectively. Using Equation 4.33, the resolution is then expected to be $\sigma_{W^2} \approx 1.3 \times 10^{-2}\,\mathrm{GeV}^2$, which is in reasonable agreement with the measured value. Similarly, the resolution in reconstructing E_γ, which is dominated by σ_P, can be calculated using Equation 5.1, and varies from 7–16 MeV at various kinematics for $^2\mathrm{H}(\gamma,\mathrm{p})\mathrm{n}$.

E. 8 GeV/c Solid Angle

The Transport model and Monte Carlo were used to determine the effective solid angle of the spectrometer. The solid angle for the detection of photoprotons from the ^{2}H(γ,p)n reaction is defined as:

$$\Delta\Omega_{d(\gamma,p)n} = (\Delta\theta\Delta\phi) \times N_{final}/N_{initial}, \tag{4.35}$$

where $\Delta\theta\Delta\phi$ are the angular cuts applied to the data ($\pm$15 mr $\times$ $\pm$ 50 mr). $N_{initial}$ is the number of trial events generated within the applied cut, including a cut on the reconstructed photon energy, and N_{final} is the number of events reconstructed within the cuts after propagation through the Monte Carlo.

The effective solid angle is thus calculated as an average over both the target length and the momentum bite of the spectrometer. To weight the average properly, the initial coordinates of the event are chosen realistically. The selection of the initial target position has been described in Section IV B. The three-momentum distribution of the trial events is approximately that of the data: Ignoring the production-angle variation of the cross section, both $\delta\theta$ and ϕ are chosen uniformly. Then, based on the expected s^{-11} variation of the invariant cross section, an initial photon energy is randomly selected according to the product of the bremsstrahlung cross section [51] and s^{-10} ($s = M_d^2 + 2M_d E_\gamma$). With the initial photon energy E_γ and the proton angle determined, the momentum ($\Delta P/P_0$) is given by inverting Equation 5.1 describing two-body kinematics. The Monte Carlo was run for each of the twelve kinematic settings of the experiment. The average solid angles are shown in Table XII. The solid angle shows strong dependence on the spectrometer angle, attributable to the limited acceptance at large Y_{trans}.

TABLE XII. Calculated Solid Angles

θ_0	P_8	E_γ range[†]	$\Delta\Omega$
	GeV/c	MeV	msr
52.999°	1.5050	1474–1574	2.101
30.958°	1.8704	1506–1575	2.397
21.183°	2.0050	1514–1574	2.536
53.000°	1.6937	1882–1900	2.187
29.065°	2.2233	1924–1990	2.491
19.847°	2.3957	1934–1990	2.613
51.340°	1.8926	2269.5–2377.5	2.216
27.609°	2.5453	2311.5–2377.5	2.520
18.835°	2.7523	2313.5–2377.5	2.637
49.170°	2.1088	2669–2777	2.248
17.920°	3.1171	2721–2777	2.656
15.528°	4.4007	4136–4190	2.664

[†]The $\Delta P/P_0$ cut varies with $\delta\theta$, and can be determined from the E_γ cuts and the spectrometer setting.

F. Nuclear Interactions of Protons

Photoprotons are produced in the target and can undergo nuclear interactions in target and detector materials before passing through all three of the scintillator planes in the trigger, thereby going undetected. The amount of proton-absorption is estimated and is in agreement with that measured using the p(e,e'p) reaction.

1. Calculation of Nuclear Absorption

Photoprotons have both elastic and inelastic collisions with nuclei. After an inelastic reaction it is assumed that the photoproton is lost, and cannot be detected. The elastic cross-section is forward peaked so that not all photoprotons undergoing elastic nuclear collisions fail to trigger the spectrometer. The two extremes are estimated from the mean free path between collisions (λ_C) and inelastic interactions (λ_I) taken from [5]. The photoproton absorption is given by

$$\mathsf{A} = 1 - e^{t/\lambda}, \tag{4.36}$$

where t is the thickness of the absorbing material. Mean free paths and absorptivities of material traversed by the photoprotons are given in Table XIII. The amount of liquid deuterium traversed depends on the production angle of the proton, and varies from 3.0 cm at $\theta_{\rm lab} = 53^\circ$ to 6.8 cm at $\theta_{\rm lab} = 15^\circ$. (Thus the angle-dependent correction due only to the LD_2 varies from $\approx$ 1.0% to 2.3%). At spectrometer momenta above 3 GeV/c the Čerenkov detector was filled with Freon-114 at 760 torr, thus introducing an additional absorption of $\approx$ 2.3%. The data at $E_{\rm beam} = 1.6$ GeV were taken immediately following the $E_{\rm beam} = 4.2$ GeV data, and the Čerenkov counter did not have time to be entirely evacuated. The pressure was monitored during the run and the absorption correction has been scaled accordingly.

TABLE XIII. Estimated Absorption of Photoprotons in Various Elements of the Target and Detector

Absorber	Material	ρ (g/cm^3)	λ_I (g/cm^2)	λ_C (g/cm^2)	length (cm)	thckness (g/cm^2)	A_I (%)	A_C (%)
target cell wall and window and spectrometer window	Al	2.7	106.4	70.6	0.08	0.22	0.21	0.31
Čerenkov entrance and exit	Al	2.7	106.4	70.6	0.08	0.22	0.21	0.31
Čerenkov mirror	Lucite	1.2	83.6	59.2	0.64	0.77	0.92	1.29
$C_2Cl_2F_4$ Čerenkov gas		4.9×10^{-3}	106	70.6	400	2.0	1.87	2.79
Wire Chambers	Fe	7.9	131.9	82.8	0.26	0.21	0.16	0.25
SF scintillators	Polystyrene	1.0	82.0	58.4	1.0	1.0	1.21	1.70
NBS scintillators	Polystyrene	1.0	82.0	58.4	1.28	1.3	1.57	2.20
SM scintillators	Polystyrene	1.0	82.0	58.4	1.3	1.3	1.57	2.20
Air	80% N_2, 20%O_2	$1.3 \cdot 10^{-3}$	90.0	62.0	400	0.52	0.58	0.84
Liquid Deuterium	^{2}H	0.0710	54.7	45.7	4.66[†]	0.33	0.60	0.72
Total							8.57	12.0

[†]The amount of LD_2 depends on the scattering angle.

2. Measurement of Nuclear Absorption

During the NE 17 run, the two SLAC spectrometers—the 1.6 GeV/c and 8 GeV/c—were configured for the NE 18 experiment [35] to detect electrons and protons arising from (e,e'p) reactions in coincidence. Thus, we were able to measure absorption of protons in the 8 GeV/c directly by comparing inclusive *ep* scattering rates to exclusive *ep* rates. Details of the coincidence detection and the 1.6 GeV/c spectrometer are described in [35]; an outline of the comparison is presented here.

The inclusive and exclusive cross sections are measured simultaneously as follows. The 1.6 GeV/c is set to detect electrons elastically scattered from protons, while the 8 GeV/c is set to detect the recoiling protons. Data for both spectrometers are written to tape whenever a 1.6 GeV/c trigger occurs. For each inclusive p(e,e')p event detected in the 1.6 GeV/c, it is determined whether or not the recoiling proton

TABLE XIV. Measured Absorption of Photoprotons

E_{beam}	1.6 GeV/c Setting	8 GeV/c Setting	Proton Efficiency[†]
2.015 GeV	-1.400 GeV/c, 37.8°	+1.237 GeV/c, 43.29°	91.5±0.6
3.186 GeV	-1.470 GeV/c, 48.99°	+2.483 GeV/c, 26.53°	92.4±1.1
4.212 GeV	-1.470 GeV/c, 54.24°	+3.559 GeV/c, 19.58°	89.8±3.9
5.122 GeV	-1.470 GeV/c, 56.98°	+4.485 GeV/c, 15.92°	88.4±4.5

[†]The increased absorption above $P_8 = 3\,\text{GeV/c}$ is from the gas in the Čerenkov detector.

was detected in the 8 GeV/c spectrometer. Thus, the proton detection efficiency is calculated as:

$$\epsilon_8 = N_{p(e,e'p)}/N_{p(e,e')p} \approx 1 - \mathsf{A}. \tag{4.37}$$

The efficiencies ϵ_8 contains contributions from the trigger, tracking and timing efficiency, which are estimated at 99% total, so the dominant mode of proton loss is nuclear absorption. Note that the measurement is independent of the 1.6 GeV/c spectrometer efficiency. The measurement was performed at four beam energies; the results are summarized in Table XIV, and agree well with the expected absorption.

G. Summary

In this chapter, the procedure for handling the 8 GeV/c spectrometer large-acceptance tune has been discussed. The difficulties with the understanding of the large-acceptance tune arise primarily because of the increased sensitivity of the optics to the details of the quadrupole field shapes and strengths. In the normal tune, the sensitivity is much less, and the measured values of $\int \mathbf{B} \cdot d\mathbf{l}$ are adequate for a description of the optics at the 1% level [43]. In the absence of detailed field maps of the quadrupoles, an understanding of the large-acceptance tune at the 1% level may not

be possible. In summary, the procedure described here is as follows. Events are reconstructed with matrix elements determined from kinematic constraints in coincidence measurements on p(e,e'p) [35], with the recoiling proton detected in the 8 GeV/c spectrometer. Inclusive cross sections are formed by division of the measured rate with a solid angle that is calculated with a Monte Carlo model of the spectrometer. The Monte Carlo model uses a second-order Transport deck to approximate the spectrometer optics. The procedure has several advantages. The Transport deck is optimized to reproduce the observed focal plane distributions in p(e,e')p and p(e,e'p) measurements. Thus the various apertures and magnifications that determine the solid angle are well reproduced. Because the trial events are reconstructed with the best-fit reverse matrix elements of the Transport deck, so that the model is self-consistent, the calculated value of $\Delta\Omega$ is not sensitive to the unknown details of the quadrupoles. The data are reconstructed with a consistent set of matrix elements, although they are different from best-fit matrix elements of the Transport deck. Nonetheless, the accuracy of the reconstructed target momentum is maximized, and using the de-radiated W^2 peak, the systematic error in the reconstruction is estimated. Furthermore, the use of an acceptance function is abandoned; all the measured counts in a run are weighted equally, thereby avoiding large systematic errors in the weighting that would result from discrepancies in the model. Finally, the procedure is applied to the well known p(e,e')p reaction, reproducing the theoretical cross sections to within 1–2%.

V. MEASUREMENT OF THE PHOTODISINTEGRATION CROSS SECTION

In this section, the final steps in the extraction of the ^{2}H(γ,p)n cross section are presented, followed by a discussion of possible systematic problems with the experimental procedure, focussing on problems that could arise from the presence of the 6% RL radiator upstream of the target and detector—multiple scattering of the electron beam and high accidental background rates, in particular. A measurement of the electrodisintegration cross section is presented as a check of the photodisintegration cross section, with favorable results. Finally, the systematic errors on the measured ^{2}H(γ,p)n cross sections are discussed.

A. The ^{2}H(γ,p)n Cross Section

Measurement of the ^{2}H(γ,p)n cross section requires an accurate determination of the initial photon flux and the final photoproton yield. The bremsstrahlung spectral shape and end-point energy must be determined, as well as the integrated flux. Background in the photoproton distribution must be measured and subtracted too. The primary background is from Al(γ,p)X and Al(γ,d)X reactions in the target end-caps, along with reactions from virtual photons and real bremsstrahlung produced in the target. All these processes can be measured and subtracted directly; at the forward points at high energy, however, there is significant rate from accidental events that do not come from the target, and a correction must be applied.

The detection of photoprotons with only the highest possible energies ensures that the final state of the photodisintegration was a proton and a neutron. With the assumed two body kinematics the initial photon energy, E_γ, can be determined from the detected proton's three-momentum:

$$E_\gamma = \frac{E_p M_d - \frac{1}{2}(M_d^2 + m_p^2 - m_n^2)}{M_d - E_p + P_p \cos\theta_p}. \tag{5.1}$$

The quantity $E_\gamma - E_0$ is histogrammed (E_0=beam energy), implicitly averaging over the spectrometer's angular acceptance, and then compared to the calculated bremsstrahlung spectrum, thereby yielding the energy dependence of the ^{2}H(γ,p)n reaction directly.

The bremsstrahlung spectrum is calculated using the procedure of Mathews and Owens [51]. The formula applies to an uncollimated photon beam produced by a radiator near the photonuclear target, and yields an integrated-over-angle cross section. The electron-nuclear bremsstrahlung cross section is calculated in the standard Bethe-Heitler theory in the extreme-relativistic limit, modified to include intermediate screening effects and a Coulomb correction. The method is valid for photon energies below the tip ($E_0 - m_e - k_{tip} \approx 0.02\,\mathrm{MeV} \cdot Z = 0.6\,\mathrm{MeV}$). A similar, but less accurate, procedure is followed in evaluating the electron-electron bremsstrahlung cross section, which produces roughly $1/(1+Z) = 3.3\%$ of the total yield in the top 100 MeV of the spectrum. The evaluation of the actual photon flux includes the energy-spread of the beam, radiative energy loss and photon absorption in the radiator. These effects introduce a 3% uncertainty in flux below the tip region. A detailed description of the procedure is given in the Appendix.

Known background process are measured and subtracted by taking data with nearly identical hydrogen and deuterium targets with both the radiator in and out. Data taken from the hydrogen target yield events only from the aluminium end-caps (Al(γ,p)X and Al(γ,d)X), and can be subtracted from the yield measured with the deuterium target. The liquid hydrogen provides an equivalent amount of radiation lengths as the liquid deuterium, while photoprotons from it are kinematically forbidden. The procedure is then repeated with the radiator out, measuring the yield from virtual processes and real bremsstrahlung photons produced in the target. Before

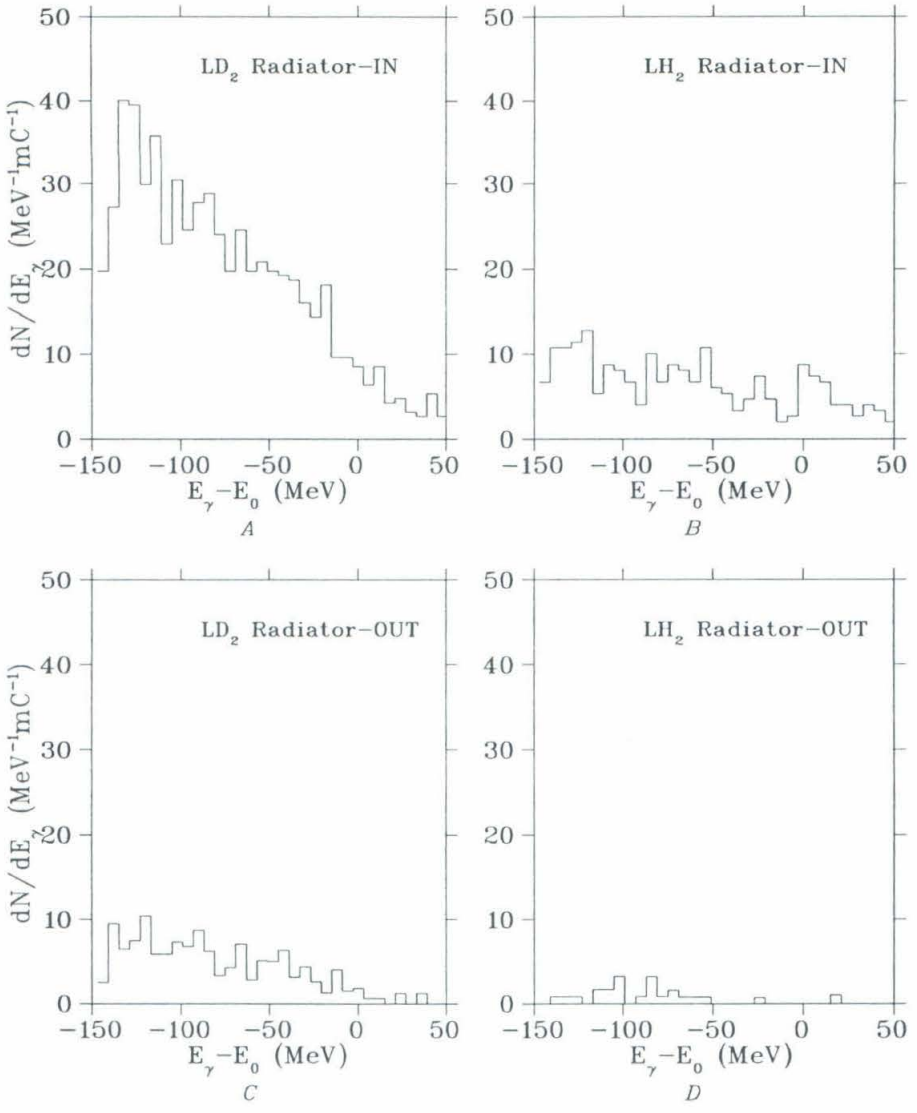

FIG. 27. $E_\gamma - E_0$ Histograms

The Figures A–D show the normalized photoproton yields, histogrammed according to Equation 5.1, taken in the LD_2^{IN}, LH_2^{IN}, LD_2^{OUT} and LH_2^{OUT} configurations, respectively.

the radiator out data is subtracted though, an energy dependent correction, $f(E_\gamma)$, accounting for radiative straggling of the electron beam in the radiator is applied. Thus, the distribution of photoprotons from the ^{2}H(γ,p)n reaction is given:

$$\frac{dN_{d(\gamma,p)n}}{dE_\gamma} = \left[\frac{dN^{in}_{LD2}}{dE_\gamma} - \frac{dN^{in}_{LH2}}{dE_\gamma}\right] - f(E_\gamma)\cdot\left[\frac{dN^{out}_{LD2}}{dE_\gamma} - \frac{dN^{out}_{LH2}}{dE_\gamma}\right], \tag{5.2}$$

where the distributions, $\frac{dN_i}{dE_\gamma}$, are the proton rates normalized by the product of the incident number of electrons on target and the areal density of nuclei in the target. Explicitly,

$$\frac{dN_i}{dE_\gamma} = \frac{e}{Q_{eff}}\frac{1}{n_{nucl}}\frac{N_{E_\gamma}}{\delta E_{\gamma,\mathrm{bin}}}\frac{1}{\epsilon}, \tag{5.3}$$

where e is the electron charge, Q_{eff} is the dead-time corrected integrated beam current, n_{nucl} is the target density (nuclei/nb), ϵ is the product of all the efficiency corrections discussed in Section III, N_{E_γ} is the raw histogram (counts/bin) and $\delta E_{\gamma,\mathrm{bin}}$ is the bin width in MeV.

The correction factor $f(E_\gamma)$ arises because the spectrum of bremsstrahlung photons produced in the photonuclear target without the radiator is different from that with the radiator present. The primary electron beam radiates energy as it passes through the radiator, so that the spectrum of electron energies impinging on the target and subsequently producing photons (real or virtual) is dependent on the radiator thickness. The correction factor is defined as the ratio of the two photon spectra:

$$f(E_\gamma) = \frac{dN^{IN}_{\gamma,target}}{dE_\gamma} \Big/ \frac{dN^{OUT}_{\gamma,target}}{dE_\gamma}. \tag{5.4}$$

The photon flux produced in the target with the radiator out is calculated simply as:

$$\frac{dN^{OUT}_{\gamma,target}}{dE_\gamma} = N_0 \int dE' \delta(E_0 - E') \left[\frac{d\sigma_{brem}}{dE_\gamma}(E', E_\gamma) + \frac{d\sigma^{eff}_{virtual}}{dE_\gamma}(E', E_\gamma)\right]. \tag{5.5}$$

$$= N_0 \left[\frac{d\sigma_{brem}}{dE_\gamma}(E_0, E_\gamma) + \frac{d\sigma^{eff}_{virtual}}{dE_\gamma}(E_0, E_\gamma)\right], \tag{5.6}$$

where $\frac{d\sigma_{brem}}{dE_\gamma}(E', E_\gamma)$ is the cross section for the production of a photon of energy E_γ by an electron of energy E' in the target materials (deuterium and aluminium), and N_0 is an overall normalization. $\frac{d\sigma^{eff}_{virtual}}{dE_\gamma}(E', E_\gamma)$ is the effective virtual photon spectrum given by Wright and Tiator [52], and is discussed in further detail in Section V H. The delta function approximates the primary electron beam energy distribution as a spike at E_0. The radiator-in photon spectrum is obtained by replacing the delta function with the electron energy distribution after passing through the radiator, $I(E_0, E', Z, t_{rad})$. The form of $I(E_0, E', Z, t_{rad})$ if discussed in the Appendix.

Thus, the bremsstrahlung flux from the target can be written:

$$\frac{dN^{IN}_{\gamma,target}}{dE_\gamma} = N_0 \int dE' I(E_0, E', Z, t_{rad}) \left[\frac{d\sigma_{brem}}{dE_\gamma}(E', E_\gamma) + \frac{d\sigma^{eff}_{virtual}}{dE_\gamma}(E', E_\gamma) \right]. \quad (5.7)$$

Figure 28 shows $f(E_\gamma)$ for a beam energy of 2.0 GeV. In the analysis, the ratio $f(E_\gamma)$ is calculated on an event by event basis, so that the correction can be applied to histograms in variables other than the reconstructed photon energy. Several approximations have been made in the calculation of the photon flux from the target that are not made in calculation of the yield from the radiator. Both the finite energy spread of the electron beam and radiative straggling in the target are ignored (the target is treated as a *thin* radiator). Inclusion of these effects into Equation 5.4 did not have a significant effect on the ratio $f(E_\gamma)$; they did, however, preclude an event-by-event calculation of $f(E_\gamma)$ because of the excessive CPU-time required to evaluate the resulting integrals reliably. (For a discussion of these effects in detail, see the Appendix on the *thick* radiator bremsstrahlung yield).

B. End-Point Fitting

The photoproton yield is calculated according to Equation 5.2, and histogrammed according to Equation 5.1. In the approximation that the angular dependence of

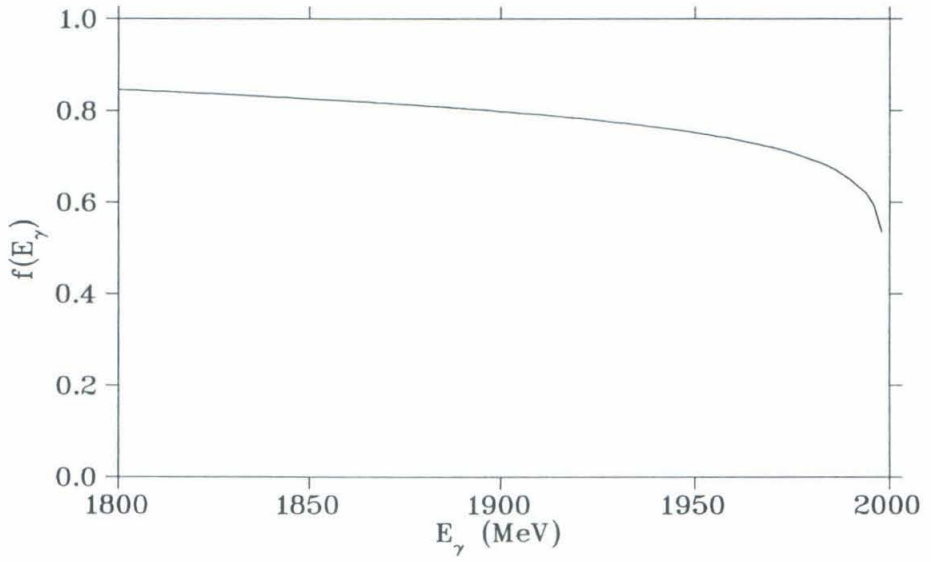

FIG. 28. The Radiator-out Correction

The figure shows the correction factor $f(E_\gamma)$, which is applied to the photoproton spectra that are measured with the radiator absent, accounting for the straggling of the electron beam in the radiator. The calculation is for a beam energy of 2 GeV.

the photodisintegration cross section, $\frac{d\sigma}{d\Omega}(E_\gamma)$ is small over the acceptance of the spectrometer, and that the energy dependence varies as s^{-10}, the photoproton yield can be written:

$$\frac{dN_{d(\gamma,p)n}}{dE_\gamma} = C_1 \times \frac{d\sigma}{d\Omega}(E_\gamma - C_2) \cdot s(E_\gamma - C_2)^{-10}. \tag{5.8}$$

The two parameters C_1 and C_2 represent an overall normalization and an offset in the momentum calibration of the spectrometer, respectively. Smearing the right side of Equation 5.8 with a Gaussian resolution function, a two parameter minimum χ^2 fit was done by varying C_1 and C_2. (The smearing resolution is determined from the known momentum and angle resolutions discussed in Section IV D 3 combined in quadrature with weights determined by Equation 4.30). Because of poor statistics, the end-point parameter C_2 is not well constrained, and little can be learned about the absolute momentum calibration of the 8 GeV/c.

C. Pion Background

At all the spectrometer momentum settings listed in Table XII, pions have a velocity very close to c ($\beta > 0.995$), so that at momentum settings below ≈ 2.5 GeV/c time-of-flight separation is possible, while above 2.7 GeV/c the Čerenkov detector can be used as a veto. No pion time-of-flight signal is seen at momenta below 2.5 GeV/c. At momenta above the Čerenkov threshold, events are seen with Čerenkov signals above the 1-photo electron (scintillation) cut that have ToF's cluster about $\beta = 1$; however, these events do not, in general, reconstruct to the target and are a small part of the accidental background discussed in Section V G. No Čerenkov veto is applied to avoid inefficiency in the detection of protons due to knock-on electrons [40].

D. Two-Step Background

The two-step background is produced by the ^{2}H(γ,π)X reaction followed by pion absorption ^{2}H(π,p)X or pion scattering ^{2}H(π,p)πN. Using the procedure developed in [36], described below, the two-step background is either kinematically forbidden or expected to be negligible at all kinematics run in this experiment.

1. Pion Photoproduction

Following [36], the only significant contribution to the ^{2}H(γ,π)X reaction is pion photoproduction, specifically quasi-free p(γ, π^+)n. The spectrum of final state pions is calculated in the impulse approximation by a Monte Carlo method as follows: The initial proton momentum distribution is calculated from the deuteron wave function of [53], and then folded with the known photon spectrum, which is boosted into the proton rest frame. The final state pion is then selected using the measured p(γ, π^+)n differential cross section from [54], and finally boosted back into the deuteron rest frame (*i.e.*, the lab frame). The resulting distribution of π^+ momenta is stored and used as an input to the second step of the calculation, which is also evaluated by a Monte Carlo method. The two reactions considered in the second step are pion absorption and pion-nucleon scattering:

$$\pi^+ d \rightarrow pp \text{ and} \tag{5.9}$$

$$\pi^+ d \rightarrow p(\pi N), \text{ respectively.} \tag{5.10}$$

2. Pion Absorption

The differential cross section for $pp \rightarrow \pi^+ d$, the inverse of (5.9), has been compiled as functions of Legendre polynomials [55]. The cross section for (5.9) can then be

calculated using the principle of detailed balance, which relates the two reactions in terms of the spins of the particles involved:

$$\frac{\sigma_{pp\to\pi^+d}}{\sigma_{\pi^+d\to pp}} = 2\frac{(2s_\pi+1)(s_d+1)}{(2s_p+1)^2}\frac{p_\pi^2}{p_p^2}. \tag{5.11}$$

The distribution of background protons in the lab can then be calculated by combining the pion spectrum calculated in Section V D 1 with the d(π,p)p cross section calculated from Equation 5.11 and [55].

3. Pion-Nucleon Scattering

The pion nucleon scattering cross section in the pion-proton center-of-mass system is calculated from measured phase shifts [56]. The background from quasi-elastic p(π,p)π scattering from the deuteron is calculated using the proton momentum distribution described in Section V D 1 folded with the CMS π-N cross section. The outgoing proton is then boosted into the lab frame.

4. Two-Step Background, Summary

The two-step process is not expected to yield significant background at any of the kinematics studied in this experiment. The expected signature is rate in the photoproton histogram (Equation 5.2) at $E_\gamma > E_0$, and none is seen. Only forward center-of-mass angles, $\theta^* \leq 90^\circ$, were studied; in the few GeV region, the kinematics of two-body photodisintegration at forward angles require the photoproton momentum to be near or greater than initial photon momentum, so that only the high momentum tails of the deuteron wave function contribute, and the phase space for the two-step processes, if there is any, is small. At backward angles the photoproton momentum is smaller and the two-step process can be significant. The NE 8 experiment studied photodisintegration at $E_\gamma = 1.6$ GeV and $\theta^* = 143^\circ$, and the two-step background was

25–30% of the d(γ,p)n rate. The calculation outlined above reproduced the measured two-step rate within 5%, and indicated that it is mostly from the pion absorption process [36].

E. Determination of Cross Section

The yield Y from the ^{2}H(γ,p)n reaction is calculated by summing the luminosity normalized photoproton distribution of Equation 5.2. To ensure that the photoprotons are produced only by the two-body process, only the top $\approx$ 100 MeV of the spectrum is used. (The actual cut depend on kinematics; for $\theta^* = 90^\circ$ the d(γ,p)nπ^0 threshold is $\approx$130 MeV below the beam energy, but at the forward angles the 100 MeV bite includes three-body rate. The cuts used are listed in Table XXIII, in the Appendix). Because of the rapidly changing shape of the bremsstrahlung spectrum near the tip, the sum is cut off at $E_\gamma - E_0 = -24.5$ MeV to avoid uncertainties in the photon yield caused by uncertainties in the location of the end-point. The photodisintegration cross section is then given in the laboratory system (i.e., with the deuteron at rest):

$$\frac{d\sigma}{d\Omega} = \frac{Y}{N_\gamma \Delta\Omega \mathsf{A}}, \tag{5.12}$$

where $\Delta\Omega$ is the average solid angle and A corrects for the absorption of photoprotons. N_γ is the number of photons produced by the radiator per incident electron in the energy range.

Because the photodisintegration cross section $\frac{d\sigma}{d\Omega}(E_\gamma)$ is a strong function of photon energy E_γ, and is not linear over the useful photon energy range $\Delta E_\gamma = E_\gamma^{\rm low} - E_\gamma^{\rm high}$, the average energy of photons impinging on the target, given by

$$\bar{E}_\gamma = \frac{\int E'_\gamma \frac{dN_\gamma}{dE'_\gamma} dE'_\gamma}{\int \frac{dN_\gamma}{dE'_\gamma} dE'_\gamma}, \tag{5.13}$$

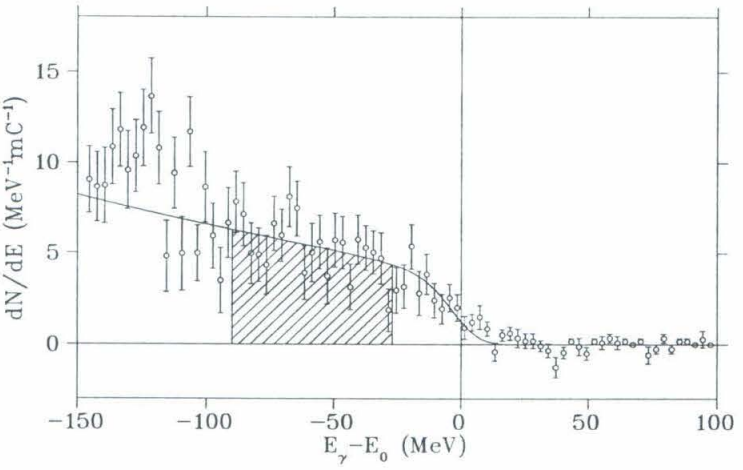

FIG. 29. $E_\gamma - E_0$ Histogram

The figure shows $^2H(\gamma,p)X$ photoproton rate, calculated according Equations 5.2. The solid line is the bremsstrahlung spectrum weighted by s^{-10} and smeared with a Gaussian resolution, as described in Section V B. The shaded region is the bremsstrahlung region used to isolate the two-body yield. Below ≈ -100 MeV, there is contamination from $^2H(\gamma,p)N\pi$.

where the integrals extend over ΔE_γ, does not properly normalize the measured cross section. In fact, the energy E_γ^{norm} at which the cross section is properly normalized must satisfy the relation

$$\frac{d\sigma}{d\Omega}\left(E_\gamma^{norm}\right) = \frac{\int \frac{dN_\gamma}{dE'_\gamma}\frac{d\sigma}{d\Omega}\left(E'_\gamma\right) dE'_\gamma}{\int \frac{dN_\gamma}{dE'_\gamma} dE'_\gamma}. \tag{5.14}$$

Explicitly, the L.H.S of Equation 5.14 represents the average cross section measured by the experimental procedure, while the R.H.S represents the actual energy dependent cross section. Clearly, Equation 5.14 cannot be solved for E_γ^{norm} without explicit knowledge of the energy dependence of $\frac{d\sigma}{d\Omega}(E_\gamma)$. Assuming $\frac{d\sigma}{d\Omega}(E_\gamma) \sim s^{-10}$, the L.H.S of Equation 5.14 is evaluated numerically, the equation is then inverted, yielding E_γ^{norm}. The energies obtained from Equation 5.14 are only slightly smaller ($\approx 0.5\,\mathrm{MeV}$) than those given by Equation 5.13. In this thesis Equation 5.13, the conventional choice, is used to evaluate the mean photon energy.

Because of the large energy region covered by the average, it would in principle be better to separate it into at least two energy bins; the poor statistics of the measurement, however, preclude such an analysis. The average photon energy defines the velocity of the center-of-mass system (CMS):

$$\beta_{cms} = \frac{\bar{E}_\gamma}{\bar{E}_\gamma + M_D}. \tag{5.15}$$

With the lab angle equal to the spectrometer central angle and the CMS defined, the CMS angle is determined (CMS quantities are denoted by *). The cross-section in the CMS is then given by

$$\frac{d\sigma}{d\Omega^*} = \frac{d\sigma}{d\Omega} \cdot \frac{d\Omega}{d\Omega^*}, \tag{5.16}$$

$$\frac{d\Omega}{d\Omega^*} = \gamma_{cms}\left(\frac{p^*}{p}\right)^3\left(1 + \frac{\cos\theta^*}{\beta_p^*}\right), \tag{5.17}$$

where

$$\gamma_{cms} = \frac{1}{\sqrt{1-\beta_{cms}^2}}.$$

1. The Invariant Cross Section: $d\sigma/dt$

In the search for the onset of scaling, one is interested in the energy dependence of the invariant cross section $d\sigma/dt$, where t is the Mandelstam variable given in Equation 1.4. It is given in terms of the CMS cross section by:

$$\frac{d\sigma}{dt} = \frac{d\sigma}{d\Omega^*} \cdot \frac{d\Omega^*}{dt}, \tag{5.18}$$

$$\frac{d\Omega^*}{dt} = \frac{\pi}{\bar{E}_\gamma{}^* p^*}. \tag{5.19}$$

The values of the CMS cross section and $d\Omega^*/dt$ are summarized in Table XIX.

F. Subtraction of Al(γ,p)X Background

1. Multiple Scattering in the Radiator

The background rates from the aluminium end-caps of the target were measured by placing a nearly identical target filled with liquid hydrogen in the beam-path. The hydrogen provides an identical number of radiation lengths of material that the liquid deuterium presents, but protons from it are kinematically forbidden. Assuming the end-caps have equal thickness, the normalization is straight forward: the rates measured with the hydrogen target are subtracted from the deuterium runs, as was done successfully in NE 8. The experimental arrangement for NE 17 is somewhat different though, the radiator is farther upstream (1.5 m compared to 0.8 m) and the inner-diameter of the aluminium flow-guide in the cryogenic liquid is smaller (1 inch instead of 2 inches). The arrangement was in fact below requirements outlined in the proposal [57], but was all that was available. Thus the possibility of electrons multiply scattering in the radiator and illuminating the Al in the flow-guide, which could make the normalization of the subtraction strongly dependent on the beam shape and target position, must be considered.

A particle with charge Z and momentum p, moving at a speed β traversing τ radiation lengths of a material undergoes an RMS deflection given by [5]:

$$\theta_{\rm RMS} = \frac{14.1{\rm MeV/c}}{p\beta}\sqrt{\tau}\left[1+\frac{1}{9}\log_{10}\tau\right]. \tag{5.20}$$

With τ =0.06 and p =1600 MeV/c, Equation 5.20 yields an RMS angle of only 1.85 mr, which is significantly smaller than the $\theta_{critical}$ = 10 mr deflection needed hit the flow-guide. The angular distribution of the multiply-scattered particles is Gaussian out to only $\approx 2.5 \times \theta_{\rm RMS}$, however, with a tail at larger angles dominated by events undergoing a single hard scattering, with a distribution given by [58]:

$$P(\theta) = \frac{1}{8\log 204 Z^{-\frac{1}{3}}}\cdot\left(\frac{\theta}{\theta_{\rm RMS}}\right)^{-3}. \tag{5.21}$$

Thus the severity of potential problems scales as $1/(E_{\rm beam}\theta_{critical})^3$. If we evaluate this parameter for various beam energies run during NE 17, and compare it with the largest value encountered during NE 8 (where rate due to large angle single scattered electrons was not observed), we see there could be a problem at $E_{\rm beam}$ =2.0 GeV and 1.6 GeV.

Since data are taken on the hydrogen target with the radiator absent, it is possible to measure the photoproton production on end-cap aluminium due only to electrons and photons passing through the center of the target. That is, with the hydrogen target, observed photoprotons must come from the aluminium, and with the radiator out, the photons can only be produced in the target aluminium along the beam axis (*i.e.*, the end-caps). With the radiator in, one can calculate the additional rate expected from the additional photon flux; if the observed rate is too large, it is indeed possible that the extra flux is coming from a small fraction of the beam obliquely striking the flow-guide. The expected ratio is given by:

$$R = \frac{Y_{Cu}+Y_{target}}{Y_{target}}, \tag{5.22}$$

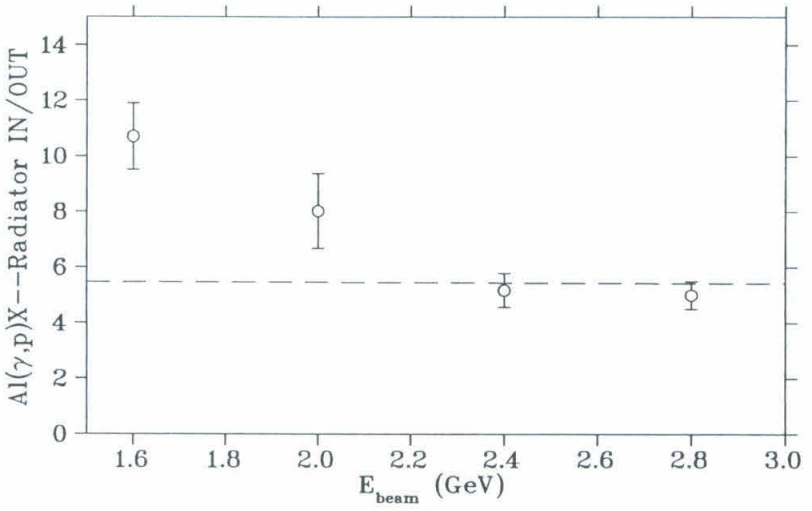

Figure 28

FIG. 30. Background Protons from Aluminium

The figure shows ratio of the proton yields from the aluminium in the target, measured with and without the radiator present. The line is an estimate of this ratio calculated by considering all the material in the beam's path. If a significant amount of beam is undergoing large multiple scattering in the radiator and subsequently striking the flow-guide in the target, one would expect the measured ratio to be higher than the estimate, with the discrepancy decreasing at higher energy.

where the yields from the radiator bremsstrahlung and from the target bremsstrahlung are proportional to

$$Y_{Cu} = N_{Cu}\sigma_{Cu}(N_2 + N_3) \tag{5.23}$$

and

$$Y_{target} = N_1\sigma_{Al}(N_2 + N_3) + N_2\sigma_{Al}(\frac{1}{2}N_2 + N_3) + \frac{1}{2}N_3\sigma_{Al} + N_{H_2}\sigma_{H_2}N_3. \tag{5.24}$$

Here the σ's are the bremsstrahlung cross sections from Al and ^{1}H, and the N are the density of nuclei (with 1, 2 and 3 labeling the aluminium upstream of the target, in the front end-cap and in the rear end-cap, respectively. See Table II and Table III for details). The results of the calculation and measurement for the $\theta^* = 90^o$ data appear in Figure 30. There is clearly excess yield at the two lowest energies, with the effect disappearing at higher energies.

2. Testing the Subtraction

The event rate produced by tails of the electron beam striking the flow-guide can, in principle, depend strongly on small changes in beam shape or position, between runs, thus spoiling the simple normalization prescription for subtracting Al(γ,p)X protons for the LD2 radiator in runs. However, photo-deuterons are produced only by the Al(γ,d)X reaction so that the photo-deuterons can be measured for both the LD_2^{IN} runs and the LH_2^{IN} and compared as a test of the subtraction procedure. The procedure is particularly simple for the $\theta^* = 90^o$ runs, where the proton and deuteron ToF peaks are well separated and the background rate from aluminium is highest. The results appear in Table XV and also in Figure XV. The measured photo-deuteron rates do not indicate a problem with the subtraction; however, the method is only accurate to about 10%.

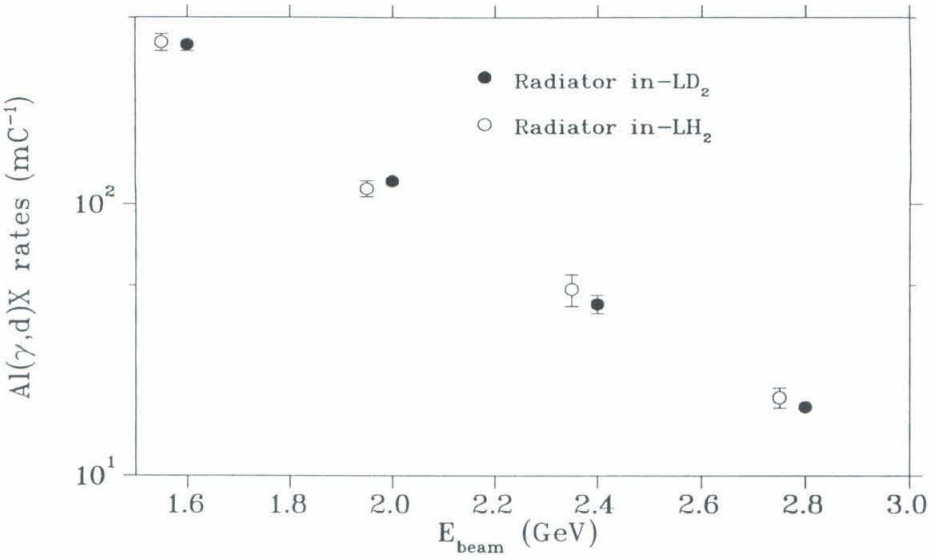

FIG. 31. Al(γ,d)X) Rates

The figure shows the $Al(\gamma,d)X$ rates at $\theta^* = 90^\circ$ measured with the radiator in for both the LD_2 and LH_2 targets. The agreement between the rates indicates that the LH_2 radiator-in subtraction is properly normalized.

TABLE XV. Al(γ,d)X Rates with the Radiator In

$E_{\rm beam}$ (GeV)	LD_2^{IN} Al(γ, d)X rate (mC^{-1})	LH_2^{IN} $Al(\gamma,d)X$ rate (mC^{-1})	Difference (mC^{-1})
1.6	397± 21	405± 29	-8±36
2.0	123±6.0	115±8.2	8±10
2.4	42.7±3.3	48.5± 6.5	-5.8±7.3
2.8	17.9±0.85	19.4±1.62	-1.5±1.8

G. Accidental Background

In addition to background from the target end-caps, there is also background that doesn't come from the target (as defined by the event reconstruction). Event-by-event inspection of these events shows that they have, in general, clean wire-chambers and good time-of-flight measurements; thus they do not result from spurious tracks or other tracking problems, but are in fact real particles that have penetrated the spectrometer shielding and triggered the detector stack. (The 3/3-scintillator trigger, of course, provides no rejection of these events). Reconstruction of the mass of these particles using the ToF information and momentum reconstruction do not in general yield reasonable values, indicating that the particles have not gone through the magnetic optics of the spectrometer (see Figure 32). (That is the particle velocity is accurately measured but it has not been analyzed by the bending magnets. The cutoff below $\beta = 0.4$ is thus explained by the limit in overlap of the 20 ns logic pulses forming the spectrometer trigger). These events are the so-called accidental background, and are significant at forward spectrometer angles.

1. Z_{target} cut

The accidental background does not come from the target, so that a Z_{target} cut removes most of unwanted events. The Z_{target} distribution measured under circumstances in which the accidental background is minimal is shown in Figure 33. The resolution in Z_{target} is poor, so that the width of the distribution is wider than the actual $\approx \pm 7.5$ cm length of the target, but it does agree with the Monte Carlo model of the spectrometer. Based on this agreement, a cut of $|Z_{target} - Z_0| \leq 25$ cm is applied to all the photodisintegration data. The offset Z_0 is necessary because of a slight tilt in the spectrometer hut. The efficiency of the cut is high, and no efficiency correction is applied.

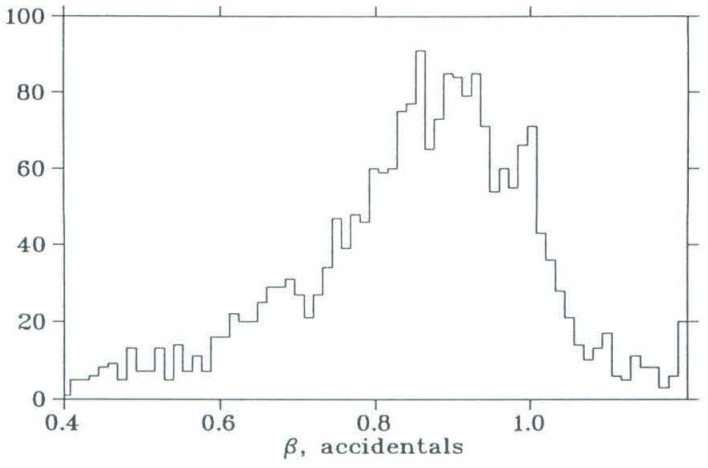

FIG. 32. Accidental Background Time-of-Flight

The figure shows the measured velocity β of events that fail the Z_{target} cut.

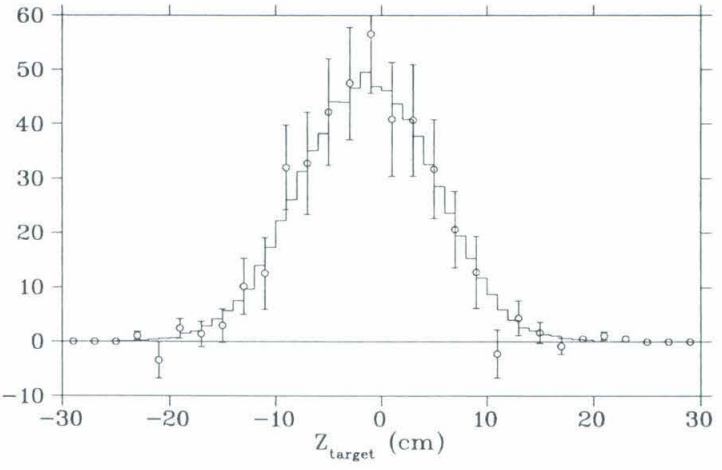

FIG. 33. ^{2}H(γ,p)n Z_{target} Distribution

The data are the Z_{target} distribution of photoprotons from $^2H(\gamma,p)n$ and the histogram is the distribution expected from the Transport model of the spectrometer. Agreement is good, and indicate that the efficiency of the Z_{target} cut is near 100%.

TABLE XVI. Accidental Background Rates

$E_{\rm beam}$(GeV), θ^*	$\frac{LD_2^{in}\text{rate}}{LH_2^{in}\text{rate}}$	$\frac{LD_2^{out}\text{rate}}{LH_2^{out}\text{rate}}$	$\frac{LD_2^{in}\text{rate}}{LD_2^{out}\text{rate}}$	$\frac{LH_2^{out}\text{rate}}{LH_2^{out}\text{rate}}$
1.6, 37°	1.92	2.10	3.71	4.20
2.0, 37°	1.94	1.97	3.16	3.22
2.4, 53°	1.97	1.63	3.09	2.55
2.4, 37°	1.96	2.17	2.88	3.20
2.8, 37°	1.90	2.00	3.22	3.41
4.2, 37°	1.84	1.86	3.08	3.11

2. Accidental Background Rates

The accidental background rate depends on the target and radiator configuration. The relative rates are measured by opening the $\delta\theta$ and ϕ cuts and accepting events that are neither from the target ($Z_{target} > 30\,\text{cm}$) nor in the proton or deuteron ToF peaks. From Table XVI it is clear that the accidental background scales roughly with the density of nucleons in the target (including the end-caps, the ratio of the number of nucleons in the deuterium target to the number in the hydrogen target is 1.95), and is about a factor of three to four larger with the radiator in compared to no radiator.

3. Accidental Background Correction

Because the accidental background is not constrained by the magnetic optics, it is rejected by cuts on reconstructed target quantities. The $\delta\theta$ and ϕ distributions of the accidental background extend from -60 mr to 60 mr and from -200 mr to 120 mr, respectively—well beyond the true acceptance of the spectrometer. Figure 34 shows that both ToF and Z_{target} cuts reject much of the remaining accidental background. Nevertheless, a small fraction lies within all the cuts; furthermore, since the rate is roughly proportional to the number of target nucleons, is will not be completely

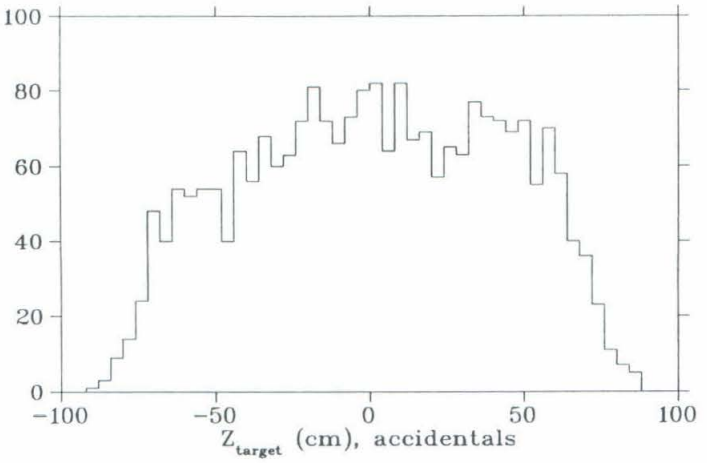

FIG. 34. Accidental Background Z_{target} Distribution

The figure shows the Z_{target} distribution of events with time-of-flight measurements not in the proton or deuteron peaks.

subtracted by the standard subtraction of the LH2 rate from the LD2 rate, and a systematic correction is required.

The Z_{target} distribution is used to estimate the size of the systematic correction and error. Events falling within the angular cuts and ToF-proton peak are histogrammed in Z_{target}; the final photoproton rate is formed in the standard manner. As a crude estimate of the background contamination, the accidental background distributions assumed to be flat in Z_{target}, and the rate outside the Z_{target} cuts is extrapolated under the peak. The rate is mostly small or statistically consistent with zero, however, at the forward angles and high energies, the rate is clearly not zero, in which case a correction is made. The estimate of the rate is subtracted, and a 100% systematic error is assigned to the correction.

H. Measurement of the Cross Section Without the Radiator

One can forgo the potential problems caused by the presence of the radiator, and measure the cross section using only the data taken with the radiator absent. Real bremsstrahlung photons are produced in the 0.19% radiation lengths of aluminium upstream of the target, and the target itself presents 2.1% radiation lengths of liquid deuterium. In addition, the electron beam presents a flux of virtual photons equivalent to $\approx$ 2% of a radiation length. Rate from the aluminium end-caps are removed by subtracting the hydrogen target yield from the deuterium target yield (see Equation 5.2 for comparison):

$$\frac{dN_{d(\gamma(*),p)n}}{dE_\gamma} = \left[\frac{dN^{out}_{LD2}}{dE_\gamma} - \frac{dN^{out}_{LH2}}{dE_\gamma}\right]. \tag{5.25}$$

The proton yield per incident charge from photodisintegration can be written in terms of the bremsstrahlung cross-section ($d\sigma_{brem}/dk$, from [51]) and the photodisintegration cross section ($d\sigma_\gamma/d\Omega$) as:

$$\frac{dN_\gamma}{dE_\gamma} = \left(\frac{1}{2}n_d\frac{d\sigma^{LD_2}_{brem}}{dE_\gamma} + n_{Al}\frac{d\sigma^{Al}_{brem}}{dE_\gamma}\right)\left(n_d\Delta\Omega\frac{d\sigma_\gamma}{d\Omega_p}\right), \tag{5.26}$$

where $\Delta\Omega$ is the solid angle of the detector and n_d and n_{Al} are the densities of target nuclei and aluminium upstream from the target, respectively. Similarly, the yield expected from electro-disintegration can be expressed by:

$$\frac{dN_{e^-}}{dE_\gamma} = \left(n_d\Delta\Omega\frac{d^2\sigma_{e^-}}{d\Omega_p dE_p}\right) \times \left(\frac{dE_\gamma}{dE_p}\right)^{-1}, \tag{5.27}$$

where $d^2\sigma_{e^-}/d\Omega_p dE_p$ is the electro-disintegration cross-section, and dE_γ/dE_p is the Jacobian of the relation between the proton energy and reconstructed photon energy (Equation 5.1). The virtual flux is calculated using the method of Wright and Tiator [52]. They relate the electro-disintegration cross section to the product of a virtual photon spectrum, N_e, and the photodisintegration cross section:

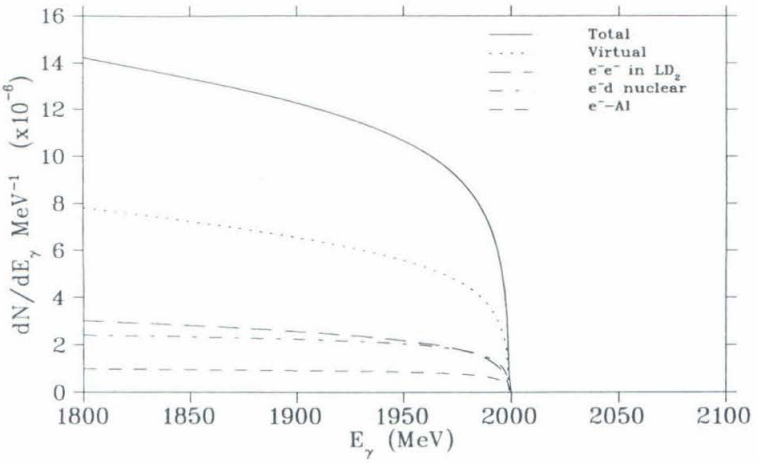

FIG. 35. Bremsstrahlung Fluxes

The figure shows the bremsstrahlung spectra for a beam energy of 2 GeV, using the thin-target formulae in the absence of the radiator. The total flux (solid line) includes contributions form the electron-nuclear yield from deuterium, the electron-electron yield from deuterium, the combined e^-N and e^-e^- from upstream aluminium, and the effective flux of virtual photons, which is calculated using the formula of [52]. *The figure can be compared with the yield from the radiator shown Figure 42.*

$$\frac{d^2\sigma_{e^-}}{d\Omega_p dE_p} = \frac{N_e}{\omega_0} R \frac{d\sigma_\gamma}{d\Omega_p}. \tag{5.28}$$

Here R is a recoil factor important for light targets such as the deuteron, and ω_0 is a kinematic factor with dimensions of energy. Using Equation 5.27 and Equation 5.28, one can define an effective virtual photon flux:

$$\frac{d\sigma^{eff}_{virtual}}{dE_\gamma} = \frac{1}{n_d}\left(\frac{dE_\gamma}{dE_p}\right)^{-1} \frac{N_e}{\omega_0} R. \tag{5.29}$$

The normalized spectra from various bremsstrahlung processes are shown in Figure 35

Given the effective photon flux, $N_{\gamma'}$, defined by integrating the sum of the real and virtual fluxes (Equation 5.26 and Equation 5.29) and the measured proton yield (Y') defined by summing Equation 5.25, the lab cross section is given analogously to

Equation 5.12:

$$\frac{d\sigma}{d\Omega} = \frac{Y'}{N_{\gamma'}\Delta\Omega \mathrm{A}} \ . \tag{5.30}$$

The lab cross section measured with the radiator-out analysis are compared with those measured using the full analysis in Table XVII. Note that statistical fluctuations in the radiator-out analysis cross section are partially anti-correlated with those in the full-analysis, so that direct comparison of the two cross sections can be misleading. In the third column, the difference between the two cross sections is calculated, with the anti-correlation taken into account in the error as follows: With the difference loosely defined by

$$\Delta = \sigma_{full} - \sigma_{radout} =$$
$$\frac{(Y_{LD_2} - Y_{LH_2})^{in} - \bar{f}(Y_{LD_2} - Y_{LH_2})^{out}}{N_\gamma} - \frac{(Y_{LD_2} - Y_{LH_2})^{out}}{N_{\gamma^*}},$$

where the Y's are the various measured yields and the N's are the calculated photon fluxes and $\bar{f} \approx 0.7$ is the mean radiator-out correction, the statistical fluctuations in the Y's contribution to the fluctuation in Δ is given by

$$(\delta\Delta)^2 = \frac{1}{N_\gamma^2}\left((\delta Y^{in}_{LD_2})^2 + (\delta Y^{in}_{LH_2})^2\right) + \left(\frac{\bar{f}}{N_\gamma^2} + \frac{1}{N_{\gamma^*}^2}\right)\left((\delta Y^{out}_{LD_2})^2 + (\delta Y^{out}_{LH_2})^2\right). \tag{5.31}$$

Agreement is reasonable, and does not indicate any serious problems caused by the radiator, although the measured yield with the radiator out is notably ≈10–15% larger than the yield without the radiator. The difference is most likely caused by systematic uncertainties in the virtual spectrum, which arise primarily from the physical assumptions involved in deriving the integral expression for N_e and from the limited accuracy of the approximate evaluation of the integral over the momentum of the undetected electron [52].

TABLE XVII. Raw lab cross sections measured with and without the radiator

E_0,θ (nominal)	$(d\sigma/d\Omega)_{\text{full}}$ nb/sr	$(d\sigma/d\Omega)_{\text{radiator out}}$ nb/sr	$\Delta \times \frac{2}{\sigma_{full}+\sigma_{out}}$
1.6 GeV, 90°	6.30±0.66	7.68±0.72	-0.19± 0.17
2.0 GeV, 90°	1.67±0.23	1.86±0.27	-0.12± 0.24
2.4 GeV, 90°	0.477±0.085	0.494±0.098	-0.088± 0.31
2.8 GeV, 90°	0.153±0.032	0.124±0.047	0.20± 0.50
1.6 GeV, 53°	13.5±1.3	16.3±1.5	-0.12± 0.16
2.0 GeV, 53°	4.42±0.61	3.77±0.70	0.14± 0.26
2.4 GeV, 53°	1.29±0.23	2.23±0.37	-0.54± 0.30
1.6 GeV, 37°	30.0±1.9	38.4±2.2	-0.24± 0.10
2.0 GeV, 37°	10.7±1.1	12.2±1.5	-0.21± 0.20
2.4 GeV, 37°	4.45±0.60	4.70±0.80	-0.053± 0.27
2.8 GeV, 37°	2.24±0.32	1.81±0.38	0.20± 0.29
4.2 GeV, 37°	0.338±0.13	0.348±0.17	0.028± 0.72

I. Systematic Uncertainties

The accuracy of the measured cross sections is limited by systematic uncertainties that arise because of our limited knowledge of the experimental equipment. The systematic errors are loosely divided into two categories: point-to-point uncertainties that effect each run or data point separately, and absolute uncertainties that roughly effect all the data equally. In the measurement of a cross section, as given by Equation 5.3 and Equation 5.12, we must consider systematic uncertainties that arise in the calculation of the photoproton yield, bremsstrahlung flux, solid angle and the density of target nuclei. The systematic errors are summarized in Table XVIII.

The mean electron beam energy is defined by the A-Bend magnets; the absolute calibration of the A-bend is 0.1% [43]. Although errors in the initial electron beam energy do not directly affect the scattering kinematics or cross section, the differential bremsstrahlung cross section is strongly dependent on the absolute beam energy. The uncertainty in the photon flux due to the uncertainty in the absolute electron beam energy was estimated by calculating the yield between two fixed energies while varying the electron beam energy. The resulting flux varied from 0.2% to 0.8%, depending on the beam energy and size of the photon bite.

The absolute uncertainty in the incident charge is estimated to be 0.50%, based on cross calibrations between the toroid and a Faraday cup [46]. Point-to-point uncertainties in the incident charge are estimated at 0.25% from the variations in the difference of the two corrected toroid readings, shown in Figure 36.

The largest uncertainty in the photon flux arises from the accuracy of the thick-target bremsstrahlung formula, which are expected to be good to 3% [51]. A similar accuracy is assigned to the radiator out correction $f(E_\gamma)$, which is based on the same formulae as the flux. The uncertainty in the overall yield, however, is reduced to 0.9%–1.5% because the radiator-out yield is roughly one third of the photodisintegration

TABLE XVIII. Summary of systematic uncertainties

	Absolute Uncertainty	Point-to-Point Uncertainty	Quantity Affected
Beam Energy	0.1%	0.2-0.8%	N_γ
Integrated Charge	0.5%	0.25%	Q_{eff}
Bremsstrahlung Formulae	3%		N_γ
Radiator Thickness	0.5%		N_γ
Reconstruction		1.7%-5.8%	Y
Radiator-Out Correction		0.9%-1.5%	Y
Dead-time		0.08%	Y
Tracking Efficiency	<1%		Y
Particle ID (ToF)	4%		Y
Solid Angle Calculation	3%		$\Delta\Omega$
Target Length	0.04%	<1%	n_{nucl}
Target Density	0.1%	*negl.*	n_{nucl}
Isotopic Purity	0.1%		n_{nucl}
Background Contamination		0-50%	Y

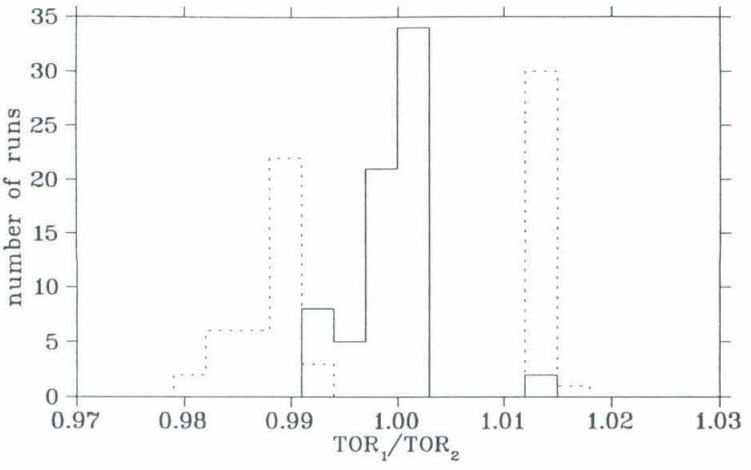

FIG. 36. Toroid Calibration

The figure is a histogram of the run-by-run agreement between the two toroids used to measure the integrated beam current, both before (dotted line) and after (solid line) the toroid calibration correction is applied.

yield. Finally, the error in the photon flux due to the uncertainty in the radiator thickness is estimated at 0.5% [36].

The uncertainty in the photoproton yield due to the accuracy of the reconstruction matrix elements is estimated from the missing-mass-squared calibration procedure (Section IV D 2). The systematic error in the reconstruction of the momentum and angle is used to estimate an error in the reconstructed photon energy at the edges of the photon bite. The uncertainty in the true yield is then roughly proportional to the uncertainty in the width of the measured photon bite; the result varies from 1.7% at $E_{\rm beam} = 1.6$ GeV to 5.8% at $E_{\rm beam} = 4.2$ GeV.

The contribution of the dead-time correction to the uncertainty is expected to be small. The hardware dead-time correction is mostly less than 0.1%, with a much smaller statistical uncertainty. The computer dead-time is in principle exact if the trigger only accepts protons. Because of the large fraction of accidental triggers, there

can be fluctuations in the number of protons missed. The run-to-run estimate of this error is 0.08%. An error of 1% is assigned to the tracking efficiency. The error in the ToF particle identification is estimated at 4% based on ToF-cut dependent variations in measured yield.

The absolute uncertainty in the density of target nucleons arises from uncertainties in the target length, density and isotopic purity of 0.04%, 0.1% and 0.1%, respectively. Because peak currents were small ($< 20\,\mathrm{mA}$), the point-to-point uncertainty in the target density caused by beam heating is ignored. Variations in target length caused by misalignment of the beam and target along with the curvature of the end caps is estimated to be less than 1%.

The solid angle is calculated with the Monte Carlo model that uses a second order Transport deck, described in Section IV B. Although the measurement of the p(e,e′)p cross section using the model reproduced the theoretical result to within 2%, a two percent error is overly optimistic. The model was not entirely successful in reproducing the focal plane distributions measure in p(e,e′)p data, nor did the best-fit reverse reconstruction coefficients exactly match those fit with p(e,e′p) data. The model is further limited by the accuracy with which the quadrupole strengths are known. Models with various quadrupole strengths within tolerances were tested. Based on the results, a 3% systematic error is assigned to the calculated solid angle.

Thus far errors in the measured laboratory cross section $d\sigma/d\Omega$ have been discussed. These errors propagate linearly to the center-of-mass cross section $d\sigma/d\Omega^*$ and the invariant cross section $d\sigma/dt$. The boosted cross sections pick up additional systematic errors resulting from the uncertainty in the boost parameters, defined by the mean photon energy and the spectrometer angle. The spectrometer angle is calibrated to 0.005°, and the resulting systematic error is negligible. The uncertainty in the mean photon energy is estimated as half the uncertainty of the photon energy at the edge of the acceptance, and ranges from 0.6 MeV to 1.6 MeV at various kinemat-

TABLE XIX. d(γ,p)n Cross Sections

E_{beam} (GeV)	$\bar{E}_\gamma$ (MeV)	s (GeV^2)	θ^*	$d\Omega^*/dt$ (nb/GeV^2)	$d\sigma/d\Omega^*$ (nb/sr)
1.598	1522 ± 1.8	9.227	84.23°	2.80	3.795±0.404±0.296
	1539 ± 1.4	9.291	52.51°	2.76	5.574±0.531±0.434
	1543 ± 1.3	9.306	36.66°	2.75	10.87±0.693±0.847
2.015	1934 ± 2.4	10.77	88.28°	2.11	1.008±0.137±0.080
	1956 ± 1.8	10.86	52.58°	2.08	1.620±0.223±0.129
	1961 ± 1.6	10.87	36.71°	2.08	3.277±0.366±0.299
2.402	2321 ± 2.9	12.22	89.38°	1.71	0.2741±0.0490±0.0224
	2343 ± 2.1	12.31	52.65°	1.69	0.4313±0.0753±0.0358
	2344 ± 1.9	12.31	36.76°	1.69	1.201±0.173±0.131
2.801	2721 ± 3.4	13.73	89.44°	1.43	0.0830±0.017±0.007
	2748 ± 2.2	13.83	36.79°	1.41	0.504±0.085±0.096
4.214	4162 ± 3.2	19.13	36.85°	0.89	0.038±0.026±0.029

ics. From Equation 5.17 and Equation 5.19 defining the Jacobian of the boost, the additional errors in the boosted cross sections are small, roughly 0.01%. The quantity $s^{11}d\sigma/dt$ does pick up an error of order 0.1% though.

The various systematic errors are added in quadrature to yield an overall systematic error which is then added in quadrature to the statistical error to give the total error. The center-of-mass cross sections along with the statistical and systematic error appear in Table XIX.

J. Summary

In this chapter the final steps in the formation of the photodisintegration cross section have been discussed, particularly the isolation of the photoproton rate from the two-body process. The steps involved include the reconstruction of the initial photon energy and the subtraction of the backgrounds from electrodisintegration and the aluminium end-caps of the target. Systematic errors in the measurement were also discussed.

A large part of the chapter focused on available systematic methods to determine if the 0.77 g/cm^2 Cu radiator upstream from the target and detector caused significant problems. Of particular concern is the size of the electron (and photon) beams at the target, and also the shielding of the spectrometer from background produced in the radiator. The discussion is particularly important for NE 17 because the experiment was allotted no check out time devoted to studying bremsstrahlung production with the radiator. Furthermore, the two crucial elements in the experimental apparatus—the distance of the radiator from the target and the target diameter—were well below the design specified in the NE 17 proposal. Although it is not entirely clear if the beam spot on target was too large (as suggested by Figure 30), the test of the subtraction procedure with photo-deuterons produced in target aluminium was successful. Although the target and detector were heavily shielded, no shielding studies were done with the radiator present, and quadrupole magnet after the target chamber, used in NE 8 to limit accidental background from beam spray, was not available. At forward spectrometer angles, the accidental background was significant. The $E_{\rm beam}$=4.2 GeV measurement was particularly problematic: the ≈25% dead-time was almost entirely caused by accidental scintillator coincidences—in which no track is present. Furthermore, over 90% of the trackable events did not reconstruct to the target. Similar background is seen at other kinematics, but is by no means as severe. An ≈10%

correction is made to the 2.8 GeV data at 37°, and other data point pick up a $< 4\%$ correction, or none at all.

VI. RESULTS AND DISCUSSION

In this chapter, the measured cross sections are presented and interpreted within the framework of several theoretical models. Previous measurements at lower energies are included for completeness. Relevance to the QCD-based and hadron-based predictions presented in Chapter I is discussed.

A. Results

Table XX shows the energies and angles at which data have been taken in both the NE 8 experiment and the NE 17 experiment presented in this thesis. The SLAC experiment NE 8 was the first measurement of ^{2}H(γ,p)n above $E_\gamma = 1\,\mathrm{GeV}$ and laid much of the ground work for the NE 17 measurement. Thus Table XX represents a summary of the ^{2}H(γ,p)n program at SLAC. NE 8 used the 1.6 GeV/c spectrometer to detect photoprotons [2], so that at the highest beam energies, the minimum center-of-mass angle measurable was limited by the spectrometer momentum ($P_{1.6} \leq 1.5\,\mathrm{GeV/c}$). NE 17 was limited to forward center-of-mass angles because of limitations on the lab-angle of the 8 GeV/c spectrometer ($15^\circ < \theta_8 < 53^\circ$). Although data at 4.2 GeV were taken during NE 17, systematic problems arising from accidental background limit its significance.

The ^{2}H(γ,p)n differential cross sections at beam energies of 1.6 GeV, 2.0 GeV, 2.4 GeV and 2.8 GeV are presented in Figure 37, along with previous data from NE 8 [36]. The two experiments overlap at 1.6 GeV and $\theta^* = 90^\circ$, and are in good agreement. At 1.6 GeV we have extended the existing angular distribution data down to $\theta^* = 37^\circ$; the center-of-mass cross section is forward-backward peaked, and at higher beam energies the forward-peaking becomes stronger. An energy-independent angular distribution is expected if the cross section scales at each angle.

The energy dependence of the cross section at center-of-mass angles of 90°, 53°

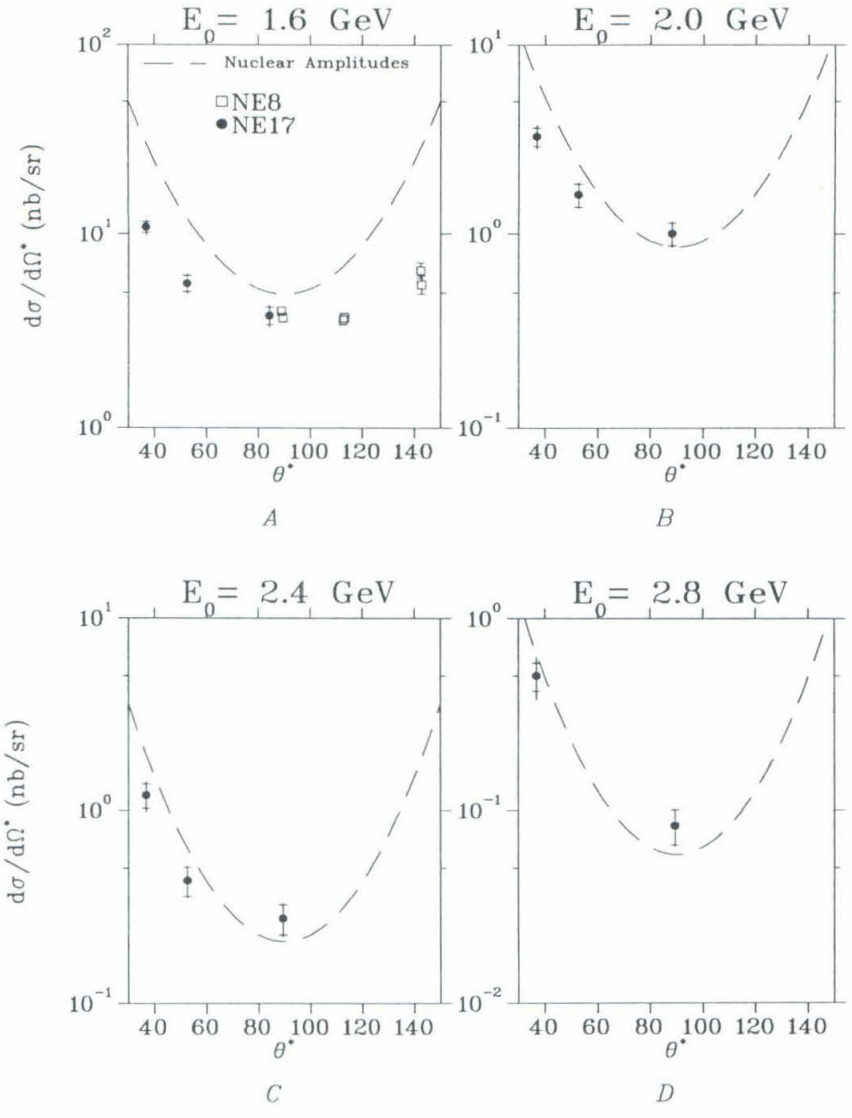

FIG. 37. Angular Distributions

The figures A–D show the differential cross section in the center-of-mass measured at beam energies of 1.6 GeV, 2.0 GeV, 2.4 GeV and 2.8 GeV, respectively. The NE 8 data are included at $E_{\text{beam}} = 1.6$ *GeV, and are in agreement with the present measurement. The dashed line is the reduced nuclear amplitude prediction with* $f^2(\theta^*) \equiv 1$, *normalized to previously measured data* [2] *near 1 GeV.*

TABLE XX. $\gamma d \rightarrow pn$ at SLAC

E_{beam} GeV	0.8	1.0	1.2	1.4	1.6	1.8	2.0	2.4	2.8	4.2
$\theta^* = 37°$					NE17		NE17	NE17	NE17	NE17[†]
$\theta^* = 53°$		NE8	NE8		NE17		NE17	NE17	NE17	
$\theta^* = 78°$	NE8	NE8								
$\theta^* = 90°$	NE8	NE8	NE8	NE8	NE8/NE17	NE8	NE17	NE17	NE17	
$\theta^* = 113°$	NE8	NE8	NE8	NE8	NE8	NE8				
$\theta^* = 127°$	NE8	NE8								
$\theta^* = 143°$	NE8	NE8	NE8	NE8	NE8					

[†]The data at this energy are of limited significance.

and 37° are shown in Figure 38. Data from Dougan *et al.* [59], Ching *et al.* [60], Myers *et al.* [61], Arends *et al.* [62] and NE 8 [2] are also plotted. Both the center-of-mass cross section and $s^{11}d\sigma/dt$ are displayed separately. Perhaps the most notable features of Figure 39 are the nearly constant values of $s^{11}d\sigma/dt$ at $\theta^* = 90°$ and $\theta^* = 53°$ above $E_\gamma = 1\,\text{GeV}$ and $E_\gamma = 0.8\,\text{GeV}$, respectively.

B. Comparison with Theoretical Models and Discussion

1. Constituent Counting

According to the constituent counting rules of QCD discussed in Chapter I, the energy dependence of γd $\rightarrow$ pn invariant cross section is given by $d\sigma/dt \sim s^{-11}$ in the region where $s \gg M_d^2 = 3.518\ \text{GeV}^2$. Consequently the quantity $s^{11}d\sigma/dt$ should approach a constant in the region where perturbative QCD describes the dynamics of the reaction. As Figure 39 shows, the data are consistent with a constant at both $\theta^* = 90°$ and $\theta^* = 53°$, however $s^{11}d\sigma/dt$ rises with energy at $\theta^* = 37°$. Including the NE 8 data at 90° and 53°, we see that the onset of scaling appears at photon

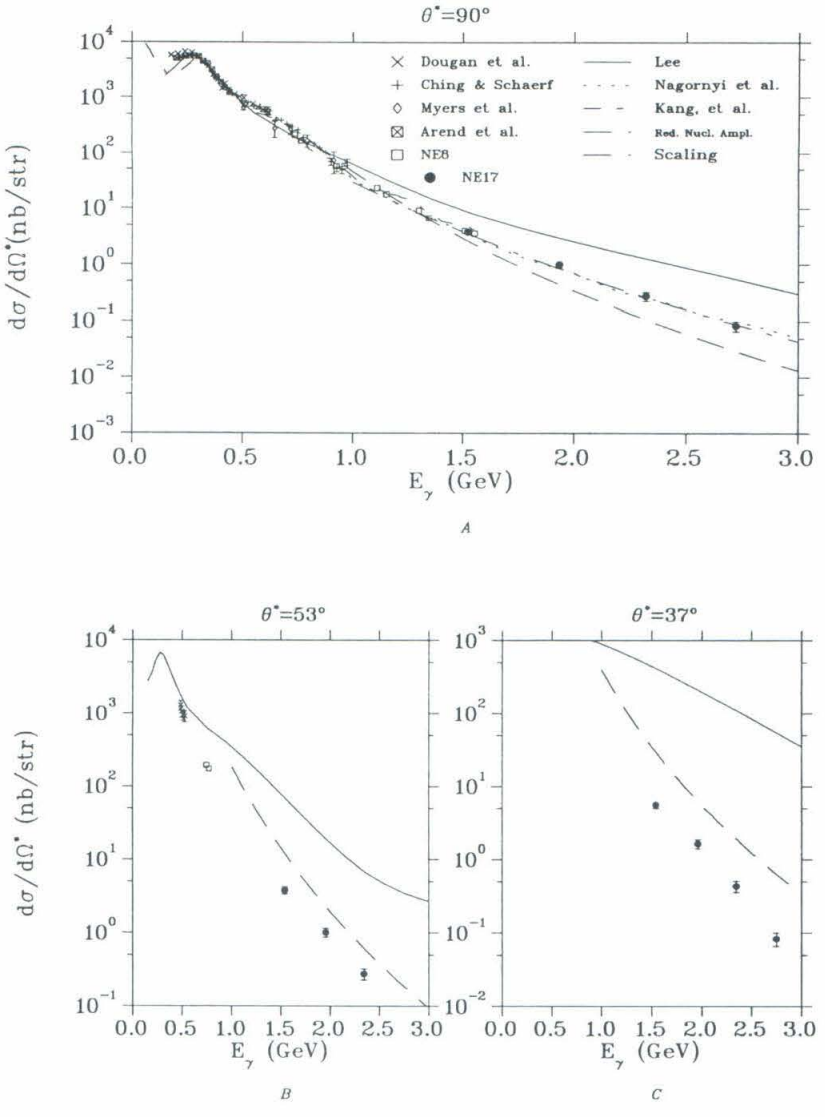

FIG. 38. Energy Dependence of $d\sigma/d\Omega^*$

The figures A–C show the energy dependence of the center-of-mass cross section measured near 90 °, 53 ° and 37 °, respectively. Previous measurements [59–62,2] *are also shown. The curves represent the theoretical predictions of* [11–14,31].

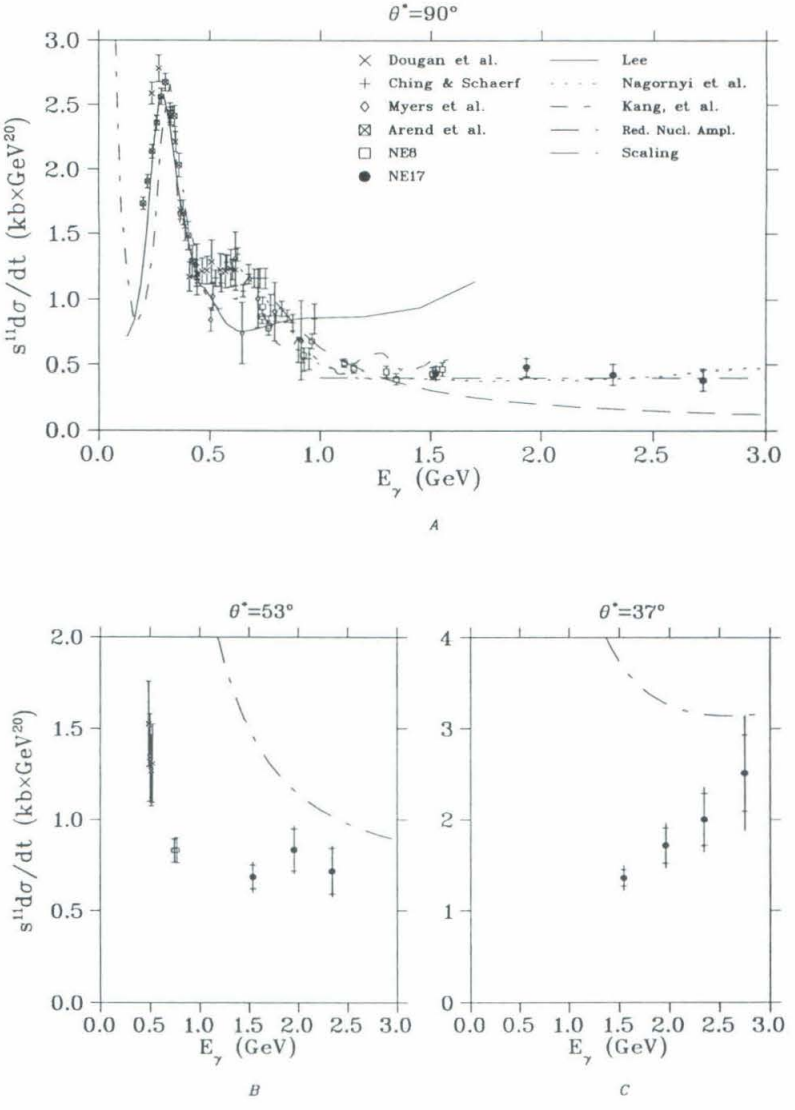

FIG. 39. The Invariant Cross Section

The figures A–C show the energy dependence of the invariant cross section measured near 90 °, 53 ° and 37 °, respectively. Previous measurements [59–62,2] *are also shown. The curves represent the theoretical predictions of* [11–14,31]. *The quantity* $s^{11}d\sigma/dt$ *is plotted, so that data can be compared on a linear scale over a wide range of energy.*

TABLE XXI. Fits to $\frac{d\sigma}{dt} \sim s^{-n}$

θ^*	E_γ	$\lvert t_{\rm p}^{\gamma d}\rvert$	n
	GeV	$(\mathrm{GeV/c})^2$	
90°	1.151–2.772	1.08–2.55	11.2 ± 0.21
53°	0.744–2.343	0.974–3.32	11.3 ± 0.19
37°	1.543–2.748	2.36–4.35	9.50 ± 0.35

energies of 1.1 GeV and 0.76 GeV, respectively. Interestingly, the momentum transfer to the recoiling proton (Equation 1.20) at which the data begin to follow the scaling law is $\approx 1\,(\mathrm{GeV/c})^2$ for both 90° and 53 ° data. The data at 37° do not show scaling behavior, even though the momentum transferred to the proton is high (2.4–4.4 $(\mathrm{GeV/c})^2$), possibly because the momentum transferred to the neutron remains small ($|t| \lesssim 0.81(\mathrm{GeV/c})^2$). Fits to the scaling behavior are shown in Table XXI.

2. Reduced Nuclear Amplitudes

In the reduced nuclear amplitudes (RNA) model of Brodsky and Hiller [12], the known scaling behavior of the neutron and proton are factored out of the photodisintegration amplitude; the resulting reduced amplitude is expected to scale as and elementary amplitude with four constituents ($\sim p_T^{-1}$). Specifically, the center-of-mass cross section is

$$\frac{d\sigma}{d\Omega^*} \propto \frac{1}{\sqrt{s(s-M_{\rm d}^2)}} F_{\rm p}^2(\hat{t}_{\rm p}) F_{\rm n}^2(\hat{t}_{\rm n}) \frac{1}{P_T^2} f^2(\theta^*), \tag{6.1}$$

where, if the theory is correct, $f(\theta^*)$ is independent of energy. The dipole form factors are used for the nucleon, and are evaluated at the momentum transfer to each nucleon. At large momentum transfers ($|t| \gg 0.71\,(\mathrm{GeV/c})^2$) the dipole form factor behaves like $F_N(|t|) \sim |t|^{-2}$, so that at large s and t with t/s fixed, Equation 6.1 becomes

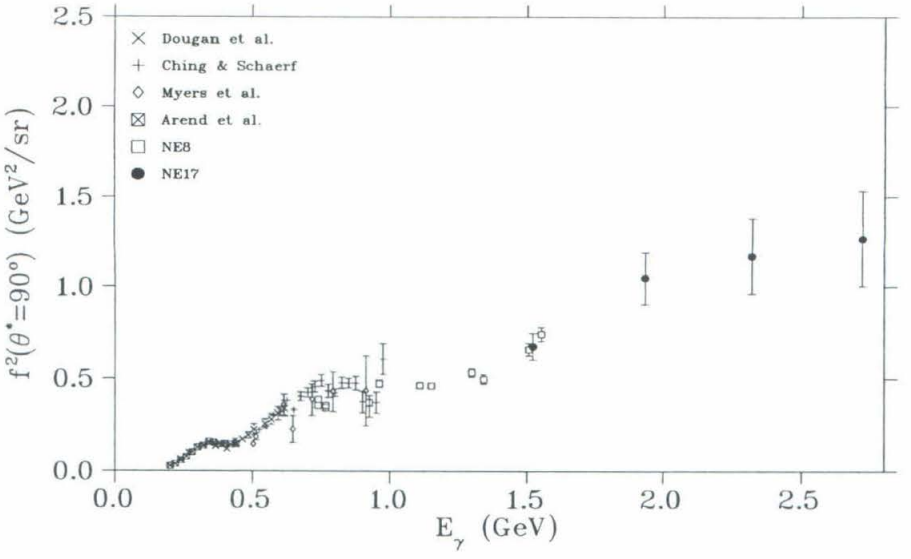

FIG. 40. The Reduced Nuclear Amplitude

The figures show the energy dependence of the quantity $f^2(\theta = 90°)$ *of [12]. Other data* [59–62,2] *are also shown. In the reduced nuclear amplitudes approach,* $f^2(\theta^*)$ *should be independent of energy above 1 GeV.*

$$\frac{d\sigma}{d\Omega^*} \sim s^{-10} \longrightarrow \frac{d\sigma}{dt} \sim s^{-11}, \tag{6.2}$$

and the standard pQCD scaling laws are recovered. The advantage of the reduced nuclear amplitude approach is that by specifically including the mass scales 0.71 GeV^2 and M_d^2, one can effectively produce scaling at lower s, even if the cross section is falling faster than s^{-11}. The NE 17 data from 1.6–2.8 GeV at 90° are fit equally well by the reduced nuclear amplitude approach or a constant, however it seems unreasonable to ignore the previous NE 8 data at lower energy where the RNA approach is expected to apply. In Figure 39, the RNA calculation has been normalized to the NE 8 point near 1 GeV; agreement is less favorable than the $s^{-11} = constant$ prediction. Figure 40 shows f^2, defined by Equation 6.1, versus photon energy. Clearly, f^2 is not constant over the energy range 1.0–2.8 GeV.

Brodsky and Hiller [12] propose a model for the angular distribution based on the photodisintegration of a meson by a virtual photon:

$$f^2(\theta^*) = N\frac{(ue_1 + te_2)^2}{tu} \tag{6.3}$$

$$\rightarrow N \text{ for transverse photons.} \tag{6.4}$$

Here N is an arbitrary normalization the e_i's are the strengths of the couplings of the quark and antiquark in the meson. Although the data are forward-peaked, the peaking is significantly less than the model, and also depends on energy.

3. Meson-Exchange Calculations

It was clear from the NE 8 data at 90° that the coupled channel meson-exchange calculation by Lee [13] has difficulties above E_γ=1 GeV, and it is not surprising that the calculation does not describe the energy dependence of the NE 17 data well. At the other angles the shortcomings are even more severe: the calculation is too large by two orders of magnitude. Although these discrepancies certainly rule out Lee's calculation, they do not rule out the whole meson-exchange approach. The inclusion of heavier resonances and relativistic effects, other than trivial kinematic relations, needs to be investigated. The Bonn group [31] included all nucleon resonances with spin $\leq 5/2$ and $m \leq$2 GeV and reproduced the data at 90° up to $E_\gamma = 1.6$ GeV. Their calculation allowed the πNN cutoff to change by 40% for photon energies above 0.7 GeV, so that it is not clear if the agreement can in fact be attributed to the inclusion of more resonances.

A crucial feature in all the conventional meson-exchange models is their self-consistency: the models are constrained by available data where ever possible. Lee, for example, uses available data on photo-meson production, NN phase shifts and NN total cross sections to constrain his model. The model is further constrained by low-energy ^{2}H(γ,p)n data. Given the large number of free parameters- the various coupling

constants, cut-off masses in form factors and the widths of resonances- agreement with a limited set of data is not remarkable. Thus the credibility of a conventional meson-exchange model rests in its successful description of both the ^{2}H(γ,p)n data at intermediate energy, lower energy, and also in its consistency with related amplitudes.

4. Asymptotic Amplitudes

The asymptotic amplitudes calculation outlined in Chapter I predicts a scaling-like behavior at $\theta^* = 90^\circ$ in the energy range covered by this experiment. Agreement with the prediction is shown in Figure 39. The curve, taken directly from [14], had been normalized with the experimental value at $E_\gamma = 1\,\mathrm{GeV}$ and had assumed $\alpha = 0$. Agreement is good over the extent of the calculation, which extends down to $E_\gamma = 0.6\,\mathrm{GeV}$. Explicit calculations of energy dependence at other angles are not available, although angular distribution at E_γ =1, 2 and 3 GeV based on several models of the deuteron's Fock state [63,64] can be found in [14]. Both models predict far too much forward peaking, with details that are highly sensitive to the deuteron structure, particularly in the region $\theta^* < 70^\circ$ or $\theta^* > 120^\circ$. The qualitative conclusion that the cross section should expect scale for $50^\circ < \theta^* < 130^\circ$ and that $s^{-11}d\sigma/dt$ should be a rising function of energy for other center-of-mass angles is consistent with the present data. It must be pointed out the asymptotic amplitudes approach relaxes some of the constraints of standard meson-exchange calculation; furthermore the method has not been applied to similar reactions such as $\gamma p \rightarrow \pi N$, and thus the significance of the agreement is not yet clear.

C. Summary

Our main result is the persistence of the scaling behavior above $E_\gamma \approx 1\,\mathrm{GeV}$ in the ^{2}H(γ,p)n cross section at 90° in the center-of-mass first observed by NE 8. The

data at $\theta^* = 53^\circ$ also show scaling behavior above $E_\gamma \approx 0.8\,\mathrm{GeV}$. The onset of scaling at both the angles occurs if the momentum transfer to the outgoing proton is $> 1\,(\mathrm{GeV/c})^2$. At $\theta^* = 37^\circ$ the scaling behavior is not seen—perhaps because the momentum transfer to the neutron remains small. The angular distributions are forward-peaked; data at $E_\gamma = 1.6\,\mathrm{GeV}$ for $37^\circ \leq \theta \leq \theta = 143^\circ$ now exist, and the forward cross section is larger than the backward cross section—a result consistent with recent quark-model predictions [65].

If the scaling is indeed due to perturbative QCD, the result does not necessarily contradict the results of measurements of the electric form factor $A(Q^2)$ [66] and the magnetic form factor $B(Q^2)$ [67] of the deuteron. $A(Q^2)$ does not show scaling behavior even at momentum transfers as high as $Q^2 = 4\,(\mathrm{GeV/c})^2$, while $B(Q^2)$ has a diffraction minimum near $Q^2 = 2\,(\mathrm{GeV/c})^2$ that is characteristic of a two-nucleon description of the deuteron [68]. As described in Section I C 1, at $Q^2 = 4\,(\mathrm{GeV/c})^2$ in elastic electron-deuteron scattering, the average momentum transfer to the two nucleons is only $(Q/2)^2 = 1\,(\mathrm{GeV/c})^2$, while it appears that the observance of scaling in the ^{2}H(γ,p)n reaction requires $> 1\,(\mathrm{GeV/c})^2$ of momentum transfer to the outgoing nucleons. Thus the observed scaling in ^{2}H(γ,p)n and lack thereof in ^{2}H(e,e′)^{2}H are not contradictory.

Clearly more theoretical and experimental work are needed to understand the origin of the observed energy dependence. Whether the behavior at 90° is attributable to pQCD or to the precocious scaling predicted by asymptotic amplitudes can be answered with higher statistics data, where logarithmic scaling violations and interference effects unique to QCD could be observed [57,69,70]. It has also been suggested [14] that a measurement of the asymmetry in the ^{2}H($\vec{\gamma}$,p)n cross section between photons polarized parallel to and perpendicular to the reaction plane could clearly identify the cause of the scaling behavior. Regardless, no conventional meson-exchange calculation has satisfactorily predicted the observed angular distributions,

and theoretical work is needed along those lines. Experimentally, one would like to see the measurement extended in the backward direction ($\theta^* > 90^o$), and of course to even higher energies.

VII. CONCLUSIONS

The differential cross section for the ^{2}H(γ,p)n reaction has been measured at several center-of-mass angles with energies from 1.6 GeV to 2.8 GeV. The results at center-of-mass angles of 90° and 53° (the latter measured up to $E = 2.4$ GeV) are consistent with the dimensional scaling laws of perturbative QCD, which predict an energy dependence described by $d\sigma/dt \sim s^{-11}$ [11]. The observed fall of with increasing s at $\theta^* = 37°$, however, is slower than s^{-11}. The QCD-based reduced nuclear amplitude approach of [12], does not describe the energy dependence of the data. We have extended the angular distribution measurement by the NE 8 collaboration [2] at $E_\gamma = 1.6$ GeV into the forward direction; the center-of-mass cross section begins to show forward-backward peaking at photon energies of 1.6 GeV, with the forward-peaking increasing at higher energy. The conventional meson model of Lee [13] greatly over-estimates the forward-peaking of the cross section, and fails to predict the observed $\sim s^{-11}$ fall-off of the invariant cross section with energy. Whether or not the results indicate that the onset of perturbative QCD has been observed is not entirely clear. Theoretically, the validity of applying pQCD to medium-energy nuclear physics is still under debate [21]. Furthermore, the energy dependence of the cross-section at $\theta^* = 90°$ is in agreement with the asymptotic-amplitude calculations of Nagornyĭ *et al.* [14], which are based only on meson and baryon degrees of freedom; the measured angular dependences also support qualitative predictions of the theory.

It is widely believed that in the search for scaling in exclusive nuclear reactions, the transfer of the largest possible momentum is paramount. Thus photoreactions provide and extremely promising tool in this search, since the photon imparts all of its energy and momentum to the nuclear system. The NE 17 experiment presented here has studied the ^{2}H(γ,p)n at several center-of-mass angles with photons energies up to 2.8 GeV, thereby achieving momentum transfers to the outgoing proton as high as

4.4 $(GeV/c)^2$—hitherto unattainable in elastic electron-deuteron scattering because of the rapidly declining cross section. The experiment effectively extended the program begun by the NE 8 experiment [2], which measured the $^2H(\gamma,p)n$ cross section with photon energies from 0.7 to 1.8 GeV.

Our understanding of the transition from meson-baryon degrees of freedom to quark-gluon degrees of freedom is far from complete. If indeed the observed energy dependence of the $^2H(\gamma,p)n$ cross section at $\theta^* = 90^\circ$ and 53° is attributable to pQCD, the failure of the scaling law at $\theta^* = 37^\circ$ must be explained. Further theoretical work with meson-baryon degrees of freedom is also needed. For a meson-baryon based theory to be deemed entirely successful, angular distributions and absolute normalizations of cross section must be reproduced.

Experimentally, photonuclear reactions have only begun to be exploited. Experiment 89-012 has been approved at CEBAF [71], and will provide higher statistics data on the $^2H(\gamma,p)n$ reaction in the energy covered in NE 17, and beyond. Furthermore, Holt [72] has suggested the possibility of investigating $^2H(\gamma,d)\pi^0$ and $^3He(\gamma,d)H$ at CEBAF to help us understand asymptotic scaling in nuclear reactions.

APPENDIX A: BREMSSTRAHLUNG FLUX

In the limit of an infinitely thin radiator of thickness $d\tau$, the photon flux (photons per incident electron per MeV) produced by electrons with energy E_0 is given simply by the expression

$$\frac{dN_\gamma}{dk} = \frac{X_0 N_A d\tau}{A} \frac{d\sigma_{brem}}{dk}(E_0, k), \tag{A1}$$

where A is the atomic weight and X_0 (gm/cm^2) the radiation length of the radiator material. The bremsstrahlung cross-section, $\frac{d\sigma_{brem}}{dk}(E_0, k)$, is summarized by Mathews and Owens [51] and includes both electron-nuclear and electron-electron emission. Equation A1 is known as the *thin-target* bremsstrahlung spectrum, and is, in fact, only approximate—it over-estimates the yield near the tip by about 15%. A more accurate calculation of the flux, using the *thick-target* spectrum, includes the finite energy spread of the beam, straggling and multiple scattering of the electron beam in the radiator and absorption of photons in both the radiator and the target.

Electrons with energy $E_0 \gg m_e$ passing through τ radiations length of material undergo an r.m.s deflection of [5]

$$14.4\,\mathrm{MeV}/E_0\sqrt{\tau} \lesssim 2.2\,\mathrm{mr}, \tag{A2}$$

while the bremsstrahlung flux is peaked in the forward direction on the surface of a cone with half-angle $\theta \approx m_e/E_0 \lesssim 0.3\,\mathrm{mr}$ [58]. The radiator is 150 cm upstream from the target (which is 1" in diameter) so that there is effectively no photon loss from multiple scattering.

At photon energies above 1 GeV, compton scattering and the photoelectric effect are negligible; photon attenuation is caused by electron-positron pair production [73]. The total pair production cross section determines the photon attenuation length, μ, and has been extensively tabulated by Tsai [74]. There is a slight energy dependence

TABLE XXII. Energy Dependence of $\gamma \rightarrow e^- e^+$ Cross Section†

E	μ_{Cu}	μ_{LD_2}	μ_{Al}
GeV	g/cm^2	g/cm^2	g/cm^2
1.6	17.25	174.7	32.54
2.0	17.08	171.1	32.16
2.4	17.05	170.4	32.08
2.8	17.01	169.7	32.00
4.2	16.90	167.2	31.74

†The photon attenuation length is related to the pair production cross sectoion by $\mu = X_0[\frac{7}{9}(1-\xi)]^{-1}$, where $\xi = [\sigma(\infty) - \sigma(E)]/\sigma(\infty)$.

over the energy range of the experiment shown in Table XXII. Absorption is roughly 2% and 0.9% in the radiator and target, respectively.

As the electron beam traverses the radiator, electrons lose energy in collisions with atomic electrons (ionization) and by radiating photons in the field of the Cu atoms (bremsstrahlung), thus depleting the number of high energy electrons available to produce hard photons within 100 MeV of the beam energy. Ionization losses are determined by the Moeller cross section ($\sim \alpha^2 Z/\Delta E^2$), while radiative loses are determined by the bremsstrahlung cross section ($\sim \alpha^3 Z^2/\Delta E$) so that for energy losses ΔE large (small) compared to 20 MeV/$(Z+1) \approx$ 0.7MeV bremsstrahlung (ionization) dominates [75]. In calculating the useful flux for this experiment, we are concerned with energy losses from roughly 10–100 MeV so that straggling in the ionization loss can be ignored (the Landau peak is 0.1 MeV wide). Hence the electron energy distribution at a depth t in the radiator, $I(E, E', Z, t)$, can be calculated considering only radiative processes. The function $I(E, E', Z, t)$ is the solution of a so called electron-diffusion equation, describing the probability of energy transfer from E to $E' < E$ as the electron penetrates deeper into the radiator. The depth t

plays the role of a time parameter. The equation is not soluable analytically with the correct bremsstrahlung shape given by Φ in Equation A3 [74]. Several authors [73,77], however, have found analytic solutions based on non-physical bremsstrahlung shapes, while Early [76] has solved the problem numerically with the correct bremsstrahlung shape (in the limit of complete screening). Both Tsai [75] and Miller [78] have found analytic approximations to Early's numerical results. A comprehensive discussion of the various approaches can be found in [76,74]. Although Miller's result is more accurate than Tsai's original result, it is not a convenient form for integration; we use a modified version of Tsai's result that is both convenient and accurate to within 1% for $t < 0.1$ radiation lengths and $E - E' = \omega < 0.8E$:

$$I(E, E-\omega, Z, t)d\omega = N \cdot \frac{1}{\Gamma(1+bt)} \left[(\frac{\omega}{E})^{bt} \right] \frac{bt}{\omega} \left[\Phi(\frac{\omega}{E}) \right] d\omega, \tag{A3}$$

$$\Phi(\frac{\omega}{E}) = 1 - (\frac{\omega}{E}) + \frac{3}{4}(\frac{\omega}{E})^2 \tag{A4}$$

$$\approx \omega \frac{d\sigma_{brem}}{d\omega}(E, \omega).$$

$\Phi(\frac{\omega}{E})$ represents the shape of the bremsstrahlung spectrum in the Born approximation and the relativistic limit with complete screening. Although $\Phi(\frac{\omega}{E})$ differs from the actual shape of the spectrum given by Mathews and Owens (particularly near the end-point where the screening is not complete), the behavior for small ω is accurate so that straggling from multiple (actually infinite) soft-photon emission is well reproduced. The parameter b normalizes the total amount of energy loss and is given in terms of the low photon energy limit of the bremsstrahlung cross section:

$$b \equiv \lim_{k \to 0} \frac{X_0 N_A}{A} \frac{d\sigma_{brem}}{dk}(E \to \infty, k) \tag{A5}$$

$$= \frac{4}{3} \left[1 + \frac{1}{12} \frac{Z+1}{Z+\eta} / \log 184.15 Z^{-\frac{1}{3}} \right], \tag{A6}$$

$$\eta = \frac{\log 1194 Z^{-\frac{2}{3}}}{\log 184.15 Z^{-\frac{1}{3}}}. \tag{A7}$$

The normalization constant N in Equation A3 is the only modification to Tsai's original result, and ensures that to yield integrates to unity. The $\approx 1\%$ increase in

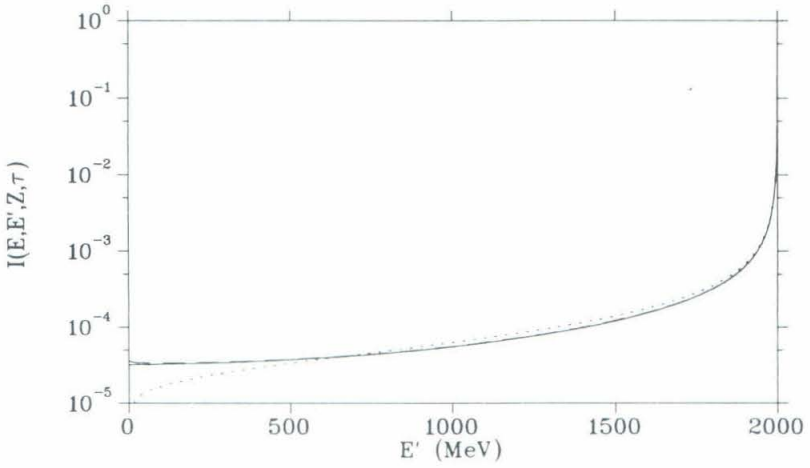

FIG. 41. Electron Radiative Straggling

The Figure shows the radiative straggling function $I(E, E', Z, \tau)$*, calculated for 2 GeV electrons passing through 6% RL of Cu (i.e.* $E = 2\ GeV$*,* $Z = 29$ *and* $\tau = 0.06$*). The solid line is Equation A3 and the dashed line is the similar, but more accurate result, from* [78]*. Neither formula is accurate below* $E' = 0.2 \times E_0 = 400\ MeV$*. The dotted line is from* [73].

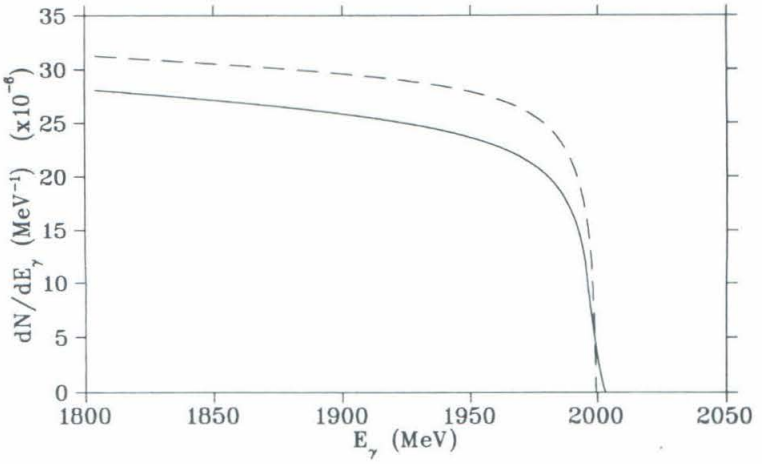

FIG. 42. *Thick-Target* and *Thin-Target* Bremsstrahlung

The Figure shows the bremsstrahlung spectrum calculated according to the thin-target formula, Equation A1 (dashed line), and the more accurate thick-target formula, Equation A9 (solid line). The calculation is for a 6% RL Cu radiator, with $E_0 = 2.0\ GeV$ *and* $\Delta E/E_0 = 0.4\%$.

the straggling brings the analytic result closer to Early's numerical result. N is given by:

$$N = \Gamma(1+bt)\left[\frac{1}{bt} - \frac{1}{1+bt} + \frac{3}{4}\frac{1}{2+bt}\right]^{-1} \qquad \text{(A8)}$$
$$\approx 1.01 \quad .$$

With the above formulae, the photon spectrum produced by an electron beam with mean energy E_0 and flat energy spread with full width Δ passing through a copper radiator of thickness t_{rad} (in units of radiation length) is given by:

$$\frac{dN_\gamma}{dk} = \frac{X_0 N_A}{A}\int_0^{t_{rad}} d\tau e^{(t_{rad}-\tau)/\mu'}\int_{E_0-\Delta/2}^{E_0+\Delta/2}\frac{dE}{\Delta}\int_k^E dE' I(E,E',Z,\tau)\frac{d\sigma_{brem}}{dk}(E',k). \qquad \text{(A9)}$$

The integral is evaluated numerically with the results given in Table XXIII. Although $I(E,E',Z,t)$ diverges as $E' \to 0$, the function can be integrated analytically

TABLE XXIII. Total Photon Yields used in Analysis

E_{beam}	Full Width	θ^*	E_γ range	N_γ
MeV	$\frac{\Delta}{E_{\text{beam}}}$	(nominal)	MeV	γ's per 1000 electrons
1598	0.249%	85°	1474–1574	3.1209
1598	0.249%	53°	1506–1574	2.0589
1598	0.249%	37°	1514–1574	1.8002
2014	0.399%	90°	1882–1990	2.6512
2014	0.399%	53°	1924–1990	1.5608
2014.5	0.399%	37°	1934–1990	1.3092
2401.5	0.399%	90°	2269.5–2377.5	2.2006
2401.5	0.399%	90°	2311.5–2377.5	1.2969
2401.5	0.399%	90°	2313.5–2377.5	1.2549
2801	0.399%	90°	2669–2777	1.8724
2801	0.399%	37°	2721–2777	0.92705
4214	0.249%	37°	4136–4190	0.58069

with respect to dE' in each E'-bin and the remaining numerical calculation converges rapidly. The integral was performed, for all kinematics, with 0.1 MeV steps in E' and E, and 0.006% steps in τ. The spectrum is then numerically integrated with k'-steps of 0.1 MeV to give the total photon flux:

$$N_\gamma = \int_{E_\gamma^{\text{low}}}^{E_\gamma^{\text{high}}} \frac{dN_\gamma}{dk'} dk'. \tag{A10}$$

The results are given in Table XXIII.

REFERENCES

[1] Chadwick and Goldhaber, Nature **134**, 237 (1935)

[2] J. Napolitano, *et al.*, Phys. Rev. Lett. **61**, 2530 (1988)

[3] S. J. Brodsky and G. P. Lepage, Nucl. Phys. **A353**, 247 (1981)

[4] H. Fritszch, M. Gell-Mann and H. Leutwyler, Phys. Lett. **B47**, 365 (1973)

[5] Phys. Rev. **D45**, Part 2 (1992).

[6] "Chiral Symmetry and the Bag Model: A New Starting Point for Nuclear Physics" in *Advances in Nuclear Physics* **V13**, Eds. J. W. Negel and E Vogt, (New York: Plenum Press, 1984), p. 1

[7] R. Blankenbecler, S. J. Brodsky and J. F. Gunion, Phys. Rev. **D18**, 900 (1978)

[8] D. Sivers, R Blankenbecler and S. J. Brodsky, Phys. Rep. **23**, 1 (1976)

[9] S. J. Brodsky and C.-R. Ji, SLAC-PUB-3747 (1985), p. 56

[10] M. P. Locher, *et al.*, "Dibaryon Resonances" in *Advances in Nuclear Physics* **V17**, eds. J. W. Negel and E Vogt, (New York: Plenum Press, 1986), p. 47

[11] S. J. Brodsky and G. R. Farrar, Phys. Rev. **D11**, 1309 (1975)

[12] S. J. Brodsky and J. R. Hiller, Phys. Rev. **C28**, 475 (1983)

[13] T.-S. H. Lee, ANLPHY-5253-TH-88

[14] S.I. Nagornyĭ, YU.A. Kasatkin and I.K. Kirichenko, Sov. J. Nucl. Phys. **55**, 189 (1992)

[15] S. J. Brodsky and G. R. Farrar, Phys. Rev. Lett. **31**, 1153 (1973)

[16] V. Matveev, R. Muradyan and A. Tavhelidze, Nuovo Cimento Lett. **7**, 719 (1973)

[17] D. H. Perkins, *Introduction to High Energy Physics, third Ed.*, (New York: Addison-Wesley. 1987)

[18] P. V. Landshoff and J. C. Polkinghorn, Phys. Lett. **B44**, 293 (1973)

[19] R. L. Anderson, *et al.*, Phys. Rev. **D14**, 679 (1976)

[20] S. J. Brodsky and B. T. Chertok, Phys. Rev. Lett. **37**, 269 (1976)

[21] N. Isgur and C. H. Llewellyn Smith, Nucl. Phys. **B317**, 526 (1989)

[22] M. Lacome, *et al.*, Phys. Rev. **C21**, 861 (1980)

[23] T.-S. H. Lee, Phys. Rev. **C29**, 195 (1984)

[24] D.O. Riska and G.E. Brown, Phys. Lett. **B38**,994 (1972)

[25] J. F. Mathiot, Phys. Lett. **B115**, 174 (1982)

[26] J. M. Laget, in *New Vistas in Electro-Nuclear Physics*, Eds. E. L. Tomusiak, H.S Caplan and E.T. Dressler (New York: Plenum Press, 1986), p. 361, and references therin.

[27] W. Leidemann and H. Arenhövel, Phys. Lett. **B139**, 22 (1984)

[28] C.R. Chen and T.-S. Lee, Phys. Rev. **C38**, 2187 (1988)

[29] R. V. Reid, Ann. Phys. (N.Y.) **50**, 411 (1968)

[30] T.-S. H. Lee, Phys. Rev. **C36**, 1549 (1987)

[31] Y. Kang, *et al.*, in Proceeding of the Particle and Nuclear Conference, MIT, Cambridge, MA (1990) p. I-40

[32] S.I. Nagornyĭ, YU.A. Kasatkin and I.K. Kirichenko, Sov. J. Nucl. Phys. **44**, 1171 (1986)

[33] F. Gross and B. D. Kiester, Phys. Rev. **C28**, 823 (1983)

[34] L. Tao, Ph.D. Thesis, The American University (1994)

[35] T. G. O'Neill, Ph.D. Thesis, California Institute of Technology (1994)

[36] T.-Y. Tung, Ph.D. Thesis, Northwestern University (1992)

[37] E. L. Garwin, Y. Tomkiewicz and D. Trines, Nucl. Instr. Methods**107** 365-370 (1973)

[38] P. Bosted and A. Rahbar, SLAC-NPAS-85-1, (1985)

[39] R. Fernow, *Introduction to Experimental Particle Physics*, (Cambridge University Press, 1986)

[40] E. Fenyves and O. Haiman, *The Principles of Nuclear Radiation Measurements* (New York: Academic Press. 1969)

[41] L. D. Landau, J. Phys. U.S.S.R. **8**, 201 (1944).

[42] K.L. Brown, *et al.*, SLAC Report No. 91, Rev. 2, 1977 (unpublished).

[43] Private Communication with G. G. Petratos.

[44] R. C. Walker, Ph.D. Thesis, California Institute of Technology (1989)

[45] Lisa Clogher, Ph.D. Thesis, The American University (1993)

[46] A. Lung, Ph.D. Thesis, The American University (1992)

[47] M. F. Gari and W. Krumpelmann, Z. Phys. **A322**, 689 (1985)

[48] N. T. Meister and D. R. Yennie, Phys. Rev. **130**, 1210 (1963)

[49] L.W. Mo and Y.S. Tsai, Rev. Mod Phys. **41**, 205 (1969)

[50] P. N. Kirk, *et al.*, Phys. Rev. **D8**, 63 (1973)

[51] J. L. Matthews and R. O. Owens, Nucl. Instr. Methods **111**, 157 (1973)

[52] L. E. Wright and L. Tiator, Phys. Rev. **C26** 2349 (1982)

[53] M. Berheim, *et al.*, Nucl. Phys **A365**, 349 (1981)

[54] H. Grenzel and W. Pfeil, Bonn Univ. Report **PIB** 1-168 (1972)

[55] H. L. Anderson, *et al.*, Phys. Rev. **D9**,580 (1974)

[56] P. Bareyre, *et al.*, Phys. Rev. **165**, 1730 (1968)

[57] R. J. Holt, *et al.*, Nuclear Physics at SLAC Proposal NE 17, 1989.

[58] J. D. Jackson, *Classical Electrodynamics*, (John Wiley and Sons, Inc., 1975)

[59] P. Dougan, *et al.*, Z. Physik **A276**, 55 (1976)

[60] R. Ching and C. Schaerf, Phys. Rev**141**, 1320 (1966)

[61] H. Myers, *et al.*, Phys. Rev **121**, 630 (1961)

[62] J. Arends, *et al.*, Nucl. Phys. **A412**, 509 (1984)

[63] Y. Burket, D Jenkins, B. Mecking, and W. Sapp, Deuteron Photodisintegration Letter of Intent of the CEBAF Project, 1988

[64] S. D. Drell and H. Pagels, Phys. Rev. **140**, B397 (1965)

[65] E. De Sanctis, A. B. Kaidalov and L. A. Kondratyuk, Phys. Rev. **C42** 1764 (1990)

[66] R. Arnold, B. T. Chertok, E. B. Dally, A. Grogorian, C. L. Jordan, W. P. Schültzs, R. Zdarko, F. Martin and B. A. Mecking, Phys. Rev. Lett. **35**, 776 (1975)

[67] R. Arnold, *et al.*, Phys. Rev. Lett. **58**, 1723 (1987)

[68] P. L. Chung, F. Coester, B. D. Keister, and W. N. Polyzou, Phys. Rev. **C37**,

2000 (1985)

[69] B. Pire and J. P. Ralston, Phys. Lett. **B117**, 223 (1982)

[70] S. J. Brodsky and G. F. Teramond, Phys. Rev. Lett. **60**, 1924 (1988)

[71] CEBAF Proposal PR-89-012, 1989.

[72] R. J. Holt, Phys. Rev. **C441** 2400 (1990)

[73] W. Heitler, *The Quantum Theory of Radiation, Third Ed.* , (Oxford: At the Clarendon Press, 1947)

[74] Y. S. Tsai, Rev. Mod. Phys. **46**, 815 (1974).

[75] Y. S. Tsai, Phys. Rev. **122**, 1898 (1961).

[76] R. A. Early, Nucl. Instr. Methods **109**, 93 (1973).

[77] L. Eyges, Phys. Rev. **76**, 264 (1949)

[78] G. Miller, SLAC Report No., SLAC-129 (1971)